UNIVERSITÄT AUGSBURG

INSTITUT FÜR PHYSIK

Investigation of the Physical Properties, Performance and Application of MEMS Sensors Based on Bulk Acoustic Waves excited in Piezoelectric Thin Film Devices

Dissertation zur Erlangung des Grades Doktor der Physik am Institut für Physik der Universität Augsburg

Jan Weber

Angefertigt unter dem Dekanat von Prof. Dr. Siegfried R. Horn

Gutachter: 1. Prof. Dr. Achim Wixforth
              2. Prof. Dr. Bernd Stritzker

Datum der mündlichen Prüfung: 16.5.2007

Zusammenfassung

In der vorliegenden Arbeit werden piezoelektrische Dünnschichtresonatoren (FBARs) untersucht und ihre Eignung und Leistungsfähigkeit in unterschiedlichen Sensorik-Anwendungen bewertet. Die theoretische und experimentelle Analyse der akustischen Modenstruktur brachte wichtige Ergebnisse die Form der akustischen Moden betreffend, welche Aufschluss für die Optimierung des Bauteils geben. Durch ein geignetes Design kann damit eine deutliche Verbesserung der Sensitivität und der Güte des Resonators erreicht werden. Unterschiedliche Moden können genutzt werden, um den Funktionsumfang der Sensors zu erhöhen und eine gezielte Modenselektion durch Aufbringen einer Struktur auf den Resonator erscheint möglich. Weiterhin wurde der Einfluss von Designparametern wie der Arbeitsfrequenz, Größe und Form des Resonators sowie Elektrodendicke auf die Leistungsfähigkeit untersucht. Unterschiedliche Sensorikanwendungen wurden ausprobiert, von Stressmessungen über Viskositätsmessungen bis hin zu Biomessungenen und auch eine Anwendung als Flüssigkeits-Mischer wurde erfolgreich getestet. In allen Anwendungen wurden die Performance des Sensors durch Experimente evaluiert und durch Modelle unterfüttert. In Biosensorexperimenten zeigte sich, dass der FBAR im direkten Vergleich zum QCM etwas besser abschnitt.

Abstract

In this work, piezoelectric thin film resonators (FBARs) are investigated and their performance and aptitude in different sensing applications is evaluated. The theoretic and experimental analysis of the acoustic mode structure yielded important results describing the nature of different modes and providing information for resonator optimization. With an appropriate design a significant improvement of the sensitivity and quality factor can be achieved. Different modes can be furthermore exploited to enhance the functionality of the sensor and a selection of specific modes by applying a structure on top of the resonator seems possible. Furthermore the influence of design parameters such as the operation frequency, resonator size, form and electrode thickness on the device performance were investigated in detail. Different sensing applications were tested from a stress- over a viscosity- to a bio-sensor and also the capability to act as a fluid mixer was tried successfully. The performance in all these applications was evaluated experimentally and backed up with theoretical models. In comparison experiments acting as a biosensor the FBAR was found to be slightly better than the established quartz crystal microbalance.

Contents

Vorwort

Die hier vorliegende Arbeit wurde im Rahmen einer Industriepromotion in der Gruppe für funktionelle Dünnschichten der Abteilung Materials & Microsystems Ceramics der Corporate Technology von Siemens verfasst. Die Arbeit fand statt im Rahmen von zwei durch die EU geförderten Projekten, PISARRO[1], welches sich über den Zeitraum von 2002 bis 2005 erstreckte, sowie BIOGNOSIS[2] seit 2005.

An dieser Stelle möchte ich den Personen herzlich danken, die am Gelingen der Arbeit ihren Anteil hatten. Reinhard Gabl, der die Gruppe funktionelle Dünnschichten von 2003 bis 2005 betreute und den maßgeblichen Anteil an der Ausgestaltung der Thematik hatte. Achim Wixforth von der Universität Augsburg, der die Arbeit von universitärer Seite betreute und äußerst großzügig sowohl experimentell als auch thematisch unterstützt hat. Mathias Schreiter, der die Leitung der Gruppe funktionelle Dünnschichten ab 2005 übernommen hat und dafür gesorgt hat, dass die Projekte und meine damit im Zusammenhang stehende Doktorarbeit nahtlos weitergeführt wurden. Wolfram Wersing, der für die Beantragung des ersten Projektes und damit die Etablierung des Themas FBAR-Sensorik in der Gruppe maßgeblich verantwortlich war und dessen Rat und fachliche Betreuung überaus hilfreich war. Mein Dank gilt weiterhin Wolfgang Rossner, der die Abteilung Materials & Microsystems mit Stetigkeit und Engagemnent führte. Herzlich danken möchte ich zudem Mathias Link, der als Doktorand wie ich an FBARs arbeitete und durch dessen Arbeit an der Prozesstechnologie die Messungen in dieser Doktorarbeit überhaupt erst möglich wurden. Weiterhin gilt mein Dank Matthias Schneider von der Universität Augsburg für eine sehr fruchtbare Kooperation. Ich möchte außerdem Robert Primig und Dana Pitzer aus unserer Gruppe danken für die Unterstützung in der Prozesstechnologie. Schließlich gilt mein Dank allen Praktikanten und Diplomanden in unserer Gruppe sowie den Diplomanden und Doktoranden am Lehrstuhl für Experimentalphysik in Augsburg sowie allen weiteren Personen, die direkt oder indirekt zum Gelingen dieser Arbeit beigetragen haben.

Der zunehmenden Internationalität unserer modernen Welt und auch unserer Arbeitsgruppe schuldend, habe ich diese Arbeit in englischer Sprache verfasst. Ich hoffe, dass sie damit mehr Menschen zugänglich wird.

Jan Weber   München, 29.04.2007

---

[1] Piezoelectric Sensing Arrays for Biomolecular Interactions and Gas Monitoring
[2] Integrated Biosensor System for Label-Free In-Vitro DNA and Protein Diagnostics in Health Care Applications

1.   Introduction

Background and Context

In this work the capability of MEMS sensors based on bulk acoustic waves for different applications will be investigated. MEMS (microelectromechanical systems) are a combination of sensors, actuators and electronic circuitry on one single chip. They are an important step towards enhancing the functionality of microelectronics from simple computational tasks to a system interacting with the environment and gathering information with the help of sensors or fullfilling mechanical tasks with the help of actuators.

The device under consideration is a bulk acoustic resonator (FBAR) and is based on the excitation of acoustic waves in a thin film structure. The films are manufactured bottom up using sputtering technologies and thicknesses in the range of a few nanometers to some micrometers are achieved. The acoustic waves are excited piezelectrically and due to the low thicknesses of the films, acoustic frequencies up to several gigahertz can be obtained. The specific sequence of layers leads to a formation of standing waves at certain frequencies.

Historically, FBARs may be put into a line with quartz microbalances and surface acoustic wave devices. Quartz crystals have been used in military communication already during the second world war and their use in the field of sensors got a kick off when Sauerbrey showed the linear relation between the device resonance frequency and a mass attachment in 1959 [SAU59]. Since then, their importance in this area has steadily been increasing making them today standard devices which are widely used not only bioanalytics [SHO72], [LEC01], but also to monitor the quality of automotive engine oil [HAM97] and may be even applied for other applications in the automotive field [JAK02]. There are a number of companies distributing QCMs as diagnostic device as well as thickness monitor in deposition technology. Especially the application in the biological science has become so broad [JAN00] that hardly anyone will be able to give a complete description of all the applications that exist to date. Examples are the monitoring of blood coagulation processes [GUH05], DNA/RNA sensing [FAW88] and immunosensing [SHO72] to name only a few.

With the rise of semiconductor fabrication technology, surface acoustic waves gained increasing importance in the field of acoustic devices. They made use of the new ability of photolithographic processes to fabricate very small patterns. With the application of interdigital transducers it was thus possible to excite acoustic waves travelling on the substrate surface and an increase of the operation frequency was obtained. A comparison of these different sensing technologies is found in Benes et al. [BEN97].

This switch from bulk to surface acoustic waves is now again being reversed, with modern sputtering technology enabling growth of thin and homogenous piezoelectric films leading to the emergence of FBARs. These devices have already gained a lot of importance in the field of filters and make up a mass market there with the requirement of low noise high performance filters in mobile phone technology [VAL90]. It is thus a logical step in the context of a highly dynamically market for micro sensors to apply them as sensors as well.

Diagnostics is one sensor application getting more and more into the focus of the medical research society as well as the suppliers of diagnostic tools such as Siemens or Phillips. Diagnostics on the molecular level is broadly regarded as one key to treat diseases such as cancer. This is because on the one hand cancer is so complex that what was seen once as one certain disease pattern turns out to be very complex and having a lot of different specifications. Depending on the special clinical picture and the genotype a certain therapy is only effective in certain patients.

Another reason for diagnostics gaining importance is a crisis in traditional pharmaceutics with the development of new drugs being time consuming and expensive. Therefore a new trend is towards a more integrated health system, where practicing physicians, medical researchers and drugmakers are linked together. This would greatly facilitate the access to the results of medical treatments and would make the development of new treatments much more effective.

Such a new health system requires smart and easy-to-use devices being able to record as many medical data as possible and also allowing a quick processing and transmitting of this data. The quicklab®-platform, a disposable diagnostic tool in the form of a chip card and being developed at Siemens AG, is one such tool. With such a device establishing for instance as a standard blood test in the medical practices a huge market would open up. According to [MIN01] the market for micro systems in health and biotech, being in the very beginning of the development, already has a volume of $ 10 billion.

To enable the readout of such a test, an appropriate sensor technology is required. Sensors have to be developed, that can be integrated into current semiconductor processing and that are small and cheap and that can be used for different applications. With bulk acoustic wave devices being established in diagnostics and being transformed into a CMOS-integrable form with the help of thin film technology, an appropriate technology is now within reach. In contrast to QCMs, FBARs are manufactured bottom up and the manufacturing technology is principally compatible with CMOS processes. They can be made very small and with photolithographic processes an integration of the sensor with electronics is possible. Compared to other systems it has the great advantage to be label

free and real time, so measurements can be carried out quickly and the measurement procedure can be simplified considerably.

With these characteristics, FBARs provide a platform for many other applications and objectives that are envisioned in the health care sector. Potential applications may be found in the online monitoring of patients with implantable sensors, automated or intelligent drug delivery systems (smart pills), artificial organs and minimal invasive surgery. All these fields require highly miniaturized sensor systems. One interesting perspective in this context are sensors than can be read out remotely, so-called wireless sensors [LOH05]. This technology is already applied successfully for monitoring the pressure in car tyres [POH97] with surface acoustic wave technology. With the same technology also a wireless biosensor has been presented [FRE99].

The aim of this work is on the one hand to investigate a certain bandwidth of measurement applications ranging from viscosity-, pressure- to biosensing, thereby highlighting the potential of this exciting new device. The different requirements due to the application as a sensor in comparison to filters will thereby be kept in mind. On the other hand it shall be investigated, where the bottlenecks for the sensor performance lie, in order to be able to make a judgement over which steps have to be taken in order to improve this sensor. Especially the latter is something which has to be considered in every application, because the application itself strongly influences the requirements for the sensor system.

Contents

The first three chapters (chapters 2 to 4) will concentrate on the device itself. Chapter 2 will give a description of the device with the theoretical as well as experimental tools necessary for analyzation and fabrication. Chapter 3 will then deal with the acoustic behaviour and will analyze vertical and lateral acoustic modes with theoretic and experimental tools. Aspects of device performance and improvement opportunities will thereby be kept in mind throughout the analysis. Sensor performance will be especially addressed in chapter 4 where such issues as electrical and acoustic losses will be analyzed. It will be especially tried to draw conclusions regarding the sensor design.

In the three chapters that follow, the focus will be on the device application. In chapter 5 the application as a stress sensor will be examined. This is an application which could be relevant on the one hand to monitor the strains in all kinds of materials with the sensor being mounted directly on the material and measuring the strain on the material surface similar to a strain gauge. Another application is the monitoring of pressures in a fluidic system. The focus of chapter 5 will be to make an assessment of the stress sensitivity of the FBAR.
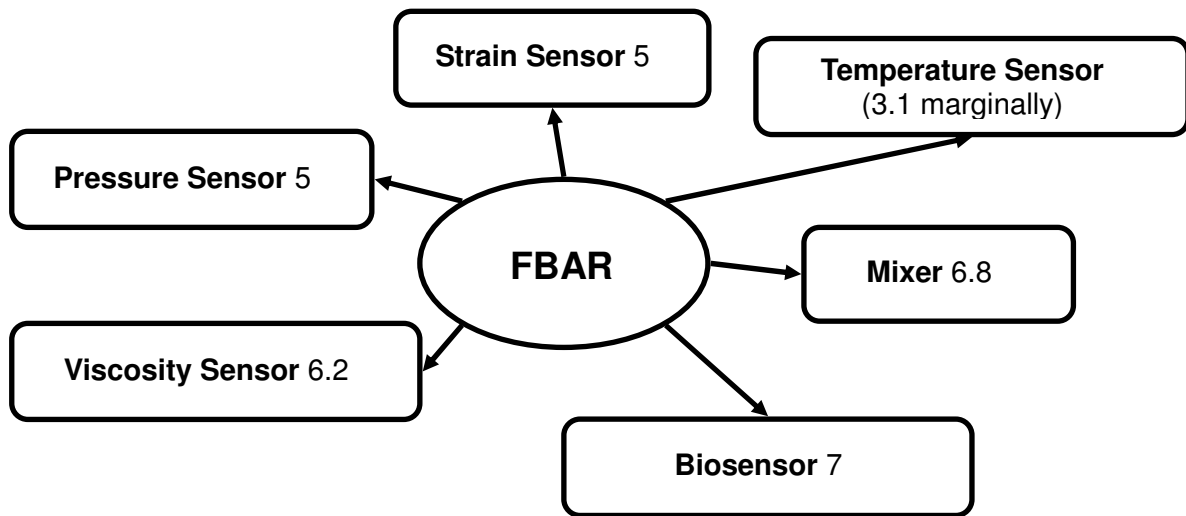
Strain Sensor 5

Temperature Sensor
(3.1 marginally)

Pressure Sensor 5

FBAR

Mixer 6.8

Viscosity Sensor 6.2

Biosensor 7

Figure 1.1: Different applications of an FBAR and the chapter, where these applications are addressed within this work.

In chapter 6, the application of the sensor in liquid will be investigated in detail. This is important because of two reasons. First the possible application as a viscosity sensor shall be tested. Bulk acoustic wave sensors are already applied in the form of quartz crystal microbalances for the monitoring of the quality of car engine oils. Measuring the viscosity at FBAR frequencies however has not been done so far, so it shall be investigated how the fluid behaves at these frequencies in order to find out, whether the fluid is still acting purely viscously. The other objective is to investigate the sensor performance in liquid. As most of the biosensing applications take place in a liquid environment, it is important to know the sensor performance in liquid and especially to quantify the influence of the fluid depending on the sensor and the fluid properties. Finally the capability of the FBAR as a mixer will be tested.

In the last chapter the application as a biosensor will be investigated. First, the biosensing principle will be explained and it will be tried to make a transition from the "physical" and the "biological sensitivity". Then a range of biosensor applications will be tested starting with a standard system known from the application of quartz crystal microbalances as immunosensors. This system shall serve for the quantification of the sensor performance in a realistic biosensing experiment and a comparison with QCM operating at a nearly two orders of magnitude lower resonance frequency will be done. It will be shown though, that the performance of the FBAR in this experiment is at least as good as QCM and that the qualitative behaviour is quite similar.

Furthermore the binding of lipid vesicles on the sensor surface will be tested and especially the influence of the elasticity on the binding dynamics will be investigated. This will give some insight of the interaction of spherical shaped objects with the flat sensor surface. In the section that follows, the formation of S-Layers on the sensor surface will be tested. Here, the special focus will be on the investigation of the influence of analyte concentration on the binding dynamics and a series of experiments will be carried out to assess this influence. In the last section of chapter 7, carbon nanotubes will be applied on the sensor surface. With a low acoustic velocity they provide a good example for a two layer system and may represent a candidate for the sensitivity enhancement method introduced in chapter 3.

2. Basic Description of the Device

In this chapter a description of the device will be given and the underlying theory will be presented. The aim is to get an understanding of the tools (theoretical as manufacturing), that are needed to describe and develop this sensor.

In the first section the sensor will be introduced and the mode of operation explained. This is followed by a treatment of the mathematics. There are three theoretical methods for the sensor description which will be addressed. They differ in their respective level of abstraction. The first method (section 2.2) comes from the fundamental physical properties of the sensing system and with the help of the equations of motion the acoustic wave form will be calculated. This is a good method when one is interested in the fundamental physical properties and an example of its successful application is the Kanazawa equation describing the frequency response of the sensor with a liquid on top (see chapter 6).

In the next section (2.3), a model based on an acoustic impedance concept will be described. The main assumption for this model is the one dimensional harmonic propagation of the acoustic waves. It has the advantage to be suitable for description of a complex layer stack as it is also present in the device used here. Furthermore, through acousto-electric analogies it is possible to derive the electric impedance of the device. As an approximation of this model, the so called Butterworth-van-Dyke-model will be presented. It is a purely electrical model, describing the electrical impedance with an electrical equivalent circuit. The acoustic properties of the sensor can be derived indirectly from the lumped elements but they are not inherently part of the model. This model is especially suitable for impedance analysis and a fitting algorithm using this model is applied in chapter 3.

In the section that follows, a short introduction into the models describing the sensor sensitivity will be given and in the last section of this chapter the process required for manufacturing of a suitable ZnO layer for shear mode excitation will be explained.

2.1 Sensing Principle

The device described in the frame of this work uses the principle of piezoelectricity. The effect is schematically shown in figure 2.1. It bases on the displacement of charges that are bound in the crystal. A mechanical deformation leads to a net displacement of the effective charge. Positive and

negative charges are moving in opposite direction giving rise to the formation of an electric dipole. When applied to a bulk, the dipole moment can be read out as an electrical voltage.

This effect is called the direct piezoelectric effect. The opposite effect is called inverse piezoelectric effect and describes the deformation of the crystal due to an application of a voltage. Piezoelectricity occurs only in nonconducting materials. A crystal is piezoelectric, when it has no inversion symmetry (consider figure 2.1: taking the centre of gravity as inversion centre leads to mapping the positive charges on the negative ones and vice versa).
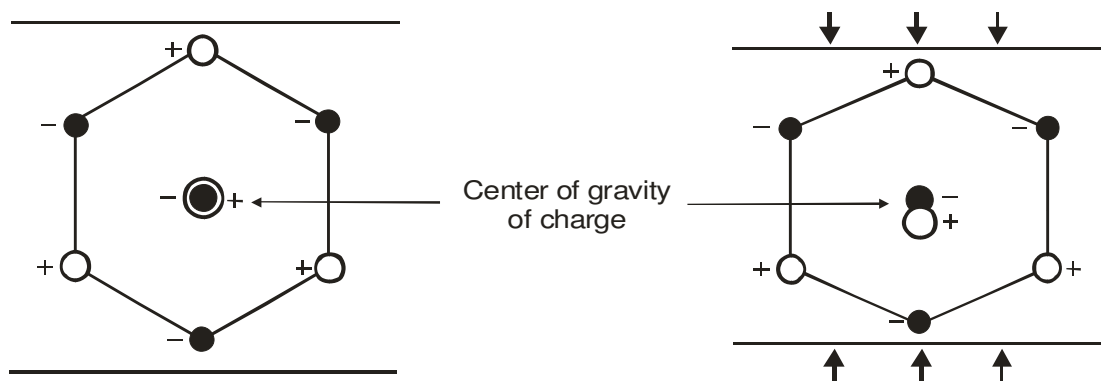

Figure 2.1: Piezoelectric effect: due to a mechanical deformation positive and negative charges show a displacement relative to each other giving rise to the formation of an electric dipole.

The application of an alternating voltage leads to the generation of acoustic waves. It is common to divide acoustic waves into two general types. The first type are acoustic waves that are propagating along the surface of a substrate. These waves are more or less trapped at the surface because of the great difference between the acoustic velocities in the bulk and in air. They are called surface acoustic waves.

The other type of waves are bulk acoustic waves. These waves are propagating in the bulk and only interact with the surface through reflection. The sensor described in this work uses these bulk waves. There exists yet another wave type, which is a hybrid of the two types mentioned before. Surface acoustic waves can have a small propagation component into the bulk. When the substrate is very thin, this component may be reflected from the backside. This gives rise to a wave travelling

in the direction of the substrate surface, but with the whole substrate participating in the wave propagation. These kinds of waves are called acoustic plate modes.
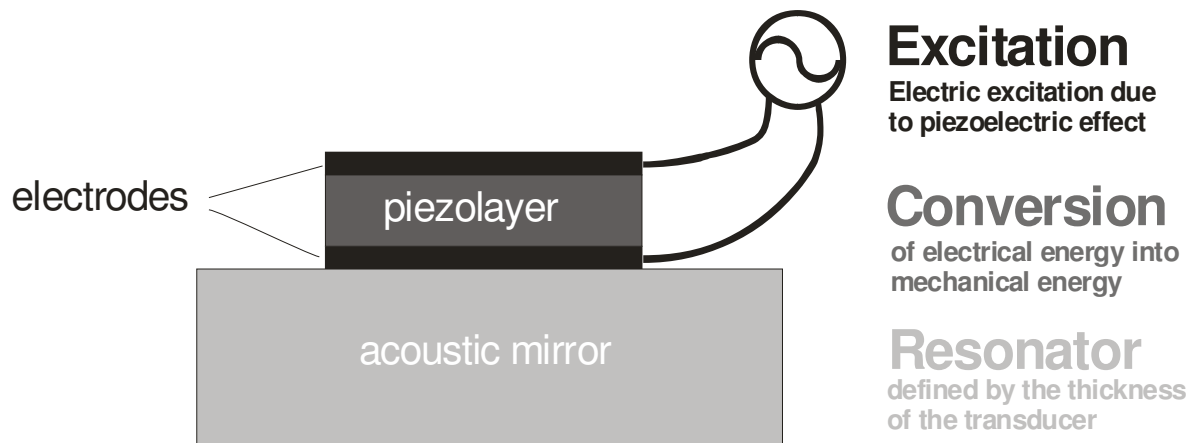

Figure 2.2: Mode of operation of the FBAR-sensor. Three principles are working together: Energy is provided with an alternating electric field which is supplied to the electrodes. Conversion into mechanical energy is achieved with a piezoelectric layer. The resonator is defined by the device thickness which is enclosed by the acoustic mirror at the bottom and the free end at the top (air or water depending on the application).

The piezoelectric effect can be exploited to build an electromechanical resonator. This is a device which converts energy from one type to an other. In the case of the FBAR electrical energy is converted to mechanical energy and vice versa. Electromechanical or piezoelectric resonators have two important fields of application. One is the field of electrical filters. They make use of the good mechanical quality factor. Moreover the velocity of propagation of acoustic waves is considerably lower than for electrical waves (depending on the elastic and dielectric properties of the material it is in the vicinity of 10^4 *m/s* compared to 10^8 *m/s* for an electric wave). Thus, the size of a piezoelectric resonator is much smaller than a dielectric resonator of comparable frequency.

The other field of application are sensors. Transducing is essential in this field, because it is not always possible to detect the property that is to be sensed with the physical principle used to process the information. The sensor described here detects a mechanical property with the help of an acous-

tic wave and converts this property into an electrical signal. As it will become clear throughout this work, this mechanical property can either be a mass added to the sensor, or it can be the acoustic propagation properties of the sensor itself. The latter again can be influenced by physical properties such as temperature or stress.

The core of the device consists of three main parts. The first serves for excitation of the acoustic wave. This is done with the help of an electric capacitor, which is contacted to some high frequency electronic circuitry. The excitation also serves for readout. Secondly the conversion of the energy from electric to acoustic energy is done with the help of a piezoelectric layer that is enclosed by the electrodes. Finally there needs to be a resonator, defining the acoustic resonance frequency. This resonator can be realized in different ways. The device described here uses an acoustic mirror. Like the Fabry-Perot layers known from optics this acoustic mirror is made of alternating layers with high and low acoustic impedance. When they have a thickness of a quarter acoustic wavelength at resonance, the impedance difference at each layer surface leads to a partial reflection of the acoustic wave. With a sufficient number of mirror layers the reflection will be nearly total.

The measuring principle of the device bases on the fact that a change of a physical property causes a change of resonance frequency. If for instance some material is added on top, the acoustic length of the resonator increases. This leads to a decrease of the resonance frequency which in turn can be read out electrically.

2.2 Physical Treatment

The general aim in the physical treatment of an acoustic or piezoelectric structure is to obtain some sort of frequency dependent behaviour of the acoustic amplitude. The starting point are thereby the geometry of the device, the material parameters and the boundary conditions. So the way towards a solution of the structure involves three steps. First, the stress-strain relations must be found for the parts composing the acoustic system. Then, the equations of motion relating force to acceleration have to be set up. Finally this system has to be solved by applying the appropriate boundary conditions. To be able to solve the problem exactly, there have to be as many boundary conditions as there are independent variables. The stress-strain-relations will be treated in the next subsection.

Stress and Strain

Strain in a medium is the equivalent to the elongation of the spring in a system with two masses and a spring. It is defined as the change of the displacement component with respect to a certain direction:

$$S_{ij} = \frac{1}{2}\left(\frac{du_i}{dx_j} + \frac{du_j}{dx_i}\right)$$

eq. 2.1.

The diagonal elements ($i = j$) are related to longitudinal strain and the off-diagonal elements ($i \neq j$) describe a shear strain. Due to the symmetry of this definition it is $S_{ij} = S_{ji}$, so the strain consists of 6 elements, which are often written as:

$$S_1 = S_{11},\ S_2 = S_{22},\ S_3 = S_{33},\ S_4 = 2S_{23},\ S_5 = 2S_{13},\ S_6 = 2S_{12}$$

eq. 2.2.

To distinguish between these two notations, the new notation will be given capital letter subscripts. The stress T on the other hand is the equivalent to force. It is related to strain via the magnitude c, called stiffness. It has the same number of components as strain. In the one dimensional case, stiffness would be the reciprocal value of the well known spring constant. Depending on the respective notation, the stiffness becomes a matrix of 3^4 or 6×6 elements:

$$T_I = c_{IJ}S_J \quad \text{with} \quad I,J = 1..6$$

eq. 2.3.

$$T_{ij} = c_{ijkl}S_{kl} \quad \text{with} \quad i,j,k,l = 1..3$$

The strain components are defined the same way as the stress components. With a certain stress component being related to the derivative respect to one certain direction ($T_{ij} = c_{ijkl} \dfrac{du_k}{dx_l}$) it can be understood as a force per unit area (see figure 2.3):
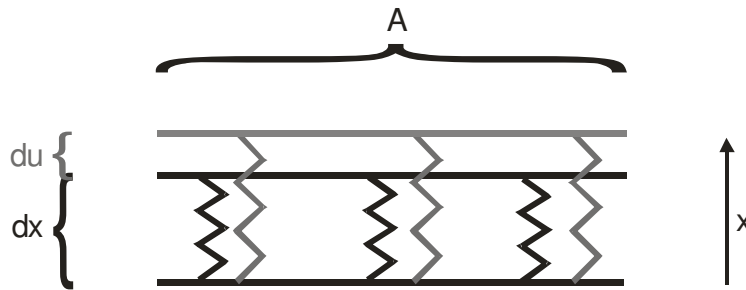
$$T_{ij} = \frac{dF_{ij}}{dA} \qquad\qquad\qquad \text{eq. 2.4.}$$

Figure 2.3: Illustration for Newtons law in a medium. du *is the deflection and* dx *the particle distance in* x-*direction,* A *the area (in* y- *and* z-*direction). Stress can be understood as a force per unit area.*

For an isotropic medium two magnitudes are extracted from the stiffness matrix and given special names because of their special relevance. Assume that the medium is subjected to a force that is acting in one direction only. This could be a lateral pressure, for instance. The medium will react in two ways: it will contract in the direction the pressure is applied and extend in the lateral direction. The Young's modulus Y_0 describes the contraction. It is defined by $S_1 = \dfrac{1}{Y_0} \cdot T_1$. Writing the Young's modulus in terms of the stiffness matrix requires a matrix inversion and yields [ROS88]:

$$Y_0 = \frac{(c_{11} - c_{12})(c_{11} + c_{12})}{c_{11} + c_{12}} \qquad\qquad \text{eq. 2.5.}$$

Furthermore the medium will expand in the direction lateral to the direction the force is applied. The poisson ratio σ defines the relation between contraction and expansion: $S_2 = -\sigma \cdot S_1$.

For a piezoelectric medium the Stress-Strain relation has to be completed by a term describing the stress, that is introduced by piezoelectricity:

$$T_{ij} = c_{ijkl}^{E} S_{kl} - e_{ijk} E_k \qquad\qquad \text{eq. 2.6,}$$

where the superscript E stands for constant electric field, e_{ijkl} is the piezoelectric matrix and E_k denotes the electric field.

Equations of motion

According to Newtons law, force is mass times acceleration. In a medium, Newtons law has to be set up in an infinitesimal form. This means that all the magnitudes have to be in the form magnitude per unit volume. In the previous subsection, stress was shown to be a force per unit area. In order to obtain the force per unit volume, stress has to be differentiated with respect to the direction x. Hence, force density is the divergence of stress:

$$f_i = \frac{d}{dx_k} T_{ik} = \rho \frac{d^2 u_i}{dt^2} \qquad\qquad \text{eq. 2.7,}$$

or, replacing the stress according to equation 2.3:

$$\frac{d}{dx_j} c_{ijkl} S_{kl} = \rho \frac{d^2 u_i}{dt^2}$$ eq. 2.8

with ρ the mass density of the medium. Equation 2.8 is the formulation of Newtons law in an elastic body. To solve the equation of motion, the appropriate stress is required, depending on the respective material system which may be elastic, piezoelectric or viscous. For a piezoelectric system, for instance, the stress from equation 2.6 has to be used and the equation of motion becomes:

$$\frac{d}{dx_j} c_{ijkl} S_{kl} - \frac{d}{dx_j} e_{ijk} E_k = \rho \frac{d^2 u_i}{dt^2}$$ eq. 2.9.

Crystal structure of ZnO

The crystal structure of ZnO is shown in figure 2.4. It is a wurtzite structure, which is a hexagonal structure and belongs to the class 6mm. It is a densely packed structure with the layer sequence A-B-A. The basis simply consists of one zink and one oxygen atom and the oxygen is situated right in the centre of the tetrahedron that is made up by its 4 nearest neighbours.

The stiffness matrix of this structure is:

$$c_{IJ} = \begin{bmatrix} c_{11} & c_{12} & c_{13} & 0 & 0 & 0 \\ c_{12} & c_{11} & c_{13} & 0 & 0 & 0 \\ c_{13} & c_{13} & c_{33} & 0 & 0 & 0 \\ 0 & 0 & 0 & c_{44} & 0 & 0 \\ 0 & 0 & 0 & 0 & c_{44} & 0 \\ 0 & 0 & 0 & 0 & 0 & c_{66} \end{bmatrix} \quad \text{with} \quad c_{66} = \frac{c_{11} - c_{12}}{2}$$ eq. 2.10.

The structure shown in figure 2.4 corresponds to this compliance matrix. There are 5 independent components. The main symmetry axis x_3 is equivalent to the packing direction. This axis is also commonly referred to as c-Axis. The directions perpendicular to it (x_1 and x_2) are equivalent in their acoustic propagation properties, which is manifested in the fact that not only the compliances for the longitudinal displacement are equal (c_{11}), but also for the components relating different longitudinal displacements (c_{13}) and also the shear compliances (c_{44}).
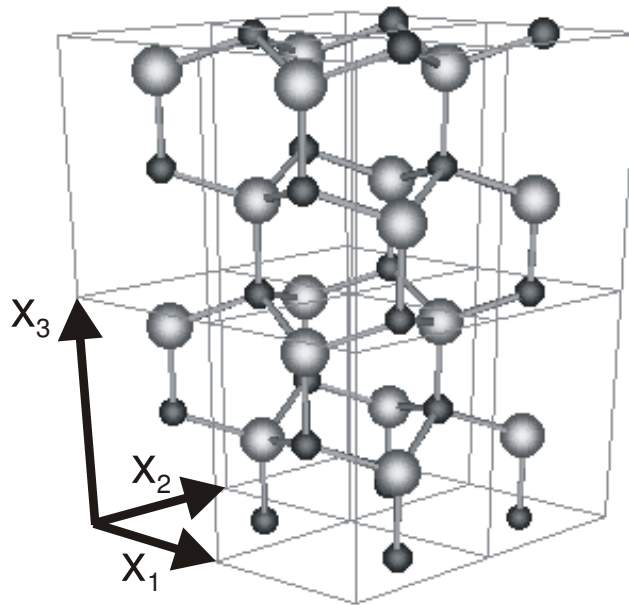

Figure 2.4: Hexagonal structure of ZnO: it is a closely packed structure with the layer sequence A-B-A. The main symmetry axis x_3 is in the packaging direction, the directions perpendicular are equivalent regarding their acoustic propagation and the piezoelectric excitation. The basis consists of one Atom of Zn and O respectively.

The correspondent piezoelectric matrix is:

$$e = \begin{bmatrix} 0 & 0 & 0 & 0 & e_{15} & 0 \\ 0 & 0 & 0 & e_{15} & 0 & 0 \\ e_{31} & e_{31} & e_{33} & 0 & 0 & 0 \end{bmatrix} \qquad \text{eq. 2.11.}$$

Again the symmetry of this piezoelectric matrix corresponds to the symmetry crystal symmetry as discussed above. The two directions x_1 and x_2 are equivalent in their piezoelectric activity and the x_3-axis is the main symmetry axis. The strain, that is caused by an electric field ($T_I = e_{IK} \cdot E_K$), takes the form:

$$T = \begin{bmatrix} e_{31} \cdot E_3 \\ e_{31} \cdot E_3 \\ e_{33} \cdot E_3 \\ e_{15} \cdot E_2 \\ e_{15} \cdot E_1 \\ 0 \end{bmatrix} \qquad \text{eq. 2.12.}$$

Without any of the directions perpendicular to the x_3-axis being distinguished, a field parallel to x_3 (E_3) will only excite longitudinal strains (T_1 to T_3). Only a field with a component perpendicular to the x_3-direction can excite a shear strain (with E_1, E_2 a strain $T_4 = t_{23}$ and $T_5 = t_{13}$ can be excited). The FBAR examined in this work has been developed mainly for sensing applications in liquid. To reduce acoustic losses in the liquid, an operation in acoustic shear mode is strongly favourable. Therefore a mode of operation of the FBAR had to be found with a non vanishing angle between c-Axis and the exciting electric field. This was achieved with a c-Axis inclined growth of the ZnO-layer (see section 2.5).

2.3 Impedance Model

In this section, a model for a one dimensional acousto-electric structure will be developed. The proceeding to arrive at this model is the one described in the previous section. The stress-strain relations are put into the equations of motion and the appropriate boundary conditions are applied. The aim is to obtain a model describing the electrical output impedance of a one dimensional acoustic layer stack containing one piezoelectric layer and two electrodes. A detailed description of this derivation is given for instance in [LUT97] and here the focus will lie on the important equations and

the approximations made. Two tasks have to be solved for this problem: the acoustic behaviour of the stack has to be solved and the conversion from acoustic to electric energy in the piezolayer and the corresponding voltage obtained at the piezolayer surfaces has to be derived. To solve the first task, the acoustic impedance concept described in the next subsection will be applied.

The acoustic impedance concept

The acoustic impedance is defined as an analogy to electrical circuits. In this analogy stress is identified as the „acoustic voltage", whereas particle velocity is the analogue to the electrical current.

$$Z_{ac} = -\frac{T}{v} \quad \leftrightarrow \quad Z_{el} = \frac{U}{I} \qquad\qquad \text{eq. 2.13.}$$

This concept is very useful. As will be shown later, by using the acousto-electric analogies the electric input-impedance of the device can be determined directly by inserting its acoustic properties. An acoustic wave travelling in one direction (x_3) in a homogenous, infinite medium will have the form of a cosine: $u = a\cos(kx_3 - \omega t)$. Inserting this deflection successively into equation 2.1, 2.3 and 2.13, the acoustic impedance becomes:

$$Z_{char} = -\frac{c\,\dfrac{du}{dx_3}}{\dfrac{du}{dt}} = \frac{ck}{\omega} \qquad\qquad \text{eq. 2.14.}$$

This impedance is also called the characteristic acoustic impedance. It will be used in the following for the calculation of the wave propagation in a multilayer structure, where an ideal wave propagation is assumed. Equation 2.14 can be reshaped to form a simple expression containing only material properties. Differentiating equation 2.7 with respect to x_k and dividing by ρ yields:

$$\frac{1}{\rho}\frac{d^2T_{ik}}{dx_k{}^2} = \frac{d^3u}{dt^2 dx_k}$$

eq. 2.15.

On the other hand, taking the stress-strain-relation (equation 2.1) and differentiating twice with respect to time (and dividing by c), yields:

$$\frac{1}{c}\frac{d^2T}{dt^2} = \frac{d^3u}{dt^2 dx_k}$$

eq. 2.16.

By equating 2.15 and 2.16, the phase velocity of the wave is obtained:

$$v_a = \sqrt{\frac{c}{\rho}}$$

eq. 2.17.

This can be used to further simplify the expression of the characteristic impedance. Using $v_a = \omega/k$ and equation 2.17 in equation 2.14 yields:

$$Z_{char} = \rho \cdot v_{ac}$$

eq. 2.18.

Acoustic propagation

Now the set of equations describing the propagation of plane waves in a one dimensional acoustic system will be developed. It will become clear later, that this provides a powerful tool to analyze the resonance structure of the FBARs. As shown in the introduction an FBAR is composed of a multi-layer system with acoustic waves being generated in a piezoelectric layer. The aspect ratio of layer thickness to lateral size is in the range of about 1:100 to 1:10000. So in a first approximation the

device can be regarded as infinite in the lateral direction or as one dimensional. In such a one dimensional structure only one dimensional waves can be excited.

In a further assumption the wave within each layer is assumed to be harmonic. It is propagating undisturbed across the layer with constant wave number and changes only occur at the interfaces between the layers, where part of the wave is being reflected and another part is being transmitted (see figure 2.5. Hence, the wave inside each layer is composed of a part travelling in forward and one travelling in backward direction. The particle deflection thus has the form of a cosine function, which may be written as the real part of an exponential function:

$$u_{1,2} = \mathrm{Re}\left(a_{1,2}e^{-i(kx_3-\omega t)}\right) + \mathrm{Re}\left(b_{1,2}e^{i(kx_3+\omega t)}\right) \qquad \text{eq. 2.19.}$$
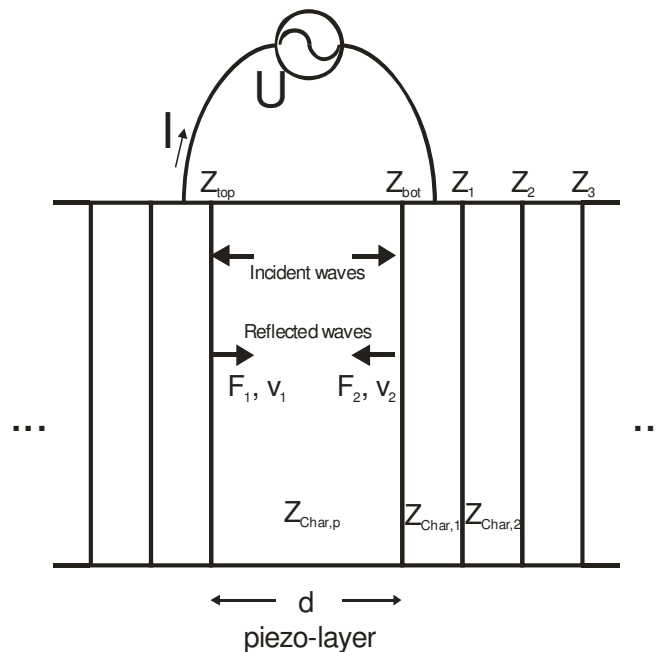

Figure 2.5: Model for the electric impedance in a one dimensional acoustic-piezoelectric system. The acoustic energy is converted into electric energy inside the piezoelectric layer. With the acoustic impedance concept an impedance for every single point within the non-piezoelectric part of the acoustic structure can be calculated. Applying the appropriate boundary conditions (sinusoidal electric potential at the piezolayer surfaces) the electric current into the electrodes and with that the input-impedance can be determined.

In the following the "Re" may be left out for convenience. The particle velocity is:

$$v_{1,2} = i\omega a_{1,2} e^{-i(kx_3 - \omega t)} + i\omega b_{1,2} e^{i(kx_3 + \omega t)} \qquad \text{eq. 2.20.}$$

Solving for the coefficients $a_{1,2}$ and $b_{1,2}$ and using $T = c\dfrac{du}{dx_3}$, an expression can be found relating

the forces and the velocities at the beginning and at the end of the layer [ROS88]:

$$T_1 = \frac{Z_{char}}{i \sin kd}(v_1 - v_2) + i Z_{char} \tan\left(\frac{kd}{2}\right) v_1 \qquad \text{eq. 2.21}$$

$$T_2 = \frac{Z_{char}}{i \sin kd}(v_1 - v_2) - i Z_{char} \tan\left(\frac{kd}{2}\right) v_2 \qquad \text{eq. 2.22}$$

with Z_{char} the characteristic acoustic impedance according to equation 2.18 is the acoustic imped-
ance for the layer under the assumption that it is infinite and that the wave is propagating only in
one direction. It shall be referred to as the "material impedance" and will be indicated with a small
z. So it is possible to decouple the equations describing the wave propagation. Practically this
means, when the layer composition (i.e. the acoustic impedance and thickness of each layer) is
known and furthermore the velocity and force at the surface of the first layer are given, it is possible
to calculate the force and velocity at each subsequent layer interface. With the trigonometric rela-
tions these equations can be modified to give:

$$\frac{T_2}{v_2} = Z_{char} \left[\frac{\dfrac{T_1}{v_1} - iZ_{char} \tan kd}{Z_{char} - i\dfrac{T_1}{v_1} \tan kd} \right] \qquad \text{eq. 2.23}$$

$$v_2 = \frac{Z_{char} v_1}{i\dfrac{T_2}{v_2} \sin kd + Z \cos kd} \qquad \text{eq. 2.24.}$$

So in the first of these equations the acoustic impedance $Z_i = \dfrac{T_i}{v_i}$ can be introduced. In order to completely solve for stress and velocity at every single point of the structure, both equations are needed. Nevertheless, in the following only equation 2.23 will be used and it will be shown that from such an impedance description the resonance conditions of the system can be derived.

Inserting the acoustic impedance into equation 2.23, one obtains:

$$Z_2 = Z_{char} \left[\frac{Z_1 - iZ_{char} \tan kd}{Z_{char} - iZ_1 \tan kd} \right] \qquad \text{eq. 2.25.}$$

In the case of an acoustic mirror comprising layers with a quarter wavelength thickness, the calculation of the acoustic impedance can be significantly simplified and one obtains for the impedance of the whole mirror [LAK95]:

$$Z_{mirror} = \left(\frac{Z_{char,1}}{Z_{char,0}} \right) \left(\frac{Z_{char,1}}{Z_{char,2}} \right) \left(\frac{Z_{char,3}}{Z_{char,2}} \right) \ldots \qquad \text{eq. 2.26.}$$

Mason model impedance

To solve for the electric input impedance, the boundary conditions have to be formulated. They consist of stress-free surfaces at the top and the bottom of the structure and of a sinusoidal electric potential at the electrodes. The boundary conditions of continuous stress and velocity at the layer interfaces are already contained in the acoustic impedance equations (2.25). By applying the boundary conditions, the Mason-model-equations follow (for a complete derivation see for example [LUT97]):

$$Z_{el} = \frac{1}{i\omega\frac{A\varepsilon}{d}\alpha}\left[1 - k_{33}^{t\,2}\alpha\left(\frac{\tan\left(\frac{kd}{2}\right)}{kd}\right)\beta\right] \qquad \text{eq. 2.27}$$

$$\beta = \left[\frac{(Z_{top} - Z_{bot})\cos\left(\frac{kd}{2}\right)^2 + iZ_{char}\sin(kd)}{(Z_{top} - Z_{bot})\cos kd + iz\left(1 - \frac{Z_{top}Z_{bot}}{Z_{char}^{\,2}}\right)\sin(kd)}\right] \qquad \text{eq. 2.28}$$

$$k_{33}^{t\,2} = \frac{\dfrac{e_{33}^{\,2}}{\varepsilon_{33}^{t}\mu}}{1 + \dfrac{e_{33}^{\,2}}{\varepsilon_{33}^{t}\mu}} \qquad \text{eq. 2.29,}$$

where d, Z_{char} are the thickness, material-impedance of the piezolayer, ε and c the dielectric constant and compliance of the piezolayer. Z_{top} and Z_{bot} are to be calculated according to equation 2.25. Z_{el} is the electrical input impedance. $k_{33}^{t\,2}$ contains the piezoelectric constant and describes the conversion from acoustic electric energy. It is also called electromechanical coupling. For a one layered resonator the impedance is simply the one in equation 2.27 omitting α and β ($\alpha = \beta = 1$).

BVD-model impedance

From the Mason model impedance a simpler, purely electrical model can be approximated. This is achieved by using the series expansion of the tangent function in the vicinity of the resonance. The following expression for the electrical resonance is thus obtained:

$$Z_{el} = R_s + \cfrac{1}{j\omega C_0 + \cfrac{1}{R_m + j\omega L_m - \cfrac{j}{\omega C_m}}} \qquad \text{eq. 2.30.}$$

An additional electrical resistance of the signal lines is assumed, adding R_s to the impedance, which is obtained as an approximation of the Mason model. The correspondent equivalent circuit is shown in figure 2.6. The piezoelectricity part is described by the motional arm with the elements R_m, C_m and L_m. The latter two elements describe the ability of the piezoelectric layer to convert energy into another form (with the difference that in the capacitor and the inductor the energy is stored in the electric and the magnetic field instead of the acoustic motion) and the resistor R_m describes acoustic losses. The capacitor C_0 describes the "real" electric capacitance which would also exist without any piezoelectric activity and is usually called "clamped" capacitance. The elements of the equivalent circuit can be determined from the fundamental parameters of the resonator. This is summarized in table 2.1.

Table 2.1: a) Relation between electric equivalent circuit parameters and the sensor material and geometrical parameters. b) Determination of resonance characteristics from the equivalent circuit elements.

a)

R_m	C_m	L_m	C_0
$\dfrac{1}{B}\dfrac{\eta}{\rho v_a}$	$B\dfrac{1}{v_a}$	$\dfrac{1}{B}v_a$	$\dfrac{\varepsilon_R \varepsilon_0 A \omega_0}{v_a \pi}$

b)

f_s	f_p	K^2	Q_p	Q_s
$\dfrac{1}{2\pi\sqrt{L_m C_m}}$	$f_s\sqrt{\dfrac{C_m + C_0}{C_0}}$	$\dfrac{f_p - f_s}{f_p} \cdot \dfrac{\pi^2}{4}$	$2\pi f_s \dfrac{L_m}{R_m}$	$Q_p \dfrac{1}{1 + \dfrac{R_s}{R_m}}$

$$B = \frac{8\varepsilon_R \varepsilon_0 K^2 \omega_a A}{\pi^3}.$$

The resonator shows the characteristic behaviour with a series and a parallel resonance. At series

resonance ($f_s = \dfrac{1}{2\pi\sqrt{L_m C_m}}$, see table 2.1) the impedance becomes real and shows a minimum

and takes a value which is at least the sum of series and motional resistance. With the help of the piezoacoustic wave the electric energy is flowing directly from one plate of the capacitor to the other. Electric storing in the capacitor C_0 is thus deactivated. The resonance circuit is shorted.

Both motional and clamped capacitance are proportional to the resonator area, whereas motional resistance and inductance are reciprocally proportional. The interrelation of these magnitudes and the corresponding influence on the resonator performance will be discussed in chapter 4.

At parallel resonance the acoustic impedance shows a maximum. In this mode of operation the opposite is happening compared to the series resonance: the energy exchange occurs between the motional arm and the C_0-arm, meaning that the piezoacoustic wave serves for reversing the polarity of the capacitor C_0. The energy stays in the resonator system and no energy exchange with the outside is taking place.
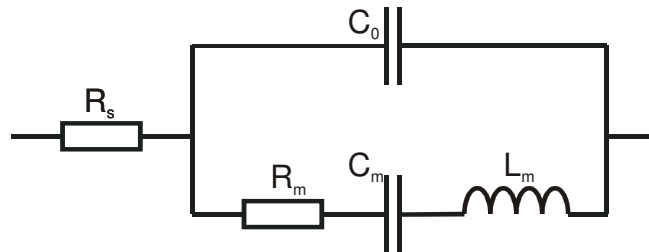

Figure 2.6: BVD-equivalent circuit.

2.4 Sensitivity

Sauerbrey [SAU59] has developed a model for the resonance frequency of a one layered resonator with a negligibly thin rigid overlayer. According to this model the relative change in mass and the relative change in frequency have the same magnitude (but opposite sign):

$$\frac{\Delta f}{f_R} = -\frac{\Delta m}{m_R} \qquad \text{eq. 2.31.}$$

As in this model the acoustic properties of the overlayer do not play any role, the change in mass can be equated to a change in thickness. Inserting the mass $m = d \cdot A \cdot \rho_R$ and using $d = \frac{v_{ac}}{2 f_R}$, the frequency shift of the system resonator-thin overlayer is obtained:

$$\Delta f = -\frac{\Delta m}{A} \cdot \frac{2 f^2}{\rho \cdot v_{ac}} \qquad \text{eq. 2.32.}$$

In most of the applications the mass loading consists of a thin layer attached, so using $\Delta m/A$ makes sense. Now consider the case, that the sensor is driven in an overmode with overmode number n. When the same frequency is assumed, the overmoded resonator will have n times the thickness of the resonator, that is driven in ground mode. Using the Sauerbrey argument (as expressed by equation 2.31), due to the greater mass of the resonator the frequency shift will be accordingly smaller:

$$\Delta f_n = -\frac{\Delta m}{A} \cdot \frac{2 f^2}{n \cdot \rho \cdot v_{ac}} \qquad \text{eq. 2.33.}$$

One may now assume a resonator with a certain thickness, which is operated at one of its overmode frequencies. With f_0 the ground mode frequency the overmode frequencies become $f_n = n \cdot f_0$ and the mode dependent frequency shift can be derived from equation 2.33 as:

$$\Delta f_{d=const}(n) = -\frac{\Delta m}{A} \cdot \frac{2 n f_0^2}{\rho \cdot v_{ac}} \qquad \text{eq. 2.34,}$$

so the sensitivity is increasing linearly with the mode number. Equation 2.34 is the interpretation of overmode sensitivity in the case of a constant thickness. Equation 2.33, on the other hand, describes the frequency change coming from constant frequency. This would be realized with resonators of different thicknesses, driving them in the accordant overmode. Hence, realizing a mass sensor at a given frequency as an overmoded device does not make sense from the point of view of sensitivity, because the sensitivity will decrease linearly with mode number.

Equation 2.31 only holds for a small mass loading Δm. To make this clear one may consider a one layered resonator with a thin layer of just the same material as the resonator itself. It is obvious then, that the relation of the overall mass to the resonator mass is just the same as the relations of the respective acoustic lengths: so the relation between mass loading and frequency is trivial:

$$\frac{\Delta m + m_R}{m_R} = \frac{f_R}{f_R + \Delta f} \qquad\qquad \text{eq. 2.35}$$

$$\text{or} \quad \frac{\Delta m}{m_R} + 1 = \frac{1}{1 + \dfrac{\Delta f}{f_R}} \approx 1 - \frac{\Delta f}{f_R} \qquad\qquad \text{eq. 2.36,}$$

so equation 2.31 is an approximation of equation 2.35 for small mass attachments. The condition for the Sauerbrey equation to hold thus is, that there is no significant acoustic propagation in the overlayer.

Lu and Lewis developed a model for a system comprising two acoustic layers. This model is exact for a two layer system when there is no damping in the overlayer. Because in this case, there is a significant acoustic propagation in the overlayer, the acoustic properties (namely the acoustic velocity) must be incorporated in the model. The system is described by:

$$\tan\left(\frac{\pi(f_0 + \Delta f)}{f_R}\right) = -\frac{\rho_f v_f}{\rho_R v_R} \tan\left(\frac{\pi(f_0 + \Delta f)}{f_f}\right) \qquad \text{eq. 2.37,}$$

where ρ_R, v_R and ρ_f, v_f are the mass density and acoustic velocity of the resonator and the overlayer respectively. Furthermore a „resonance frequency" for the overlayer itself was defined by

$f_f = \frac{v_f}{2d_f}$. Applying the first order series expansion of the tangents-function and assuming again

the same material of resonator and overlayer directly leads to equation 2.32, meaning that with this model the fact that the frequency changes is included in this model, whereas in the Sauerbrey model it is assumed so small, that it can be neglected.

2.5 Fabrication of c-Axis inclined ZnO

One of the main technological challenges in the development of an FBAR for application in liquid and biosensing was to develop a sputtering process to fabricate a C-Axis inclined ZnO-layer. As shown in section 2.2, this would allow for an excitation of acoustic transversal shear modes, enabling low loss operation in liquids (see chapter 6). A detailed description of this process is given in the work of Link [LINK2].

The setup is shown schematically in figure 2.7. A dc-pulsed magnetron sputtering facility by Von Ardenne Anlagentechnik is used with a pulse power of 100 W. The sputtering chamber is evacuated to 10^{-6} Pa and during deposition the heater temperature (being placed above the wafer) is adjusted to between 150 and 280 °C. Argon and oxygen gas is fed into the chamber and the pressure during the sputtering process is about 0.2 to 0.5 Pa. The distance between target and substrate is about 60 mm.

A blind made of stainless steel is placed next to the wafer (see figure 2.7). It has a height of between 15 and 35 mm. By conducting θ-2θ-scans with an X-ray diffractometer, the c-Axis inclination was measured along the wafer surface. A c-Axis inclination was found in the vicinity of the blind with a maximum at about 5 mm distance from the blind. The inclination there was about 16° with a full width at half maximum of 13°. The inclination was always found to be directed away from the blind. Immediately below the blind almost no inclination is found and inclination is also declining towards the wafer edges.

To optimize the process, different seed layers, blinds of different sizes as well as a variation of the sputtering temperature have been evaluated. The choice of an appropriate seed layer is critical and with some seed layers such as platinum the ZnO-layer was showing no inclination at all. The c-Axis inclination could be explained by oblique particle incidence. A cosine form of the angle distribution of the particles leaving the target can be assumed. In simulations the distribution of the mean angle of particle incidence over the wafer was determined. It was found to be qualitatively the same as the c-Axis inclination with the direction of inclination pointing away from the blind. So the c-Axis inclination can indeed be explained by the direction with which the particles impinge onto the wafer.
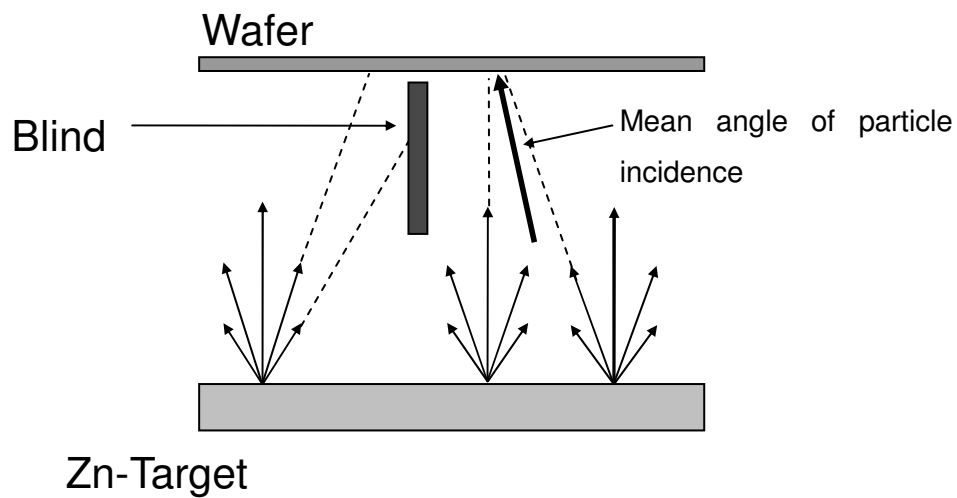

Figure 2.7: Sputtering setup applied for fabrication of the C-Axis-inclined ZnO-layer: through shadowing of the particle flow an oblique particle incidence respect to the surface normal is obtained. This leads to a c-Axis-inclined growth of ZnO.

3. Acoustic Mode Structure

In this chapter the mode structure of the resonators will be analyzed. The modes will be classified into two types. The first type are modes with the propagation direction of the acoustic wave vertical to the resonator surface. They will be referred to as vertical modes. The second type will be modes that propagate laterally to the resonator surface and will be called lateral modes.

Vertical modes depend on the vertical structure of the sensor i.e. the sequence, thickness and the materials of the layers used. So they are determined by the resonator design. In most publications the solidly mounted transducer is divided into the so-called resonator, a term that refers to the electrode layers and the piezoelectric layer, and the acoustic mirror. But unlike most of the mirror-resonator configurations known from laser physics for instance, the resonator and mirror can not be separated so clearly. This is because the resonator and the mirror have thicknesses that are about in the same order of magnitude. For this reason, the vertical modes do not appear to be whole-number multiples of the ground mode any more. The layer structure of the sensor will be analyzed in section 2.1 and a considerable impact of the vertical modes on the sensor sensitivity will be found.

Lateral modes on the other hand have an important impact on resonator performance. They originate in the lateral conditions. As mentioned before, the FBARs investigated here usually have a large width compared to resonator thickness. As a consequence the lateral resonances will be correspondingly narrower spaced than the longitudinal resonances. This can lead to a perturbation of the measurement.

Lateral resonances can be described to have their origin in the resonator edges, which are usually free. When these edges are deflected, a wave will be generated and will propagate across the resonator. Being reflected at the opposite edge, this gives rise to a formation of standing waves [LAK03]. The FBARs investigated in the scope of this work can show pronounced lateral modes at resonator sizes of 70 µm, corresponding to an aspect ratio of as much as 100:1. At these sizes the lateral resonances have a spacing of only a few MHz and therefore may interfere with the measurement, because the evaluation circuit is not able to lock in on one special mode. Especially when FBARs are developed with the scope to provide disposable sensing devices, production costs become a critical issue. For semiconductor processes costs scale directly with the area that is occupied on the wafer. Hence, it is desired to decrease resonator area. A target value for the resonator area may be in the vicinity of (10 µm)², a value that would still allow the integration of sensor, CMOS evaluation circuitry and functionalization.

In the development of FBAR-filters, several approaches have been followed to minimize or suppress lateral modes [LEE04]. One is the so called lateral edge enforcement. An additional layer is applied, enforcing the edges of the resonator and serving as a propagation barrier for the lateral modes [KAI03]. Another concept consists of applying a soft material outside the resonator. The lateral waves will propagate into this material and are absorbed there. Another concept, called "apodization", is based on giving the resonator an asymmetrical shape. Different acoustic lengths lead to a smearing out of the lateral resonances [LIN05].

However, the requirements for mass sensors and filters are quite different. Whereas for a mass sensor the sensitivity has to be maximized, meaning that the impedance phase at the point where the sensor is read out should be as steep as possible, for a filter it must be guaranteed that the insertion loss in the pass band does not exceed a certain value. For mass sensors this is only critical when the risk of "resonance hopping" exists. If the lateral resonances on the other hand are so weak, that this possibility does not exist, it does not make any sense to apply the above mentioned strategies of smearing out or damping the lateral resonances.

Another strategy may be thought of in order to handle the problem of lateral modes. The resonator could be made so small, that the intervals between the modes increase. Lateral dimension should therefore be in the order of magnitude of the thickness of the resonator. The latter is somewhere below 1 µm, so this method will be very demanding regarding technology as well as resonator design.

3.1 Vertical Modes

In order to investigate the vertical mode structure of the resonator, the one dimensional electro-acoustic model introduced in chapter 2 will be used. It will be shown in chapter 4, that these simulations match the measurements very closely. The aim of the simulations is to get an idea of the impact of the respective sequence of layers on the sensitivity of the sensor. Furthermore it will be shown, that by dimensioning the layers appropriately, different modes may even be exploited to expand the functionality of the sensor.
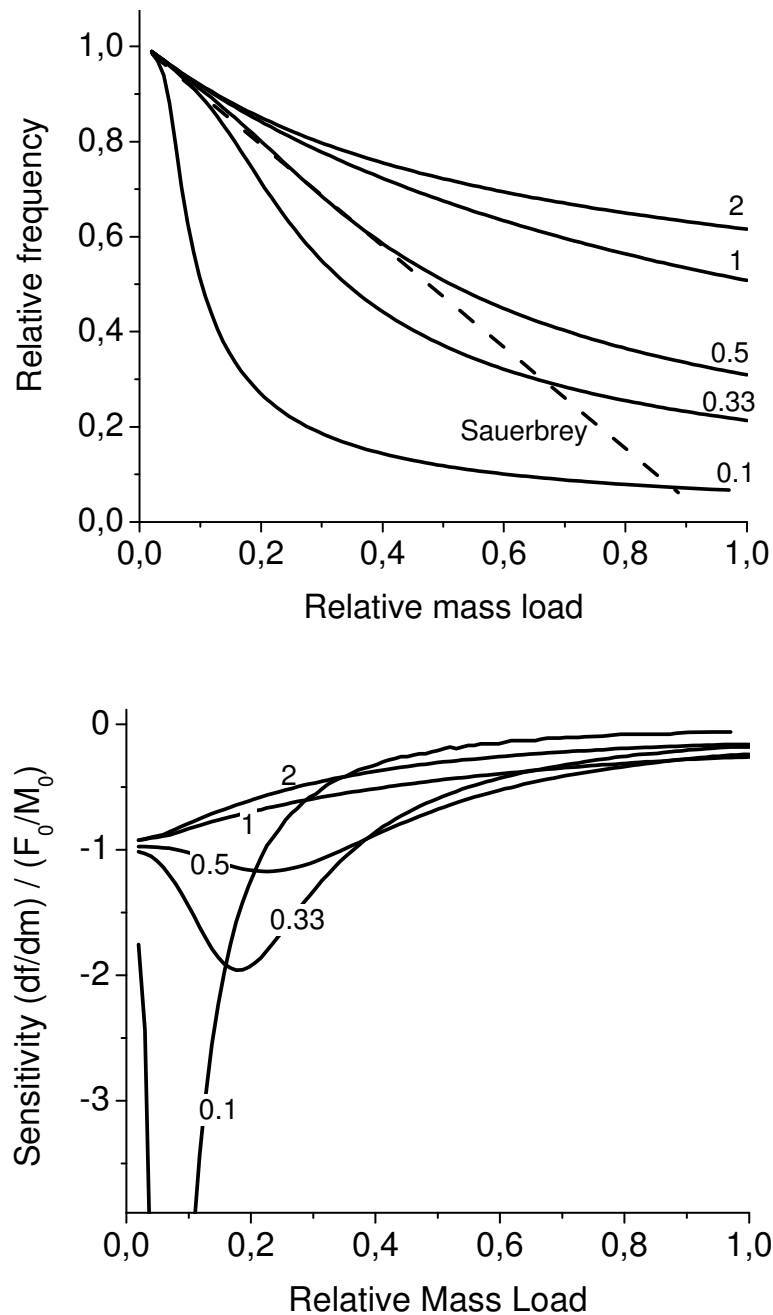
Figure 3.1: Simulated frequency change (above) and sensitivity (below) of a resonator with huge mass loads of different acoustic velocities relative to the velocity of the resonator. The mass density of the whole system is assumed to be homogenous. For the acoustic velocity being the same for the resonator and the overlayer, the sensitivity matches the Sauerbrey value at the beginning and decreases to a quarter the initial value when the overall mass is doubled. When the acoustic velocity is very low, there is a region of a strongly increased sensitivity followed by a section where sensitivity is lower. This provides an efficient method to enhance the sensitivity of the device.

First the sensitivity of the sensor will be studied. A simplified system comprising a resonator layer with thin electrodes and an overlayer will be considered. From the equations describing the input impedance of the system the resonance frequencies are extracted taking the respective minimum of the impedance magnitude (series resonance frequency). Then the layer structure will be extended and the impact of the acoustic mirror will be studied. The parameters used to obtain the results in this section are summarized in the appendix.

In chapter 2 it was mentioned, that a mass loading, which is non negligible compared to the resonator thickness itself, causes a deviation from the linear Sauerbrey behaviour. This is already evident with a homogenous system with a resonator and overlayer having exactly the same acoustic properties, where the resonance frequency is inversely proportional to the overall mass. In the investigations that follow, the change in sensitivity resulting from a variation of the acoustic impedance of the overlayer, will be examined.

Influence of the impedance ratio

A simplified layer stack with a homogenous acoustic impedance will be taken as a starting point. The acoustic impedance of the overlayer (the layer on top of the resonator, which is usually the measurand) will then be varied and the impact of the impedance ratio between resonator and overlayer on the sensitivity determined. The Mason model is used with the material properties of ZnO. All layers are assumed to have the same properties and the acoustic velocity of the overlayer is varied. The result is shown in figure 3.2. The upper graph shows the frequency shift to be greater for smaller acoustic velocities. A range of mass attachments is shown up to an overlayer mass identical to the resonator mass itself. For the same acoustic velocities of resonator and overlayer the frequency decreases to half with doubling the overall mass as expected. The correspondent sensitivity is decreasing by a factor of four.

For low acoustic velocities of the overlayer the frequency response starts similarly for small mass loads and then gives rise for a steep decline. For an acoustic velocity of the overlayer of 10% the acoustic velocity of the resonator and a mass attachment of 6% the resonator mass the mass sensitivity is thus increased by factor 9. Such low acoustic velocities are not unrealistic as will for instance be shown in chapter 7, where the acoustic velocity of a suspension of carbon nanotubes being deposited on the resonator was determined to 80 m/s. This is even 70 times lower than the acoustic velocity of ZnO. So the sensitivity of the sensor can be enhanced by an intermediate layer with a low acoustic velocity with a certain thickness. When only little mass is added, again the frequency shift should be independent of the acoustic velocity of the layer being measured.
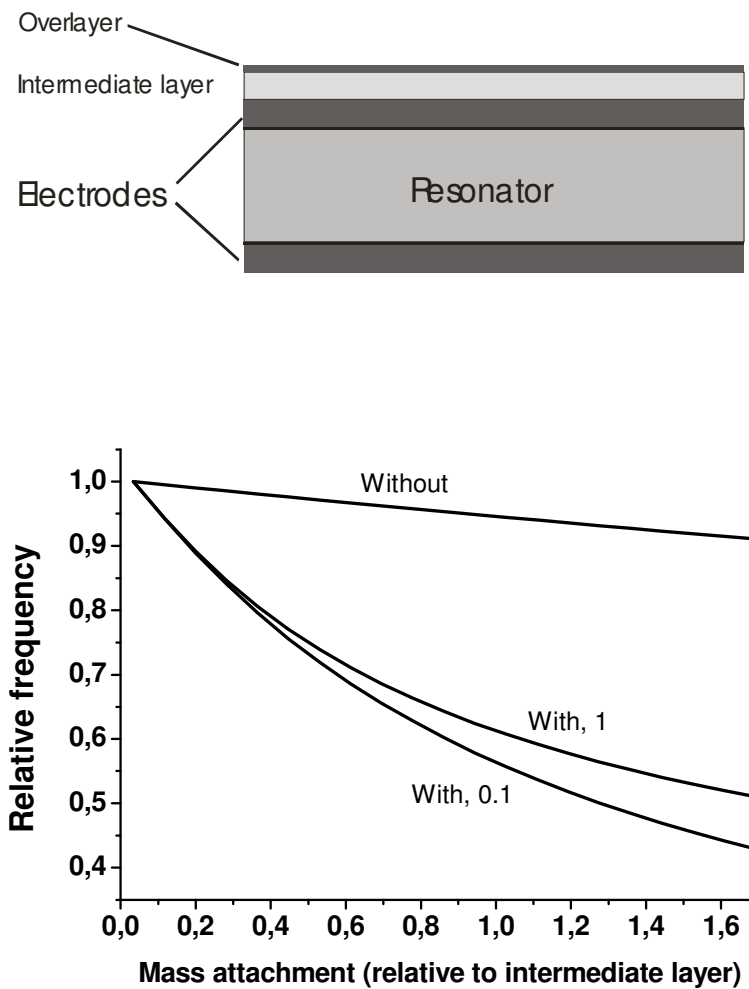
Figure 3.2: Above: Setup of a resonator with an intermediate layer with low acoustic velocity for sensitivity enhancement. Below: normalized frequency versus overlayer thicknesses for a resonator with and without an intermediate layer. The intermediate layer has an acoustic velocity of 0.1 times the resonator acoustic velocity and a thickness of 6% the resonator's thickness. For the overlayer an acoustic velocity of 0.1 and 1 times resonator acoustic velocity was applied. With the intermediate layer the frequency shift is non linear but sensitivity is greater in the whole range up to mass attachments 1.6 times the intermediate layer.

To test this, further simulations with the Mason model are carried out. The stack was the same as above with the resonator layers and the electrodes having the same acoustic properties. Additionally an intermediate layer applied with a thickness of 6% of the resonator. This would correspond to 60

nm for a resonator of 1 μm thickness. In figure 3.2 the result is shown for a resonator with and without an intermediate layer. For the overlayer an acoustic velocity of ZnO and 0.1 times ZnO was used respectively. The frequency response of the sensor with intermediate layer is about 11 times higher in the beginning. The resonator without any intermediate layer has a pretty linear response to the overlayer. With intermediate layer the response, however, is strongly nonlinear. Interestingly, even with an overlayer 1.6 times the intermediate layer the frequencies for both overlayer acoustic velocities lie quite close together compared with the frequency of the resonator without an overlayer. So the acoustic velocity of the intermediate layer has clearly a stronger impact than the acoustic velocity of the overlayer. This is of great benefit, as the acoustic velocity of the overlayer is not always known.

The system investigated so far was a very simple one, comprising only the piezoelectric layer and the electrodes. This corresponds to a structure as it would be applied in a membrane type resonator. In the following, the influence of the acoustic mirror shall be investigated.

Acoustic mirrors

As described in chapter 2, the acoustic mirror consists of a sequence of layers of alternating acoustic impedances. So the mirror is a periodic structure. Just as gratings in optics or the interdigital transducers in surface acoustic wave devices, this acoustic mirror, being periodic in space, constitutes a selection condition for the acoustic wave. In the case of interdigital transducers the periodic structure is actively generating the surface acoustic wave with the distance between two fingers matching half a wavelength. The acoustic mirror on the other hand is passive and has a maximum reflection, when the wave inside one mirror layer has a quarter wavelength.

This can be seen in the resonance characteristic shown in figure 3.3. Two configurations are compared, one with only the resonator and the electrodes (this would realized be as a membrane) and one "solidly mounted" on a substrate and with a mirror in between. The resonator was assumed to have a thickness of 600 nm and the acoustic impedance of ZnO and the substrate to have a thickness of 20 μm and the same acoustic impedance. An acoustic mirror of alternating layers with double and half the acoustic impedance was applied having thicknesses of 600 and 150 nm in accordance with the reflection condition. The main resonance is at about 7 GHz for both resonators and it is seen very nicely that at half the resonance frequency the mirror becomes transmitting and therefore substrate resonances can be observed.
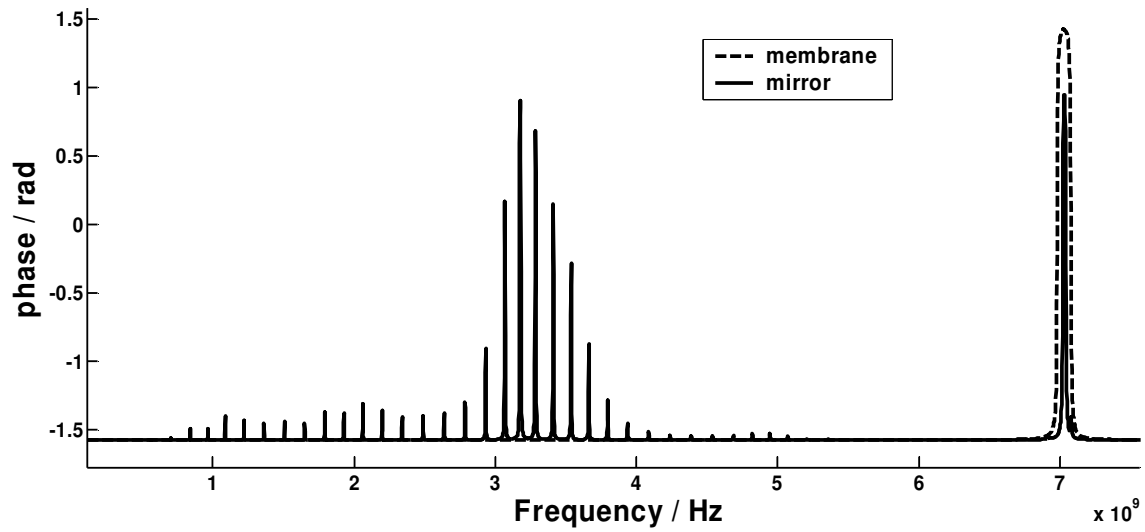
Figure 3.3: Simulation of the impedance phase for a resonator with a mirror, solidly mounted on the substrate and for a membrane type resonator.
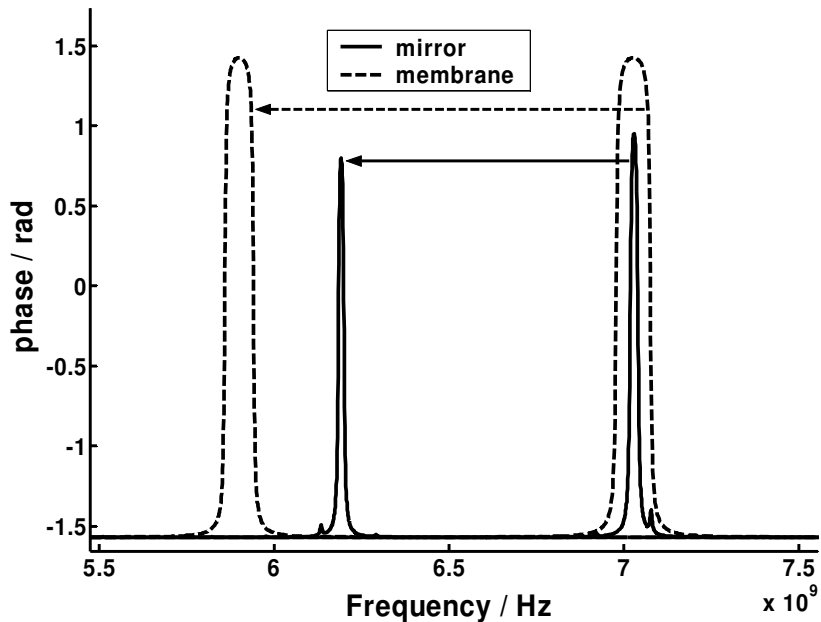

Figure 3.4: Influence of the mirror on the resonance frequency: when the same percentage of material is added to the resonator layer, in the case of the solidly mounted configuration the resonance shift will be smaller. This is because the acoustic mirror is not only a reflector but also a resonance frequency determining element.

In most resonator-mirror configurations the resonator is much larger than the mirror. In these cases the resonance frequency will be determined only by the resonator dimension itself. In the case of the FBAR however both the resonator and the mirror layers have a comparable size. Adding a certain percentage to a resonator in membrane configuration will shift the frequency by the corresponding amount. When the same amount is added to the resonator layer of a mirror configuration resonator the shift is smaller. This is seen in figure 3.4, where a layer was added on top of a membrane and a mirror type resonator, respectively. It had a mass of 16 % of the top electrode, piezoelectric and bottom electrode layers together. The resonance of the membrane type resonator shifts by 16 % (as expected) and the mirror type only by 12 %. The acoustic mirror is not only acting as a reflector but also partly as a resonance frequency determining element.

Now the nature of the overmodes observed around 3.5 GHz in figure 3.3 will be investigated more closely. They have a spacing of 124.8 MHz and have been classified as wafer modes, meaning that the acoustic mirror is transparent so that the acoustic wave can travel through and the acoustic wave is reflected from the backside of the wafer. In the simulation the "wafer" was assumed to have a thickness of 20 μm. In reality it will be much thicker, the modes will therefore be correspondingly narrower spaced.

Now some mass is added on top of the resonator with the mass density of this additional layer being the same as the resonator and the thickness reaching up to 800 nm. In figure 3.5 the result of this simulation is shown for thicknesses between 430 and 800 nm. As expected (and was already explained in chapter 2.4, see for instance equation 2.33) the overmode resonances have a very low sensitivity and the frequency shift is very small accordingly. Nevertheless, there are regions, where the sensitivity (that is, the frequency shift per thickness variation) is strongly enhanced. With decreasing acoustic mode frequency these regions are shifting towards greater electrode thicknesses.

Obviously, there is an anticrossing taking place. Anticrossing is a well known effect in all areas of physics. It implies, that two energy states form a superposition in a region where they would otherwise cross energetically. In the case observed here, a "resonator-mode" crosses a "wafer-mode". The former is the mode, whose energy is concentrated in the resonator layer, and the wafer-mode has its energy distributed across the whole wafer. According to the considerations in chapter 2.4, the resonator-mode has a much higher sensitivity. To illustrate the anticrossing, the resonator-mode was modelled (similar parameters as for the membrane type resonator were used) and was added to the plot (dashed line). As the resonator mode crosses the wafer mode, a superposition forms in the crossing region. Such an anticrossing is possible, because both resonances can exist at the same

time. This implies, that the mirror is partly reflecting, letting pass one part of the acoustic energy and reflecting the other part.

Interesting applications arise from this characteristic. Looking at a certain top electrode thickness, some modes appear more sensitive (namely those which are in the crossing region) than others. This may be exploited for instance, to distinguish between a frequency change, that is due to a mass change, and one that is caused by a change of intrinsic properties of the resonator.
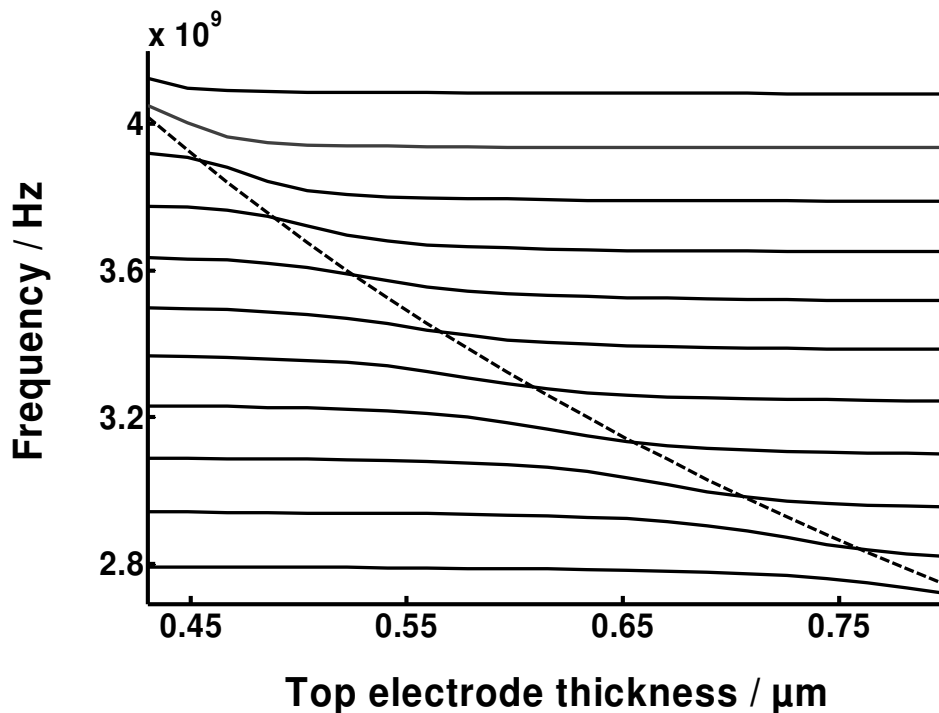

Figure 3.5: A structure as in figure 3.3 is considered and the modes in the non reflecting region of the mirror regarded. The thickness of the top electrode is varied. An anticrossing can be observed with the resonator mode (dashed line) crossing the wafer modes. This is similar to the superposition of energy states in particle physics. It gives rise to the emergence of modes with high and low mass sensitivity and can be exploited to differentiate between a change in mass and the intrinsic properties of the resonator.

3.2 Lateral Modes

In this section, lateral modes will be investigated. Up to now our sensor system was regarded as essentially one dimensional. Nevertheless, some perturbations arise from the edges of the resonator and can be observed in the resonance characteristic. In contrast to the previous section, the approach will be experimental and it will be tried to classify the nature of the lateral modes from the resonator electric impedance.
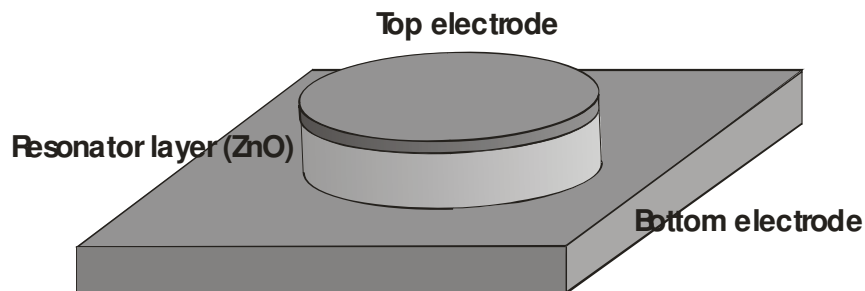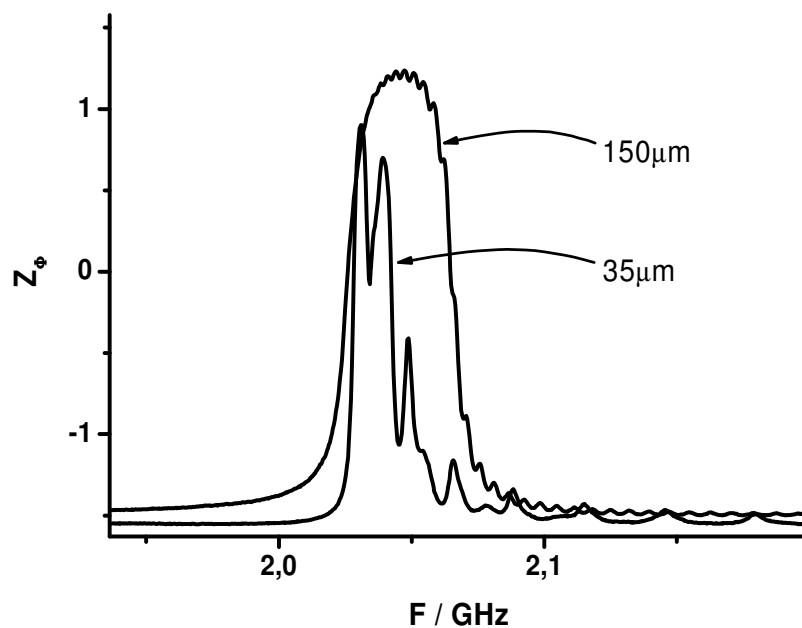

Figure 3.6: Resonance characteristics of two resonators with identical layer structure but different lateral dimension. They have a circular shape and a structure with a patterned resonator layer and top electrode solidly mounted on the (unpatterned) bottom electrode and mirror layers as shown below.

Description

Consider the impedance characteristics shown in Figure 3.6. They were obtained from two 2 GHz resonators. The resonators have a circular shape and a structure with a patterned resonator layer and top electrode as shown in figure 3.6 below. The mirror layers below were not patterned, only the bottom electrode was partially patterned in a square of $(400\mu m)^2$.

The vertical layer structure of the resonators is exactly the same. The difference is only in diameter which is 35 and 150 µm respectively. Three principle features can be observed. First, the lateral resonances are much stronger in the case of the smaller resonator. So the aspect ratio plays an important role for the amplitude of lateral modes. Secondly, they are wider spaced in the 35 µm case. This is a confirmation for their provenience from the lateral extent. Finally, there are no lateral resonances seen left of the main longitudinal resonance. This is a clear indication that the lateral resonances are directly linked to the longitudinal resonance. There exists only a ground longitudinal resonance and a longitudinal resonance combined with lateral resonances.
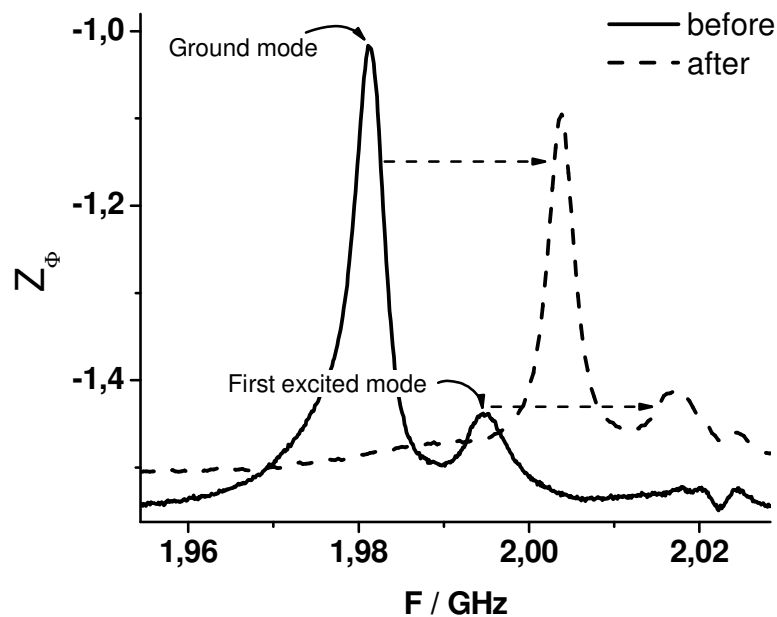
Figure 3.7: Resonance characteristic (impedance phase) for a 25μm, 2 GHz resonator before (solid) and after deposition (dashed) of a thin layer of about 20 nm of carbon nanotubes. The lateral resonance 13.5 MHz above the main resonance is shifting parallel with the main resonance providing evidence that the lateral resonance is directly coupled to the longitudinal resonance.

The resonances observed can therefore be regarded as excited states of a ground state, which is a more or less pure resonance. To demonstrate this, consider figure 3.7. The impedance characteristic of a resonator with the same vertical structure as before, a quadratic shape and a lateral extent of 25 µm is shown. It has its main resonance at 1.98 GHz. An additional resonance is seen about 13.5 MHz above the main resonance. This resonance only occurs for the resonator with this lateral size but not for other resonators that have the same vertical layer stack. Hence, it can be identified as a lateral resonance providing from the resonator edges. After the first measurement (solid line) a thin layer of carbon nanotubes of about 20 nm was applied. Due to the acoustic properties of this layer the resonance is showing a significant frequency shift of about +22 MHz (these measurements are discussed more in detail in chapter 7). It is seen quite clearly, that the lateral resonance is also shifting by the same magnitude. This means that it is directly coupled to the main resonance. The lateral resonances can thus be regarded as excited states of the main resonance.
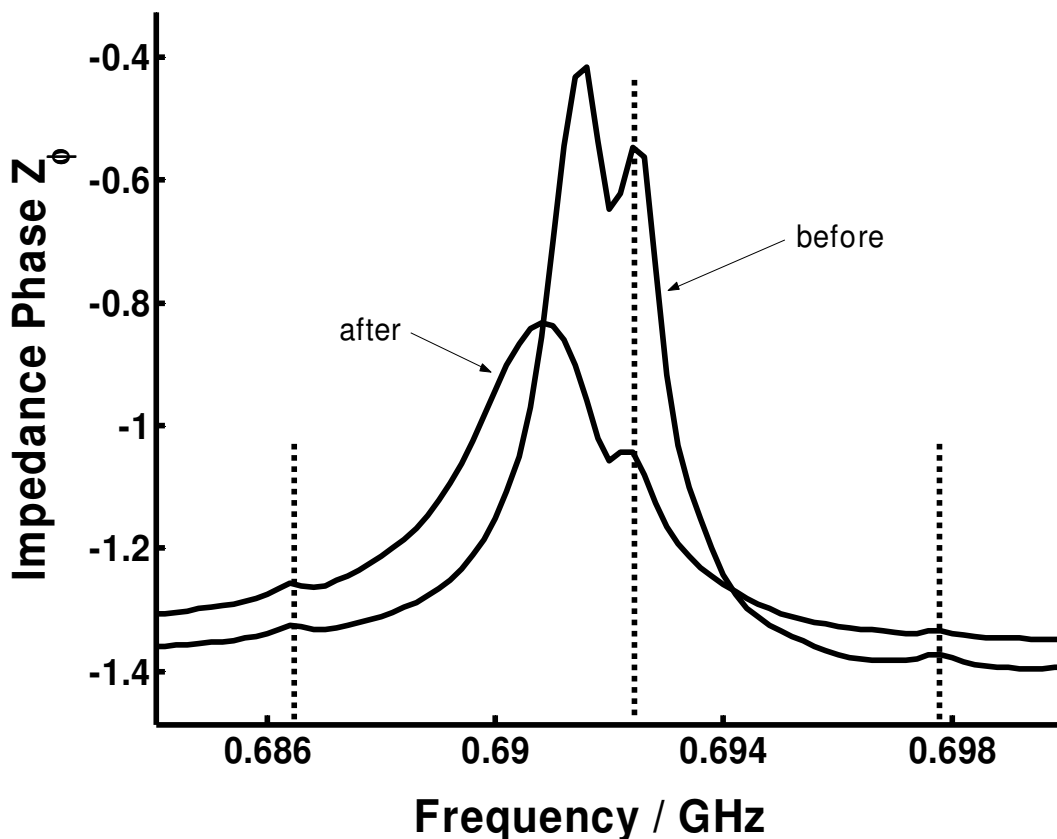

Figure 3.8: Wafer resonances of a pure shear mode resonator in water and with a mass attachment (vesicles, see chapter 7). The resonances stay in the same place, meaning that they are independent of the main FBAR resonance.

This is in contrast to the modes that occur, when the longitudinal waves are reflected from the bottom of the silicon substrate, the so-called wafer modes. They are observed in overmoded resonators (see chapter 2) or in a resonator whose acoustic mirror is not working properly. Figure 3.8 shows the resonance characteristic of a shear mode resonator operating at about 600 MHz. Three spikes are observed with a spacing of about 6 MHz respectively. This spacing corresponds to half the wavelength of the shear mode in 500 am thick silicon substrate. A mass sensor experiment with this resonator was carried through with the adsorption of lipid vesicles (see chapter 7). Due to this mass attachment a frequency shift by about -1 MHz occurs. Nevertheless, the wafer resonances do not shift as significantly as the main resonance. This is a clear indication that the overmodes of the ground wafer mode are independent of the main resonator mode. They are stronger, however, in the vicinity of the main resonance so they are associated to the main resonance but they are no excited resonances of the main resonance.
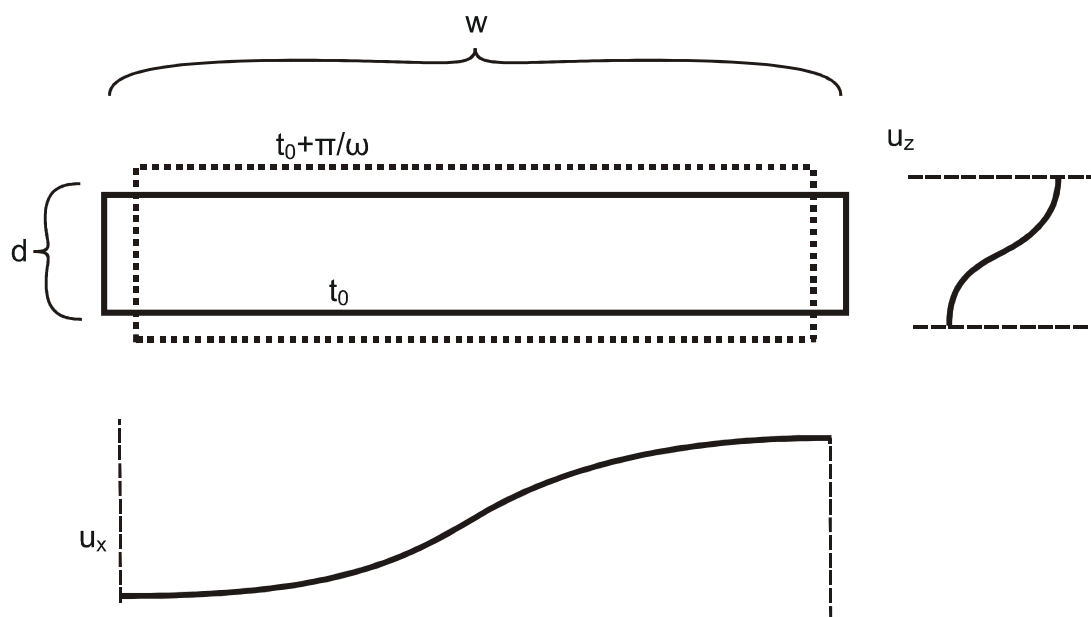

Figure 3.9: Model of the plate vibration: a longitudinal vibration is excited electrically and due to the poisson ratio a secondary lateral vibration takes place which in the ground mode has the same qualitative distribution of the deflection. This lateral deflection causes lateral waves to run across the resonator and lateral overmodes can be observed.
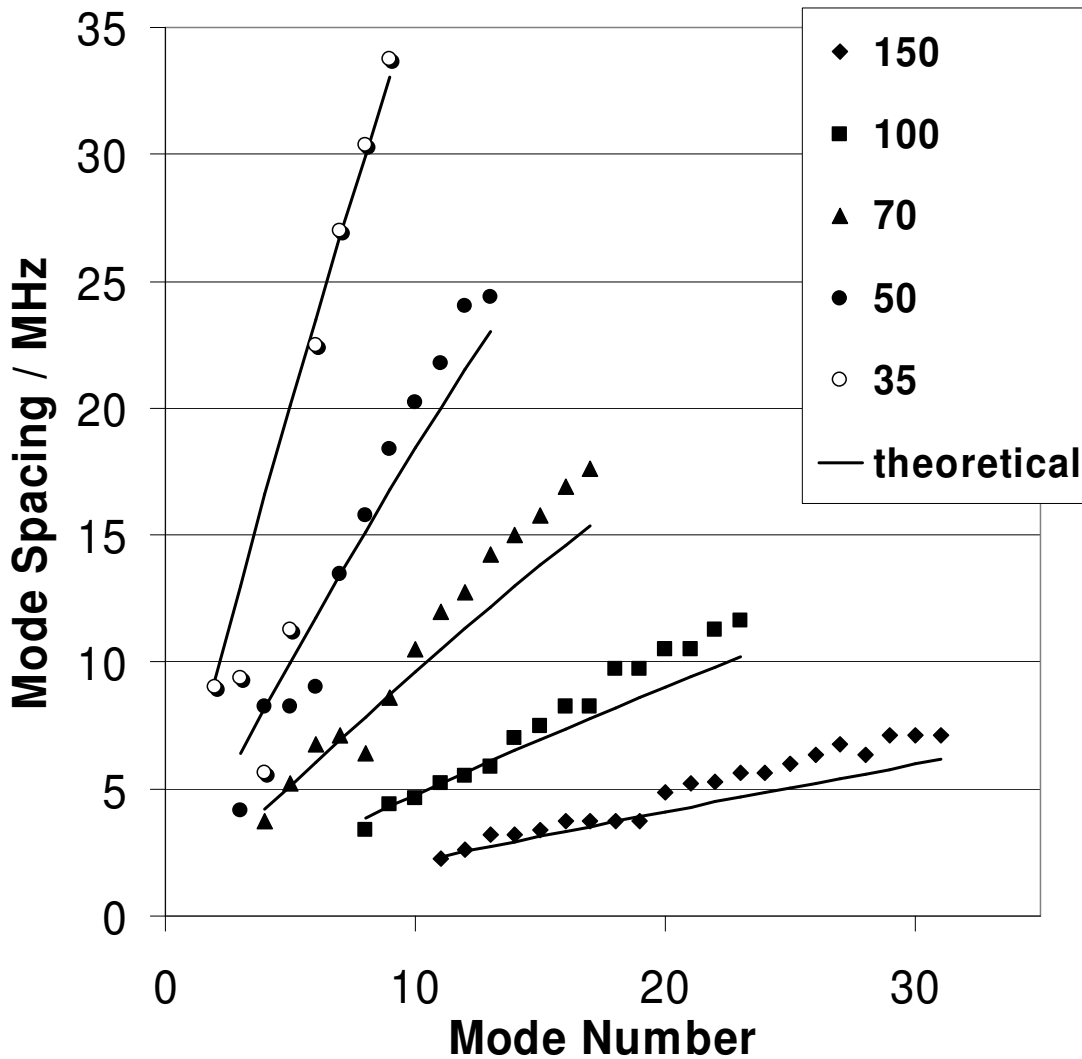
Figure 3.10: Mode spacing determined for completely patterned resonators with circular shape and different lateral extensions. Spacing increases with mode number as well as with decreasing lateral extension, the latter clearly indicating their origin as lateral modes. The lines show the values obtained theoretically with equation 3.3, inserting the acoustic properties of ZnO, proving the validity of the model and the extensional nature of the modes.

Now the resonance frequencies of the lateral resonances will be derived. The resonator is assumed to have the form of a simple plate. This is shown schematically in figure 3.9. A longitudinal vibration is assumed with the frequency given by the longitudinal resonance. The resonator is no more one dimensional, but being cut off in lateral direction, having an extent of w. The resonator edges are free and can be deflected. So there will be a deflection in x-direction, which is described by the

poisson ratio σ (see chapter 2). This deflection is directly caused by the longitudinal deflection u_x. It is greatest at the resonator edges (because they are free) and will be zero at the center of the resonator. So u_x will just have the same form of a half wave as the longitudinal resonance. Without any longitudinal deflection, also this plate extension would not occur. Now this lateral deflection causes a wave to propagate across the resonator (note that in the case shown in figure 3.9, there is no such wave in lateral direction, u_x is just linked to u_z). Then there will be further resonances when a multiple of half the wavelength matches the resonator extension.

Describing the longitudinal and lateral resonances separately yields:

$$f_{long} = n\frac{1}{2d}\sqrt{\frac{c_{33}}{\rho}} \quad \text{and} \quad f_{lat} = m\frac{1}{2w}\sqrt{\frac{c_{11}}{\rho}} \qquad \text{eq. 3.1}$$

with n and m the respective mode numbers. The c-axis is assumed to be in growth direction and the main resonance is assumed to be longitudinal, therefore c_{33} is chosen for the longitudinal and c_{11} for the lateral resonance.

According to [MAN89] the combined frequency of the plate will then be:

$$f = \sqrt{f_{long}^{2} + f_{lat}^{2}} \qquad \text{eq. 3.2,}$$

which leads to the resonance frequency of the resonator:

$$f_{nm} = \frac{1}{2\sqrt{\rho}}\sqrt{\frac{c_{33}n^{2}}{d^{2}} + \frac{c_{11}m^{2}}{w^{2}}} \qquad \text{eq. 3.3.}$$

Because of the quadratic dependence on mode number in the square root, the mode spacings between the lateral modes (second term in the square-root) are expected to increase linearly. In figure 3.10 the mode spacings of the overmode resonances are shown. They were determined from the impedance phase of the resonance (such as shown in figure 3.6) by picking the peak positions. Indeed they show the linear increase with mode number that was expected from equation 3.3.

The spacings of the resonance frequencies were also calculated with equation 3.3. The thickness d was determined from the ground resonance, assuming the lateral mode number m=0. For the lateral modes the compliance c_{11} of ZnO was used and the respective resonator width.

These theoretical values are plotted as lines in figure 3.10. Indeed they match quite closely the measured values when the appropriate mode numbers is chosen. So the lateral modes have a direction of propagation and deflection in lateral direction and can be denominated as thickness extensional modes.
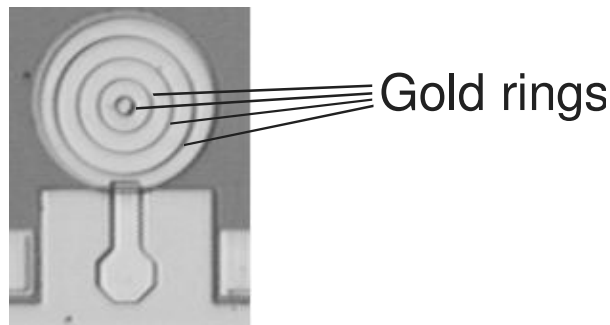

Figure 3.11: A 150 μm resonator with four gold rings.

More interesting features are observed. The larger the resonator, the bigger the mode number of the first mode which can be identified. This is mainly for the reason, that the modes are very closely spaced in vicinity of the ground mode. With increasing lateral extent of the resonator this spacing becomes closer according to equation 3.3. Therefore it is less probable to dissolve the resonances. In addition to the closer spacing the resonances of the larger resonator are also less pronounced. Furthermore the lateral resonances lie in the rising edge of the main resonance, which is another reason making it harder to dissolve the low mode resonances.

Further experiments where carried out in order to investigate the lateral resonances. Small rings of gold with a width of 2 μm and a thickness of about 100 nm were deposited onto the gold electrode[3]. They were concentric and had different diameters, depending on the respective resonator. A photo of these rings is shown in figure 3.11.
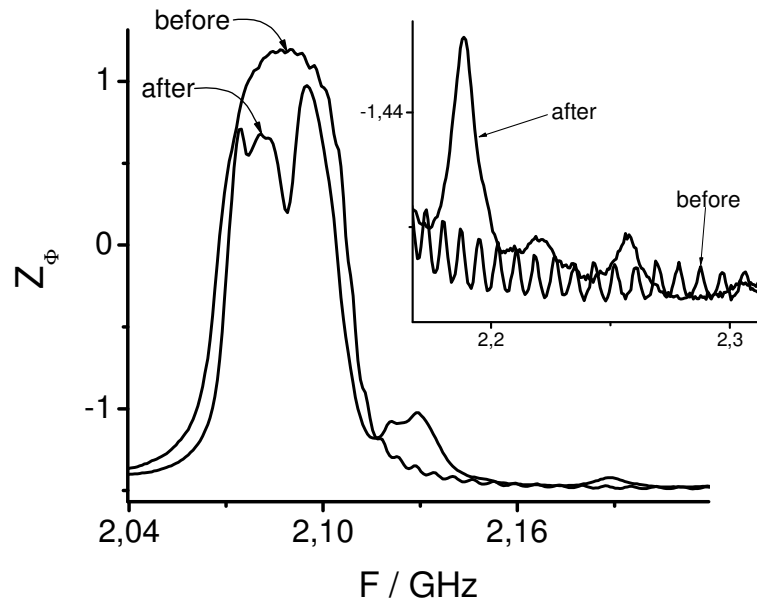
Figure 3.12: Resonance of a 150 μm resonator before and after deposition of four gold rings.

Figure 3.13: Schematic form of the first lateral mode observed. The mode type is thickness extensional. Because the resonator is clamped onto the substrate, most of the energy is close to the resonator surface and therefore the lateral modes are easily manipulated by a surface mass load.

---

[3] Processing was done with electron beam lithography by Jens Ebbecke at Universität Augsburg

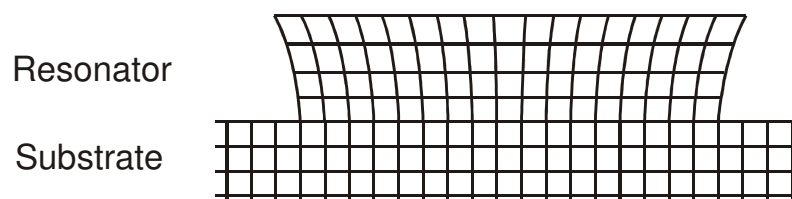Aim of this experiments was to investigate the propagation conditions of the lateral modes and to find out, if it would be possible to select and emphasise certain lateral modes. With four rings having a diameter of 10, 40, 70 and 100 μm only 0.05 % of the resonator was covered which is equal to a mass load on the resonator corresponding to a homogenous layer of 0.05 nm. So the mass load can be regarded as negligible.

In figure 3.12 the impedance phase of a resonator with four rings is shown before and after deposition. In the inset, the part right of the resonance is zoomed in. Especially in that part it is seen very clearly, that the lateral resonances are strongly disturbed by the gold rings. Some resonances vanish completely, whereas others appear strongly amplified. Hence, a structure on the resonator surface, though very small in absolute mass, has a strong impact on the propagation of the lateral resonances. This leads to the assumption, that probably most of the lateral mode energy it close to the surface. The rings make the surface more inert and a resonating mode is favoured with vibration nodes at the ring positions. For all 150 μm resonators with four rings the quality factor taken from the maximum slope of the rising edge of impedance phase shows to be slightly improved after ring deposition. The average Q_s is up from 174 to 201. The specification of a certain propagation condition with the rings results in a better quality factor. In the next section, more will be learnt about the impact of the lateral resonances on resonator performance.

Figure 3.13 shows the schematic picture of the first lateral resonance as it results from the investigations presented before. The lateral vibration is thickness extensional and the clamping of the resonator to the substrate leads to the deflection to be negligible near the substrate and increasing towards the resonator surface.

Finally, the impact of liquid on the propagation of the lateral resonances was tested. In figure 3.14, this is shown for a resonator having 25 μm width. The lateral resonances are very well pronounced when the resonator is measured in air. As they are of thickness extensional type, the interaction between the lateral resonances at the resonator surface and the water is expected to be a viscous one. Therefore, the damping should be quite small (see chapter 6). Nonetheless, the resonator immersed in water does not show any lateral resonances at all. This is even more evident when considering the weak resonance left from the main one (at about 2.03 GHz). This resonance certainly originates from the vertical structure of the resonator (lateral resonances only occur associated with longitudinal resonances as shown before). Although it is less pronounced than the lateral resonances in air, it does not vanish in water. The reason for this may be, that with water the lateral resonances are not

trapped any more. They are not any more reflected at the edges but propagate into the water, where they will be absorbed.
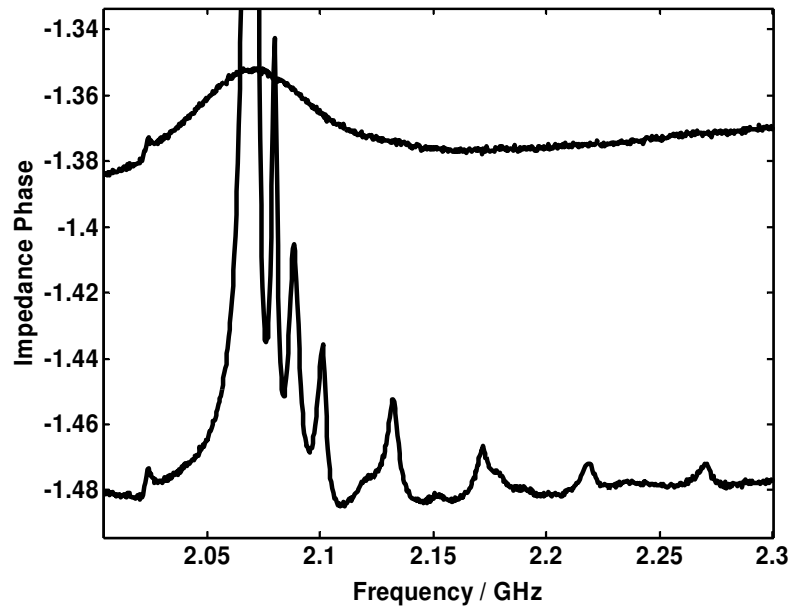

Figure 3.14: Impedance characteristic of a resonator with 25 um width in air and in water: immersion into water causes the lateral resonances to vanish completely. Below the main resonance an additional resonance is observed, that may originate from the vertical structure. Although this resonance is very weak, it is not completely damped out by the immersion into water.

Impact on Resonator Performance

It is useful to know, what exactly is the impact of lateral modes on resonator performance. Consider again figure 3.6. Some principle features regarding the nature of the lateral resonances have already been discussed. There is yet another interesting feature: Especially in the case of the smaller resonator (35μm) the lateral resonances are quite narrow and sharp. Especially when the quality factor is determined from the slope of the impedance phase it is higher for the smaller resonator (517 to 230). As will be discussed in chapter 4, this may also be due to the electrical series resistance. Nevertheless it is useful to know, which effect lateral resonances will have on the resonator performance.
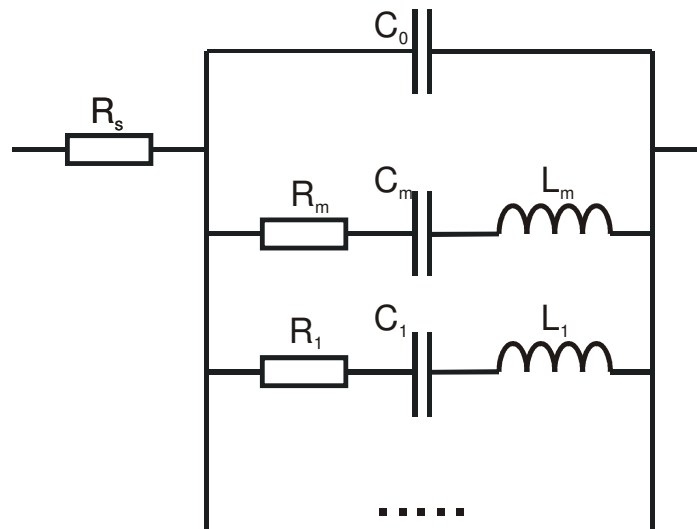
Figure 3.15: Multimode BVD-model for the analysis of the quality factors and couplings of the lateral resonances. Each branch represents one resonance.

The resonances were therefore analysed with a multiple resonance BVD-model [ROS88]. With this model one can try to get an idea of the influence and strength of the lateral overmodes. Especially will it be interesting to learn, which is the amount of energy stored in these modes. To achieve this, the multimode BVD-model from figure 3.15 was fitted to the measured values. The large number of parameters to be fitted (3 parameters for every mode plus 4 for the main mode) exceeds by far the number that can be fitted with conventional fitting algorithms. Therefore a semi-manual approach was chosen, obtaining a rough fit for the main resonance with the Levenberg-Marquardt algorithm and adding the lateral modes afterwards. In figure 3.16 the impedance magnitude for a resonator with circular shape and a diameter of 150 μm is shown[4]. Initial values for the quality factor and the electromechanical coupling were chosen for the main mode. It was assumed that higher acoustic modes have a lower coupling and a lower quality factor. An attenuation factor was defined which was raised to the power of the mode number and multiplied to the initial value of the coupling and the Q-factor respectively. The coupling thereby principally determines the width of the peak whereas the quality factor provides a measure for the peak steepness.

---

[4] Impedance magnitude is shown here instead of the impedance phase because the lateral modes can be seen more clearly there.
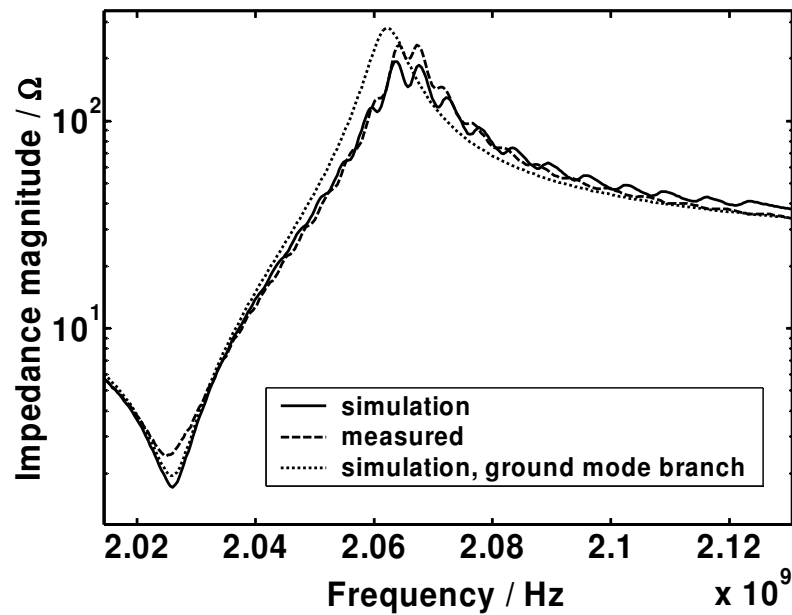
	Q-factor	Coupling
Main mode	340	21 %
First lateral mode	1000	1.5 %
"Attenuation" factor	0.985	0.98

Figure 3.16: Resonator with a diameter of 150 μm and circular shape: measurement and fit with multiple BVD model. Coupling of the first lateral mode is determined to 1.5 % in contrast to 21 % for the main longitudinal mode. The quality factor on the other hand is 340 for the main mode and 1000 for the first lateral mode. For the following modes Q and k_t are determined by subsequent scaling with the attenuation factor. The quality factor for the lateral overmodes is slightly decreasing but still close to 600 for the 40th overmode!

The simulation approximates the measured resonance quite well. So the main mode (purely longitudinal) and the overmodes (a superposition of a longitudinal and lateral mode as discussed above)

seem to be working rather independently. In consequence, the equivalent circuit parameters can be extracted for each single mode and thus the electromechanical coupling and quality factor can be extracted separately. Also shown is the resonance obtained when only applying the ground mode branch of the BVD model. It can be understood as the resonance characteristic of the resonator assuming that it had no lateral resonances.

Table 3.1: Quality factors and couplings of the lateral resonances for a resonator with a diameter of 35 μm and a circular shape (see also figure 3.17).

Mode	Main mode	1	2	3	4	5	6	7	8	9	10	11	12
Q	900	1600	800	750	580	450	410	450	280	230	200	387	349
k_t	0.11	0.024	0.035	0.042	0.032	0.018	0.026	0.02	0.02	0.02	0.02	0.02	0.02

It is observed that the lateral modes, although quite closely spaced in the region of the series resonance, do not explain the reduction of the series quality factor. In fact, Q at the series resonance is slightly higher as compared to the simulation of the pure ground resonance (seen from the sharpness of the dip). Nevertheless, lateral modes indeed lead to a reduction of the parallel Q. The modelling parameters are shown in the table in figure 3.16. With this fitting method a Q factor of 340 for the main (longitudinal) mode is obtained. When the resonance is fitted with the simple BVD model without any branches for the lateral modes, the Q factor reduces to 250. So the Q factor that is actually seen is reduced from 340 to 250 by the lateral resonances.

As expected, the lateral resonances couple much weaker. The coupling coefficient was fitted to 1.5 % thus more than one order of magnitude smaller than for the main mode. This also seems to be the main reason, why they only cause small ripples. The Q factors on the other hand are quite high (1000 for the first mode) and decrease only a little with a Q-factor of still 600 for the 40th overmode.
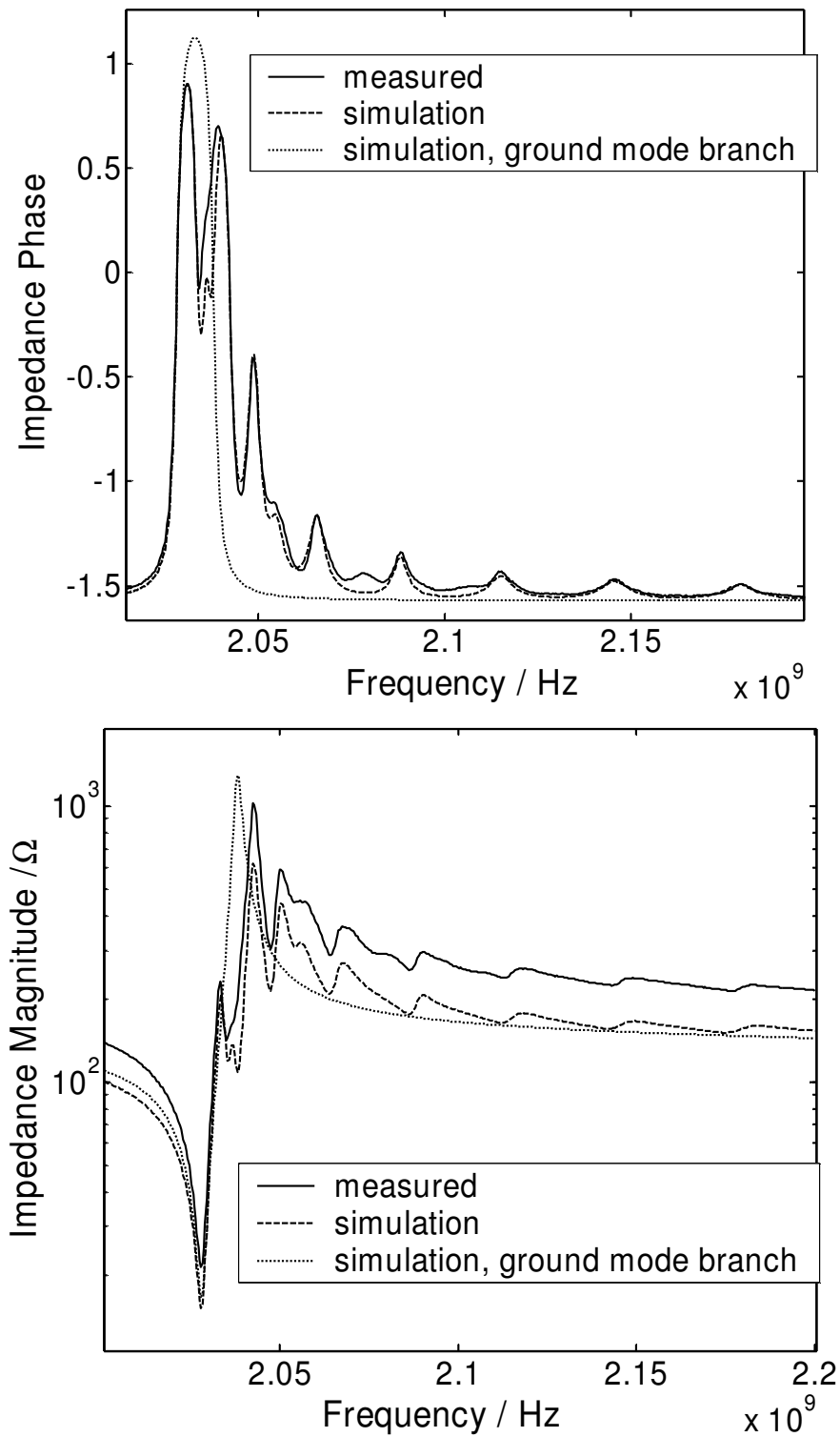
Figure 3.17: Lateral resonances of a circular resonator with a diameter of 35 μm: Measurement (line), fit with a multiple BVD-model (dashed) and the resonance as it would be without any lateral resonances.

The same procedure was carried out with a smaller resonator. In figure 3.17 the impedance characteristic for a resonator with a circular lateral shape and a diameter of 35 μm is shown. The resonances are not only more strongly pronounced but also more irregular than in the case of the 150 μm-resonator. Therefore each resonance was fitted separately by adapting the coupling and the quality factor of the resonance respectively. The values for the quality factor and the couplings are summarized in table 3.2. Also here the first lateral resonances have a higher Q-factor than the main resonance. The quality factor is about 1600 for the first lateral resonance compared to 900 for the main resonance. The other lateral resonances show some variation in coupling, the highest coupling is achieved at the third overtone resonance and also the quality factors do not decline continuously. Also in this case the decline of both quality factor and coupling coefficient are quite low.

Both resonator sizes yield a quality factor of the lateral modes that is higher than for the main mode (at least for the first mode). This ratio is better for the larger resonator (1000 to 340 compared to 1600 to 900). This may be because of the roughness at the resonator edges which will have a higher negative impact for smaller resonator areas.

Furthermore, it is interesting that the fitted quality factors for the longitudinal resonance (main resonance) still differ quite strongly between the 150 and the 35 μm-Resonator (900 to 340). These values are supposed to be the intrinsic values for the Q-factors of the longitudinal resonance. This means that the difference between the series quality factors seen for different lateral sizes can not be only explained with the influence of the lateral resonances. So there has to be another influence apart from the mode structure. This will be analyzed in chapter 4.

4.   Sensor Performance

In this chapter some important aspects of the sensor performance will be addressed. The focus will be on the operation of the device as a mass sensor. As mentioned before the device is well known from filter applications [VAL90]. In that field operation frequency, insertion loss and bandwidth are the relevant properties. Optimization thereby concentrates on increasing the bandwidth and decreasing insertion loss. The operation frequency is defined by the application. Parameters that can be used to improve their performance are for instance the form of the resonator, the lateral dimension and the material composition [RUB05], [LAK92], [LAN03], [LAR02]. Insertion loss influences quality factor and the possible mass resolution of the device, so it is one parameter that has to be optimized also for a mass sensor. Bandwidth on the other hand is less relevant. Moreover, the operation frequency itself is not important but the relative frequency shift, from which the mass attachment can be deduced. So the operation frequency can be essentially treated as a free parameter. Therefore, the influence of this parameter on the device performance will be investigated in section 4.3.

In figure 4.1, an overview of the important influences determining the performance of the device is given. When operating as a mass sensor, the minimum mass, that can be detected, has to be made as small as possible. It depends mainly on three factors: the sensitivity, giving the frequency response of the sensor due to a change in mass, the Q-factor as a measure of the device losses, and the noise describing random fluctuations of certain sensor properties. The relation between these magnitudes will be derived in section 4.1. Sensitivity for a one layered mass sensor is given by the Sauerbrey formula but it can be increased above this value with a clever dimensioning of the layer stack for the sensor. This has been shown in chapter 3.1. So there is some room for optimization. In this chapter, the one dimensional Mason model will be verified by experiments and a reduction of sensitivity with electrode thickness will be observed (section 4.3).

The two factors noise and Q-factor are principally different quantities. The Q-factor describes the relative loss of energy. This can happen in many different ways, the energy can be lost electrically in the signal lines, dielectrically as friction loss during the switching of dipoles or acoustically. A method to experimentally determine the contributions of the different losses in a piezoelectric was presented by Uchino et al. [UCH01]. Electric losses will be treated in section 4.2. Acoustic losses can happen in different ways. If for instance lateral modes are excited, some acoustic energy may be propagating away from the resonator in the lateral direction. In the case that the lateral modes are trapped, they can be characterized electrically. This has been done in chapter 3.2 and the coupling for the lateral modes was determined for different lateral overmodes and resonator sizes. Employing

laser probing techniques, the shape of lateral modes can be investigated more in detail [TIK98] and even material parameters may be extracted [MAK04]. Acoustic losses may as well happen in the longitudinal propagation of the waves. This can be due to acoustic scattering at lattice imperfections or at rough interfaces. Also, a badly reflecting mirror can cause losses. Due to optimization of the mirror and because of the broad reflection band this loss source could be made negligible. Moreover, acoustic loss can happen due to a thickness variation of the acoustic layers. As the layers used for the resonators are only in the range of some hundred nanometers thick, this is an important loss source. The frequency variation that is caused by this thickness variation and the consequent degradation of the quality factor will be determined in section 4.3.
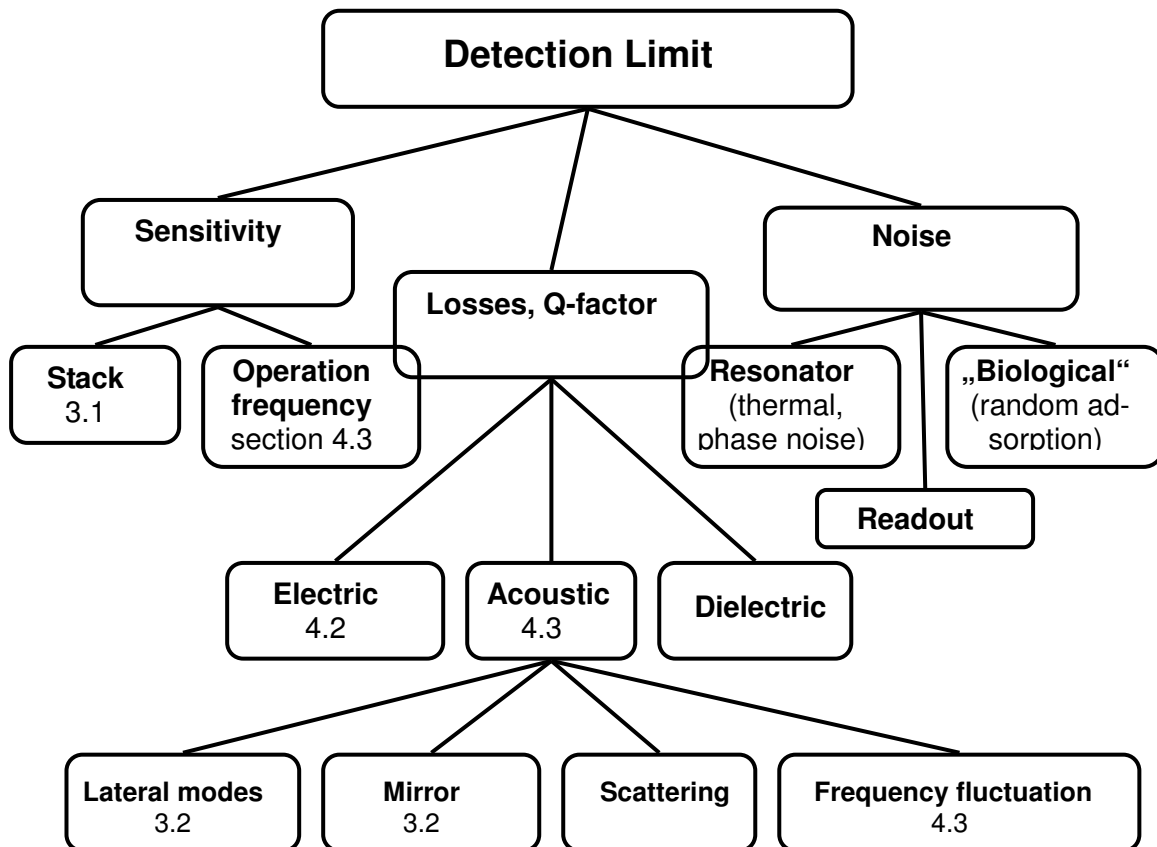

Figure 4.1: Overview of the influences determining the performance of the sensor system.

Noise describes any property in the system, that is subject to a fluctuation in time and that is having an impact on the measurand. This fluctuation together with the Q-factor defines the exactness with

which the measurand can be determined (see equation 4.2). Hence, in theory Q-factor and noise are independent properties, nevertheless, in practice there may be some interrelation between these magnitudes. A loss source may itself be subject to some fluctuation, such as an acoustic scattering due to thermal phonons for instance.

4.1 Detection Limit

Sensitivity will be taken as a starting point in order to determine the detection limit. Sensitivity gives the frequency shift Δf that is evoked by a certain mass attachment per area $\Delta m/A$ on the sensor surface:

$$s = \frac{\Delta f}{\Delta m / A}$$

eq. 4.1.

Here, the mass per unit area or mass loading is used, because in most of the measurement situations the analyte to be measured forms a homogeneous thin film on the resonator surface. In order to know the minimum detectable mass, one must know which frequency shift Δf_{min} can still be detected. From the definition of the resonator quality factor [LAK93] it follows that:

$$\Delta f_{min} = \frac{1}{2} f_0 \frac{\Delta \Phi_{min}}{Q}$$

eq. 4.2

so from equations 4.1 and 4.2 it follows for the minimum detectable mass attachment:

$$\frac{\Delta m_{min}}{A} = \frac{1}{2} f_0 \frac{\Delta \Phi_{min}}{s \cdot Q}$$

eq. 4.3.

In the following, the noise is described within $\Delta \Phi_{min}$, denoting the minimum phase resolution. It will not be determined in this work, because it depends on the application and the readout circuit ap-

plied. Therefore, in the investigations of the device performance the focus will be on the investigation of the 1/s·Q-part of equation 4.3. A figure of merit

$$FOM = s \cdot Q$$ eq. 4.4

will thus be used.

Apart from the noise sources mentioned above, the phase resolution also depends on the respective readout circuit and on the desired signal to noise ratio. Factors like the number of measurements and the measurement time period also have to be taken into account. A larger number of measurements for example will reduce the requirements for the signal-to-noise ratio. The signal-to-noise ratio is usually calculated from the experiments by determining the Allan deviation:

$$\sigma_{allan} = \sqrt{\left\langle (\partial x_2 - \partial x_1)^2 \right\rangle}$$ eq. 4.5,

where x_1 and x_2 are two successive values of a continuous measurement respectively. The signal-to-noise ratio is then determined to:

$$SNR = \frac{X_2 - X_1}{\sigma_{allan}}$$ eq. 4.6.

With a SNR of $\sqrt{2}$ times the Allan deviation, the probability of a signal to be noise would be 32%. Taking $SNR = 3\sqrt{2}\sigma_{allan}$, this probability reduces to 1%. So the desired signal-to-noise ratio depends on the number of measurements. A larger number of measurements will reduce these requirements, because the overall failure probability reduces with the number of measurements. A longer time period on the other hand can introduce other noise sources such as those coming from fluctuations in the environment (random mass attachment for example).

4.2 Electrical Losses

Signal lines

Electrical losses occur due to the wiring that is necessary to connect the resonator. The propagation of an electric wave at high frequencies is mainly taking place in the dielectric medium surrounding the electric conductor. To investigate the influence of electric losses, resonators with different wiring lengths were examined. As the acoustic resonator forms part of an electroacoustic transducer, it shows the well-known behaviour with two resonances, a short circuit and an open circuit resonance. This can be modelled with the Butterworth-van-Dyke equivalent circuit [ROS88]. According to this model, the quality factor can be written as (see chapter 2.2):

$$Q = \frac{\omega_R L_m}{R_m} \qquad\qquad \text{eq. 4.7.}$$

Because of the transducer being part of a resonator circuit a quality factor is defined for the serial as well as the parallel resonance, of whom the latter mainly reflects acoustic losses, whereas the former is also influenced by electrical losses. According to Larson et al. [LAR00], the quality factor of the series resonance and the parallel resonance are related to each other via the series resistance:

$$Q_s = Q_p \frac{1}{1 + \dfrac{R_s}{R_m}} \qquad\qquad \text{eq. 4.8.}$$

As shown in chapter 2.3 (table 2.1 b), the motional resistance depends on the area of the resonator. Hence, the motional resistance can be expressed as the product of a specific resistance of the resonator (depending on resonance frequency, material parameters and coupling) and the resonator area:

$$R_m = \frac{R_{spec}}{A} \qquad \qquad \text{eq. 4.9,}$$

which means that for small resonator areas R_m is increasing and Q_s should be approaching Q_p according to equation 4.8. For large resonator areas on the other hand the resistance of the signal lines is expected to have a stronger influence. By fitting 14 different resonators with 8 sizes between (50 $\mu m)^2$ and (200 $\mu m)^2$, all of them operating at 2 GHz, a value for R_{spec} between $2.5 \cdot 10^{-8}$ and $4.4 \cdot 10^{-8}$ Ω/m^2 was found.
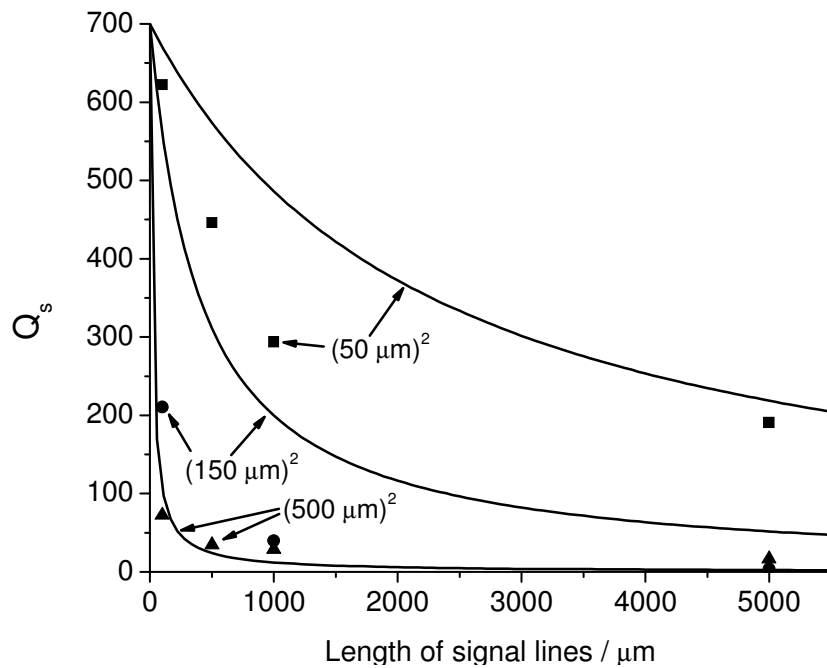

Figure 4.2: Mutual influence of the signal line lengths and resonator diameter on the resonator performance: according to equation 4.8, the impact is stronger for smaller resonators areas because their motional resistance R_m is smaller, scaling directly with resonator area. The dots represent measurements, lines are calculated with R_m taken from fitted values and R_s from the signal line geometry (an Ohmic resistance with the specific resistance of gold is assumed). Q_p is assumed to be 700.

Using the fitted values of R_m, an estimation of the mutual influence of R_m and R_s on the series quality factor can be obtained (according to equation 4.8). The fitted values of the motional resistance range from 0.078 Ω for a (500 $\mu m)^2$ resonator to about 10 Ω for a resonator with an area of (50

$\mu m)^2$. A signal line having a thickness of typically 200 nm, a width of 25 μm and a length of 100 μm the Ohmic resistance would be about 0.44 Ω. In figure 4.2, the theoretical values obtained from equation 4.8 are shown. A Q_p of 700 was assumed and R_s was determined as the Ohmic resistance of the signal line according to

$$R = \rho_{spec} \frac{l}{hw}$$ eq. 4.10

with ρ_{spec} the specific resistance of gold, l the signal line length and h and w are the thickness and width. Especially for large resonator areas, Q_s is strongly reduced by the Ohmic resistance. Hence, for greater resonator areas much care must be taken to reduce the Ohmic resistance by either making the signal lines shorter or increasing their cross section. The calculations are at least qualitatively mirrored by the measured values (dots). Yet, some of the measured values show a strong deviation from the theoretical ones, which may be due to a resistance effect of the resonator itself and will be discussed in the next section.

Resonator area

The influence of the resonator area on the quality factor will now be investigated. Most of the resonators investigated have a quadratic shape and are edge fed. As the electrode thickness is always the same, the Ohmic resistance is the same for all resonator top electrodes ($l = w$ in equation 4.10). Hence, there is no change expected because of the Ohmic resistance of the electrode. Nevertheless, it has to be taken into account, that the resonator itself has a complex impedance depending on the resonator area and the frequency. Together with the series resistance this will have an impact on the resonator performance. Figure 4.3 (upper graph) illustrates this. It shows the magnitude of the electrical impedance for two resonators with a lateral dimension of $(50\mu m)^2$ and $(500\mu m)^2$. They were obtained from calculations with the BVD-model. Model parameters that are typical for the investigated device were used and were directly scaled with resonator area (according to the equations in table 2.1). Because of the reciprocal dependence of impedance on capacitance, the impedance curve of the smaller resonator lies two orders of magnitude below the larger resonator. At series resonance, the circuit is principally shortened with only the series resistance remaining. Series resistance therefore represents a lower limit of the impedance at series resonance. At 2.05 GHz, the absolute

value of the capacitance impedance is $\left|\dfrac{1}{j\omega C_0}\right| = 1.61\Omega$ which is already in the range of the series
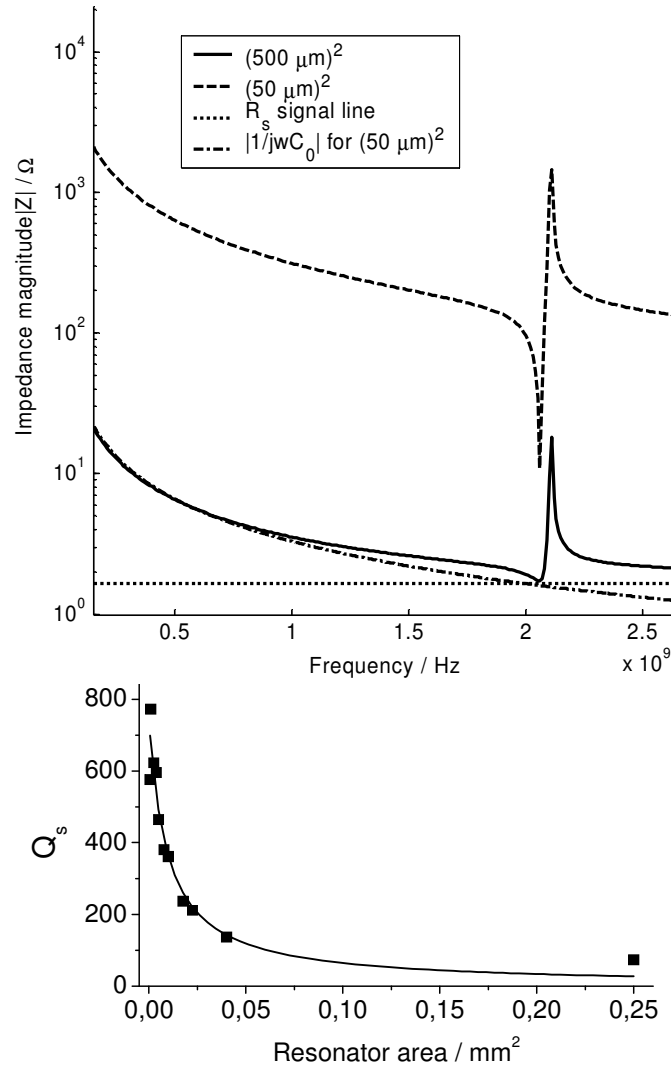
resistance.

Figure 4.3: Top: Impedance characteristic (impedance magnitude) for two resonators with different areas determined with the BVD-model. The impedance of the resonator having a diameter of 500 μm is getting quite close to the series resistance (1.6 Ω) which leads to a significant reduction in the series quality factor compared to the 50 μm resonator. Lower panel: Q_s obtained for different resonator areas for a signal line length of 100 μm (200 nm thick, 50 μm wide). It displays an approximately reciprocal dependence of $Q_s \approx \dfrac{746}{1+106\cdot A[mm^2]}$.

Therefore, the series resonance will be less sharp for the larger resonator and the quality factor will downgrade accordingly. Apart from resonator area, this influence also becomes more critical with increasing operation frequency

In figure 4.3 (lower graph), the series quality factors are shown for different resonator areas, and an approximate reciprocal dependence is obtained. . Fitting Q_s over the resonator area yields $Q_s \approx \dfrac{746}{1+106 \cdot A[mm^2]}$. So again, the dependence from equation 4.7 is obtained. Q_p can be identified to 746 and the specific motional resistance from equation 4.8 can be determined to $1.5 \cdot 10^{-8}$ Ω/m^2. Hence, when an operation at series resonance frequency is desired, resistance scaling has to be considered very carefully, taking into account the interplay of resonator impedance and the resistance of the signal lines.

Also, the top electrode itself can have a resistance effect. This was tested with a resonator with a rectangular shape. It had a large aspect ratio, with a length of 200 μm and a width of only 25μm. In a first measurement it was contacted at the narrow edge and for another measurement the contact was in the center of the resonator. In the first case, a lower series quality factor was obtained because of the electrical distance being twice as long. Nevertheless, for the quadratic resonators used here, the Ohmic resistance of the top electrodes is only about 0.05 Ω compared to 1.6 Ω for the shortest signal lines.

4.3 Acoustic Performance

Experiment

In this section, the influence of acoustic losses and especially the impact of operation frequency on the device performance will be investigated. Resonators with operation frequencies of 2.2, 4.1 and 8.0 GHz were fabricated. The resonators were of a simple type with only the top electrode being patterned. This is shown in figure 4.4. The structure was obtained by simply etching a trench into the top layer separating the electrode from the large area outside which is contacted capacitively with the ground electrode. This setup allows for easy fabrication of an FBAR employing only a single photolithographic step. The materials used were platinum as top and bottom electrode and ZnO as the piezoelectric material. The acoustic mirror also consisted of alternating layers of ZnO and platinum. The thicknesses used for the 2.2 GHz stack were: 100 nm for the top electrode, 400 nm the piezolayer, 500 nm for the Pt ground electrode and the Pt mirror layers, respectively, and

800 nm for the ZnO mirror layers. In order to get to higher frequencies, the layers were downscaled and two different stacks were fabricated with a thickness of 50 or 27 nm for the top electrode, 250 or 130 for the piezolayer and 220 or 110 for the Pt ground electrode. The mirror layers had a thickness of 380 or 190 for ZnO and 270 or 130 nm for Pt.

In order to determine the sensitivity of the sensor, the top electrode thickness was varied and the resulting resonance frequency shift was determined. The thickness variation was achieved by a plasma sputter etch of the platinum signal electrode. Before the first sputtering step, the thickness of the signal electrode was determined by α-step measurements (Tencor α-step 200) quantifying the height of the step that is being formed by the top electrode. Additionally, a four point measurement of the electrical resistivity was carried out. After each sputtering step, the thickness of the top electrode was quantified by measuring the resistivity. The measurement tips were kept in the same position throughout the whole measurement.
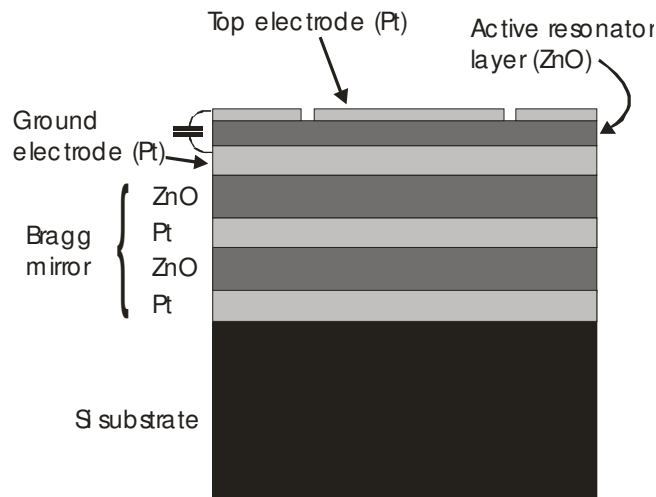

Figure 4.4: Configuration of the FBAR used for the measurements

Sensitivity

The sensitivities were determined theoretically from the Sauerbrey formula (equation 2.32). Therefore, the resonator was assumed to be made up of a single ZnO-layer. The resulting values for the sensitivity are 2.24 kHz·cm²/ng for 2.2 GHz, 8.96 kHz·cm²/ng for 4.1 GHz and 35.85 kHz·cm²/ng for the 8 GHz case.

Furthermore, the sensor sensitivity was determined from the one dimensional model (Mason model, see chapter 2.3). The acoustic properties of the whole stack including the top electrode and the piezoelectric resonator layer were inserted and the sensitivity was evaluated from the derivative of frequency over top layer thickness, just as described in chapter 3. The sensitivity could thereby be calculated to 2.098 kHz·cm²/ng for the 2 GHz stack, 8.512 kHz·cm²/ng for 4 GHz and 27.7 kHz·cm²/ng for 8 GHz. The results are summarized in table 4.1.

According to the Sauerbrey equation, the sensitivity exhibits a quadratic dependence on the sensor operation frequency. It can nevertheless be seen that the simulated results lie slightly below the values for the single layer model with the disagreement increasing for increasing sensitivity. In consequence, this means that less than a quadratic improvement is achieved when increasing the operation frequency of the device. The reason for this has to be searched in the multilayer properties of the resonator. There are some layers such as the adhesion layers needed to compensate for lattice mismatches between the different mirror layers, which were not downscaled. The thicknesses of these layers are in the range of 10 nm, which is no longer negligible for an 8 GHz device, where mirror and transducer layers are around 100 nm thick.

Table 4.1: Comparison of sensitivities: calculated from a simple one layer model (Sauerbrey), from 1D-simulations and measurement. Sensitivities given in kHz·cm²/ng.

Operation frequency	2.2 GHz	4.1 GHz	8 GHz
Sauerbrey	2.24	8.96	35.85
1D-simulation	2.098	8.512	27.7
Measurement	2.030	8.250	26.2

The experimentally obtained sensitivities agree quite well with the values from simulation as the results show (table 4.1). Deviations can be explained by a certain inaccuracy of the applied method of thickness determination. So the one dimensional Mason model proves to be to be very well suitable not only to determine the operation frequency but also the mass sensitivity of the device.

Acoustic influence of the top electrode thickness

In section 4.2, the influence of series resistance has been investigated. This parameter depends on the geometry of the signal lines and the top electrode. In particular, series resistance will increase with decreasing electrode thickness. As the electrodes additionally form a part of the acoustic path of the resonator, the influence of the thickness on the acoustic properties and especially the sensitivity of the device will be investigated in the following. It will be shown that this thickness is indeed a critical quantity.
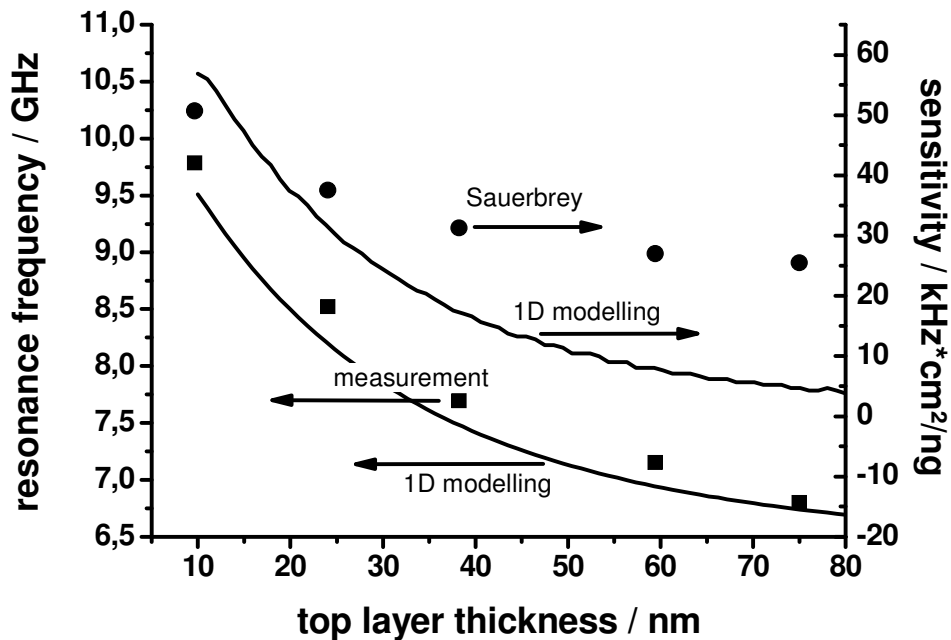

Figure 4.5: Resonance frequency for different top layer thicknesses (8 GHz device). Because of multilayer properties the resonance frequency (squares: measured, straight line: simulation) behaves strongly non linear. The sensitivity corresponding to these modelled values (upper straight line) is considerably lower than expected from the Sauerbrey calculation (circles) at the respective frequency.

An acoustic stack operating at 8 GHz is considered. In calculations with the Mason model, the thickness of the top layer was varied between 10 and 80 nm. The resonance frequency was determined and again the sensitivity calculated using equation 2.32 ($\Delta m/A$ being directly calculated from

the toplayer thickness). Again, the outcome of these simulations was confirmed by corresponding measurements with the method described above.

The results are plotted in figure 4.5 where the lower line and the squares show the resonance frequency obtained from the simulation and the measurement, respectively. The upper line shows the sensitivity obtained from the derivative of simulated frequency over top layer thickness, according to equation 4.1. The measured values are modelled quite accurately by the Mason model (therefore the measured values for the sensitivity are not shown in figure 4.5). The sensitivity is varying over a range from 4 to 56 kHz·cm²/ng. So again, a multilayer effect is observed analogue to the calculations in chapter 3, but this time it is decreasing the sensitivity below the Sauerbrey values. Two factors contribute to this decrease: As the resonator layer is only 130 nm thick a reduction of 70 nm of the top electrode thickness strongly affects the resonance frequency. As the squares in figure 4.5 show, it is varying from about 6.6 to 9.5 GHz. Therefore, an increase in sensitivity according to the Sauerbrey model is expected. To assess this influence, the simulated values of the resonance frequency were inserted into the Sauerbrey equation and the obtained sensitivity was also plotted (circles in figure 4.5). With a range of 24.4 to 50.6 kHz·cm²/ng the sensitivity shows a much smaller variation than the "real" sensitivities. Only for small toplayer thicknesses this "Sauerbrey-Sensitivity" matches the simulated value.

Frequency fluctuation

The Quality Factor of the resonator is a measure for the energy loss in the system. These losses were classified at the beginning of this chapter. In this section, the losses occurring due to interface roughness will be determined, because this is an important parameter determined by the fabrication process and having an influence when the thicknesses of the layers are scaled.

It is assumed that surface roughness is locally altering the length of the acoustic path t. This will cause a frequency fluctuation with the consequence of a broadening of the acoustic resonance. With this model a simple estimate for a resonator consisting of only one layer (see figure 4.6) can be made. The length variation Δt causing a certain Q can be calculated. One can assume a standardized normal distribution for the thickness fluctuation which translates into an analogous frequency fluctuation. The quality factor is then obtained from the full width at half maximum of the acoustic amplitude Δf and the resonance frequency as $Q = f_0 / \Delta f$. If surface roughness is assumed to be about the same for all layer thicknesses (Δt = const.) the frequency dependence of the quality factor can be estimated. Because of $f = v_a / 2t$ (v_a the acoustic velocity) and $\Delta f / f = \Delta t / t$, the quality factor can be obtained:

$$Q = \frac{t}{\Delta t} \propto \frac{1}{f}$$ eq. 4.11.

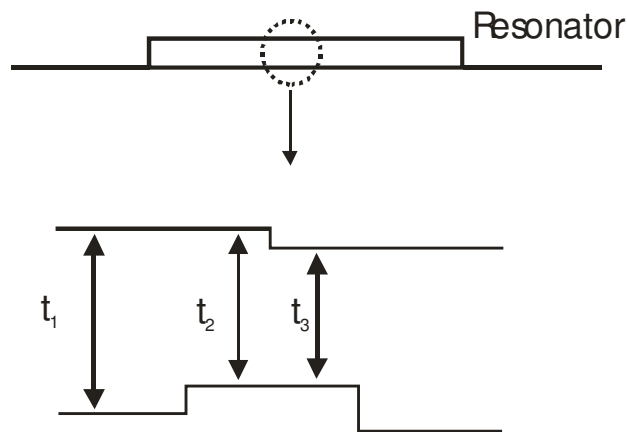So the quality factor is inversely proportional to resonance frequency.

Figure 4.6: Microscopic view of the resonator. Interface roughness causes a local variation of the acoustic path t, the resonance broadens leading to a reduction of the quality factor (derivation see text).

A multilayered resonator with a frequency of 2 GHz corresponds to a single layered resonator consisting of a 700 nm thick ZnO-film. It has a typical Q of 400. With equation 4.11, a thickness fluctuation of $\Delta t = 1.8$ nm is obtained. α-step and AFM measurements of the resonator layer yield surface roughnesses of a few nanometers which does not contradict this estimation and it seems plausible that frequency fluctuation is one important source of resonance broadening.

Comparison for different frequencies

The resonators operating at 2, 4 and 8 GHz were characterized electrically by reading out the S11-parameters with the network analyzer and determining the impedance characteristics. The quality factor was taken from the slope of the impedance phase. For each frequency, a whole wafer with a multilayer stack was processed. For each diameter and each frequency, the quality factor of 6 resonators was determined, and the average value was calculated. The standard deviation of the quality

factors for a certain diameter was found to lie between 4 and 30 % and was especially large for small resonator sizes, which can be assigned to the stronger lateral modes (see chapter 3.2). The evaluated quality factors also showed a strong dependence on diameter with a maximum at a certain value (see also section 4.4). In order to compare different frequencies, the respective resonator diameter with maximum quality factor was used for the calculations.

Table 4.2: Q-factors and figures of merit for different frequencies.

	2.2 GHz	4.1 GHz	8 GHz
Q_s	480	191	100
Q_p	399	179	74
FOM = $Q_s \cdot s$	1007	1626	2105
FOM = $Q_p \cdot s$	837	1524	2050

The results are summarized in table 4.2. The quality factors strongly decrease with frequency, roughly following a reciprocal proportionality. This behavior could be caused by frequency fluctuation as discussed before.

Several additional factors play a role and make an interpretation of the results difficult. In the next section the specific structure of the resonator will be considered.

4.4 Lateral Structure

As described earlier, the resonators in this study were processed such that only the top electrode was patterned. A simple illustration of the sensor is shown in figure 4.7 a. The top electrode is patterned and prolongated in order to form the contact pad. The latter is needed to enable contacting with the Picoprobe® RF-tips and has an extent of 80 µm in both directions. For resonators with diameters below 100 µm this contact pad is not needed and the resonators have a simple quadratic shape (see figure 4.7 b). In another setup, the resonators are patterned completely which means that the piezoelectric layer is being patterned before the application of the top electrode (see figure 4.7 c). The bottom electrode can therefore be directly contacted whereas in the first design it is contacted ca-

pacitively. Manufacturing of this system is much more laborious and includes several photolitho-
graphic steps. Therefore it was available only for 2 GHz.

The influence of these different resonator designs was investigated. In figure 4.8 the area depend-
ence of the quality factors is compared for the completely patterned and the only top electrode pat-
terned system. For the completely patterned resonator, a decrease of the series resonance quality
factor and an increase of parallel quality factor with resonator area is observed. The decrease of the
series quality factor is reciprocally proportional to the resonator diameter and was explained in sec-
tion 4.2.

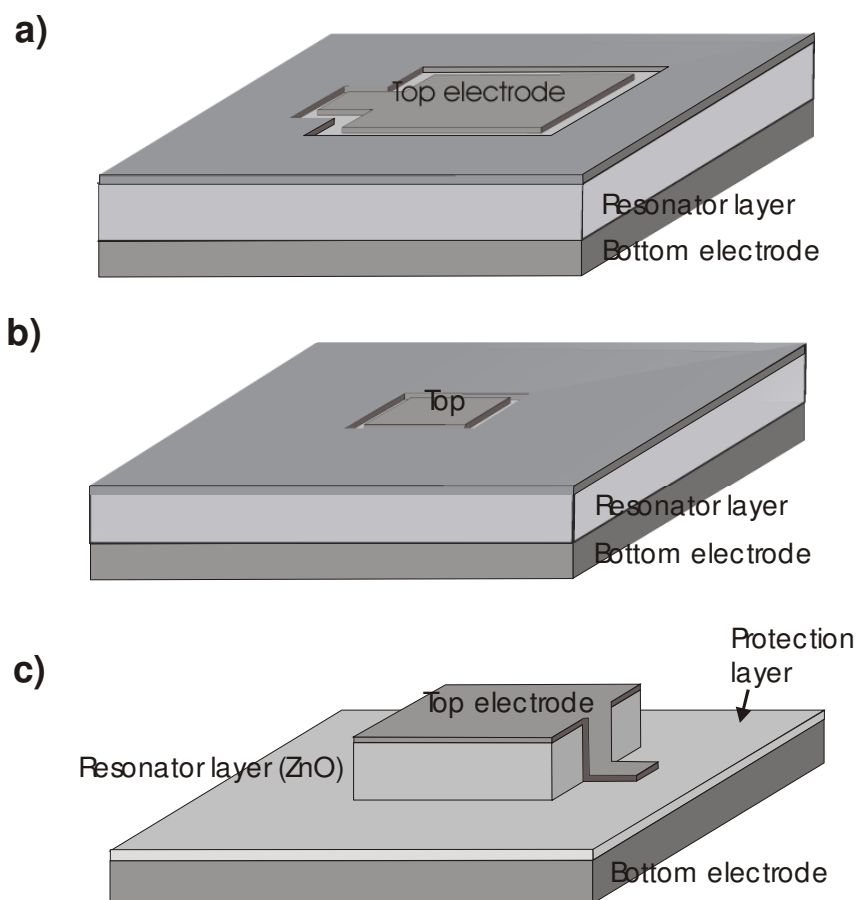*Figure 4.7   a): Design of a resonator with only the top electrode being patterned (for resonator
diameters above 100 µm) and b) for resonator sizes below 100 µm, c) shows a completely patterned
resonator. In the first case, the area below the contact pad forms a resonator of its own.*

For the resonator design with only the top electrode being patterned and for diameters above 100 μm, the series quality factor saturates (with $Q_{s,min} \approx 174$, see figure 4.8, top). On the other hand, the parallel quality factor increases with an increase of the resonator size up to 200 μm (with $Q_{p,max} \approx 400$, see figure 4.8, lower panel). Above this size, it even decreases again.

To explain all this, the different loss mechanisms have to be regarded. As Lakin showed [LAK03] the acoustic losses decrease with increasing aspect ratio. The reason for this are lateral resonances which propagate into the substrate and thus dissipate the acoustic energy. This may be the reason for the lower quality factor of the small area resonator with patterned top electrode: as the resonator edges are in acoustic contact with the area outside, the energy trapping is worse. This leads to an especially high acoustic loss for small resonators. An increase of the aspect ratio on the other hand has a great effect for the reduction of such losses so that the rise is steeper for the only top electrode patterned case.

Why does the system with a patterned top electrode patterned system reach a bottom or top in Q_s and Q_p, respectively? In this resonator setup the area below the contact pad forms a resonator of its own. So the quality factor may additionally be determined by the resonating contact pad.

This supposition is confirmed when the lateral dimension of the contact pad is considered. It is 80 μm corresponding to a resonator with a quality factor a little above the saturation value (see dotted line in figure 4.8). So the overall quality factor is lifted by the higher quality factor of the contact pad. For the parallel resonance the same occurs in the opposite way. Here, the quality factor of the contact pad (dotted line) lies below the resonator quality factor and the overall quality factor for the larger resonators having a contact pad is decreased.

Finally, Q_p is observed to be quite "noisy" for small resonator sizes as being represented from the nonlinearity of the Q values as well as the high standard deviation. This is due to the lateral resonances which make an exact determination of the intrinsic quality factor impossible (see chapter 3.2). Moreover, they may even have a positive influence on the visible series quality factor as was discussed in chapter 3.
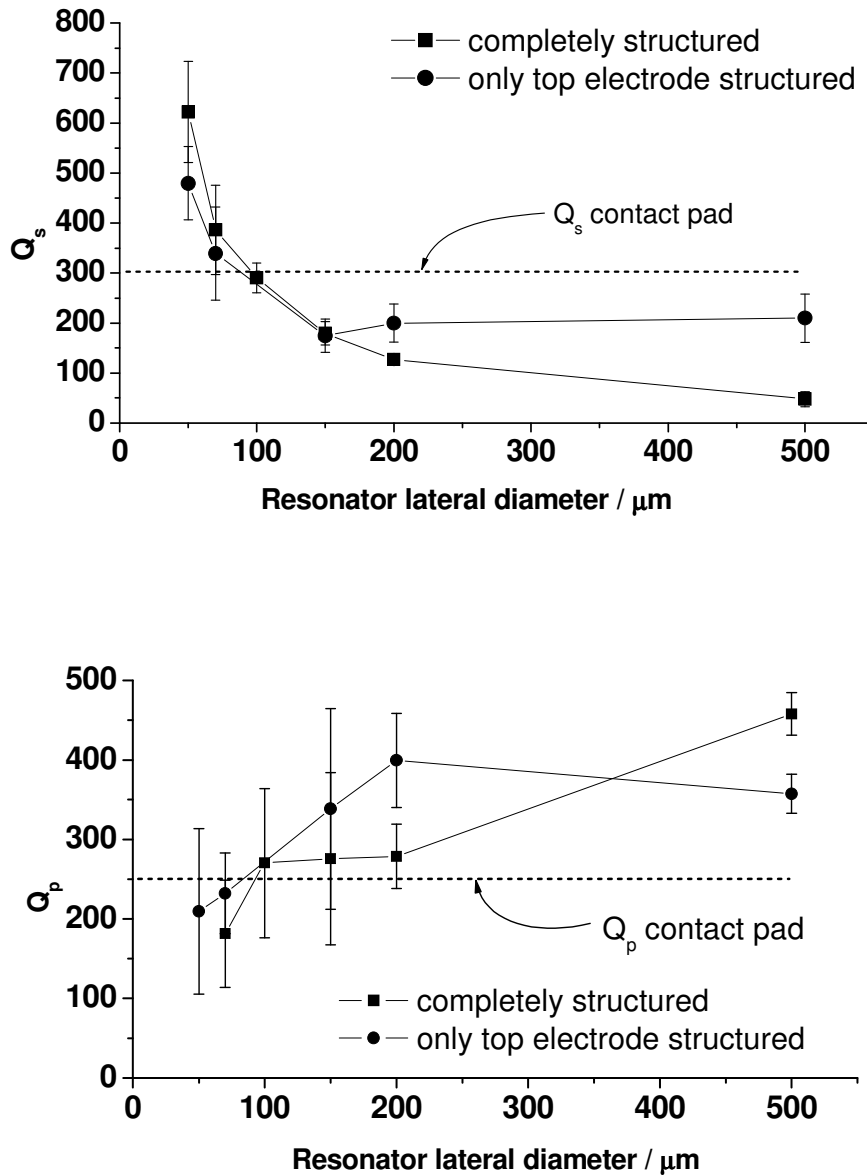
Figure 4.8: Comparison of serial and parallel Q for a top electrode patterned and a completely patterned resonator, both operating at 2 GHz. For the series resonance, Q is decreasing because of the electrical impedance effect (see section 4.2). The quality factor of the only top electrode patterned is reaching a bottom because of the resonating contact pad. Q_p on the other hand is increasing with lateral size and equally shows an upper limit for the only top electrode patterned case. The dotted line shows the approximate Q value of a resonator with a diameter of 80 µm, which corresponds to the size of the contact pad. For each size several resonators were measured and the error bars show the standard deviation.

To summarize, it becomes clear that such a simple system where only the top electrode is patterned is not sufficient to give evidence for precise scaling rules for the frequency dependent adjustment of the resonator area being needed in order to obtain optimum performance. Disturbing influences originating from the acoustic properties of the contact pad falsify the result so strongly, that no conclusion can be drawn according to the resonator dimension being optimum for the respective operation frequency. The variation of Q is rather small as compared to these disturbing effects. In order to obtain reliable results regarding the frequency and area dependent performance, a setup without a resonating contact pad should be chosen.

4.5 Conclusions for the Sensor Design

For application of the FBAR as a mass sensor, it is desired to make the device as small as possible. This does not only reduce manufacturing costs because the packaging density increases, it also enables fabrication of large array comprising many FBARs with different functionalities. The series resonance displays a quality factor that is increasing with about the reciprocal of resonator lateral extent. Consequently, it seems desirable to read out the series resonance frequency thereby exploiting the double advantage of a better performance and a smaller size. The parallel resonance quality factor in turn strongly decreases which has to do with acoustic leaking.

In order to achieve efficient operation in the mass sensor mode it has to be ensured that effects deriving from the series resistance are excluded. This could mean for instance electrically isolating the resonator from the analyte. Moreover, when the resonator is further downscaled, lateral resonances play an increasingly important role and will reach a magnitude where the danger of mode hopping occurs. Thus, an efficient mode extraction has to be developed as discussed in chapter 3.2. This will certainly be one of the main future tasks.

According to equation 4.3, the mass resolution is dependent on the Q·s-product, the frequency and furthermore the phase resolution $\Delta\Phi$. So in order to make conclusions about the actual device performance, further studies will be needed to determine the magnitude of the phase resolution. This phase resolution, however, will depend very much on the respective readout mechanism, which could be a frequency counter when a simple and small device is desired, or an impedance analyzer similar to that used in the experiments here, which in turn allows to record more measurement details.

Furthermore, the minimum detectable mass loading depends on the required signal-to-noise ratio. Factors like the number of measurements and the measurement time period have to be taken into

account. A greater number of measurements for example will reduce the requirements for the signal-to-noise ratio of an actual single measurement. A greater time period on the other hand can introduce other noise sources such as those coming from fluctuations in the environment (random mass loading for example).

If for instance a phase noise following a 1/f-dependence is assumed, the Q·s-product shown in table 4.2 would describe the resonator performance and the mass resolution would improve slightly with frequency. The increase of sensitivity is overcompensating the decrease of the quality factor. A constant phase noise on the other hand would mean that the sensor performance is getting slightly worse with higher frequencies. Sensitivity, however, can be modelled quite precisely as one could see in section 4.3.

Further consequences must be taken into account when higher frequencies are aimed at. There is for instance the problem of the inherent noise of the material which is increasing with frequency, the power consumption of device and electronics, and issues such as the ageing rates [VIG00], which all have to be discussed in the context of the respective application. Ageing rates for instance are less relevant for disposable devices. Moreover, the sensor has to be made temperature stable which is more difficult for higher frequencies.

Finally, the problem of nonlinearity of the frequency shift arises for higher frequencies. This was discussed in section 4.3 and two principal problems arise from this concerning the operation of the FBAR as a mass sensor. The first problem is that this nonlinearity occurs when the top electrode thickness is getting into the order of the thickness of the resonator layer.

So on the one hand the top electrode has to be made very thin in order to achieve a good sensitivity (and to minimize acoustic losses in the relatively "soft" top electrode [SAL02]). On the other hand, decreasing the electrode thickness will increase the series resistance. It is important to note, that the "multilayer" degeneration of sensitivity as being discussed in section 4.3, can be of an order of magnitude or more thus nullifying the "Sauerbrey" increase of sensitivity due to a frequency increase. Measurements of the quality factor taken from the parallel resonance for a resonator with a diameter of 500 µm at different electrode thicknesses indeed show an increase of the quality factor for smaller electrode thickness, meaning an improvement due to lower acoustic loss in the metal electrode.

The second problem caused by nonlinearity is that sensitivity may vary throughout a measurement as typical attachment layers can be several nanometers thick. This means that the results obtained

for the mass loading have to be corrected throughout the measurement and also the resolution will downgrade.

In conclusion, it can be stated that according to the current assessment the Q·s-product for the FBAR is slightly increasing with frequency. Nevertheless, when a precise statement or suggestion has to be made regarding the frequency which should be used, not only the readout mechanism must be considered and especially its measurement accuracy. Also the sensing application and the special demands for the sensor have to be taken into account.

5.   Application as a Stress Sensor

In this chapter, the sensor will be submitted to an external pressure or tension. Pressure sensors based on surface acoustic waves are already in practical use for measuring the pressure in car tires [POH97] and have been proposed as early as 1976 [REE76]. There are quite a number of potential applications for a stress sensor. On the one hand, it may be thought of a monitoring of gas or fluid pressures. Fluidic systems are used for a wide range of chemical processes and they often require the monitoring of the fluid pressure. In medical diagnostics it may be a helpful device to monitor the blood pressure, one of the most important parameters in the human body. An example of how such a sensor could look like is shown in figure 5.1. The same configuration may be employed as a sensor for gas pressure as well.
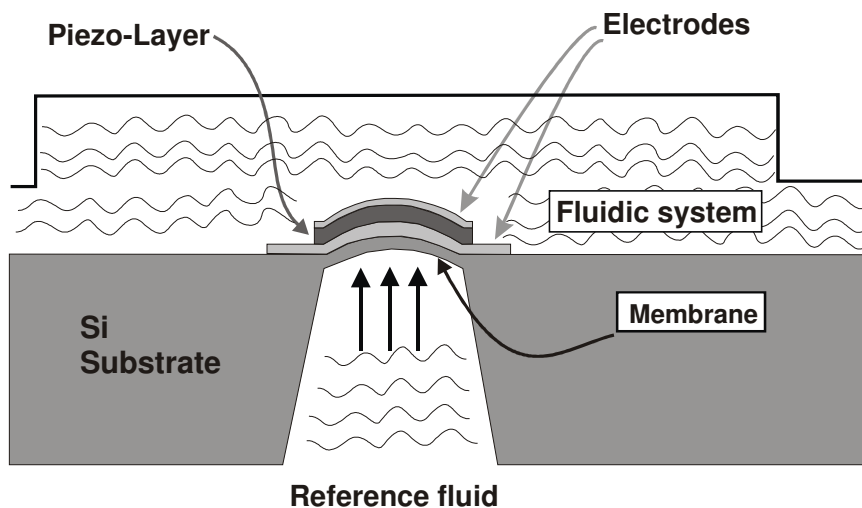

Figure 5.1: FBAR-sensor measuring a fluid pressure. Setup as a membrane. Difference of the pressures of a reference fluid and the measurand fluid causes bending of the membrane and thus a resonance frequency shift.

The configuration consists of a membrane made of silicon and separating two volumes. Depending on the application, also a more stable material could be used. Membranes made of steel for instance are more robust and therefore suited for higher pressures. One volume contains the gas or fluid to be measured whereas the other volume contains a reference gas or fluid having a constant pressure. The difference pressure of the two fluids or gases causes a bending and thus introduces some stress into the membrane. Apart from this function, the membrane also serves as the acoustic cavity. The

measurement principle bases on the fact, that the forces acting perpendicularly on the membrane result in a bending of the membrane. The forces acting inside the plate are mainly in the lateral direction, being caused by the elongation of the membrane which is a result of the clamping to the substrate.

The forces have different effects on the resonator. Through the poisson ratio, the thickness of the membrane is altered. Stretching the membrane certainly changes its mass density, which is directly related to the acoustic velocity. Finally, it seems possible that the elastic properties themselves are altered due to the deformation of the electron orbitals. The magnitude of these effects and their impact on the resonance frequency will be discussed later in this chapter.
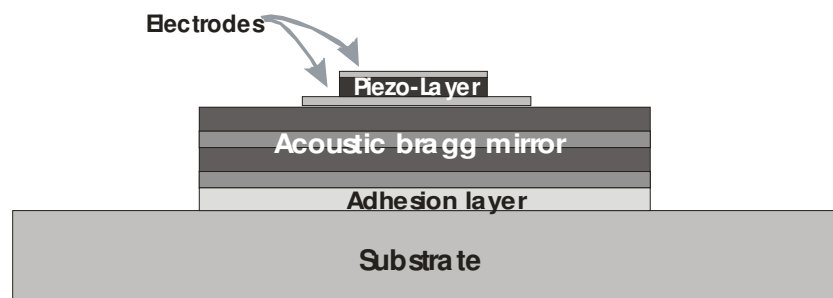

Figure 5.2: Setup for an FBAR sensing material strains: SMR (solidly mounted) configuration with an appropriate adhesive layer transmitting the strain from the substrate to the sensor.

The sensing principle may also be applied in the area of monitoring material strains. A configuration for such a sensor is shown in figure 5.2. In this case the FBAR would be in the solidly mounted to the substrate under investigation, with a bragg mirror reflecting the acoustic wave. Hence, the acoustic energy is confined in the sensor top layer. This energy confinement is necessary, because otherwise the sensing effect would cancel out. A substrate, that is bending due to an externally induced pressure, has opposite strains on top and bottom. It will be shown later, that also the resulting frequency shifts are opposite.

As the sensor thickness is only some 100 nm, which is thin compared to most substrates, the forces exerted by the sensor to the substrate can be neglected. In consequence, measuring the strain with an FBAR will be intrusion free. The influence of the sensor properties on the measurement result will be almost negligible. A critical point, however, will be to choose an appropriate material for the adhesion layer and an adequate process to fix the sensor to the substrate. This adhesion layer has to

ensure that the material strain is efficiently transmitted to the sensor. With the afore mentioned approximation that the sensor has no effect on the substrate, and under the assumption that the adhesion layer is working optimally, the sensor will adopt the deflection at the substrate surface. As a consequence the sensor is in fact measuring the strain on the substrate surface.

5.1 Experiment

To evaluate the FBAR device and test its functionality as a stress sensor, a measurement setup was required, which mirrors the situation in a sensing application as properly as possible. It was made use of the fact that the sensor was available on a wafer. A wafer can be bent quite easily by the application of lateral forces. One problem measuring an FBAR directly on a wafer consisted in the electrical contact. Removing the measurement tip and contacting it again introduces some considerable noise, which may amount up to 100 kHz. Hence, a measurement method had to be found with the sensor remaining contacted throughout the measurement. Furthermore, it had to be ensured, that the contact pressure does not change as a result of the wafer bending.

Therefore, a measurement configuration as shown in figure 5.3 was chosen. The wafer was positioned on a steel point. The steel point had a diameter of about 700 μm at the top. The sensor was aligned with the steel point. This was achieved by first aligning the steel point with the measurement tip. After that the wafer was positioned on the steel point. While steel point and measurement tip remained in place, the wafer was moved into the right position in order to be contacted. Now, a ring was placed on the top side of the wafer around the edge. The 4'' adapter ring from the Ardenne[®] sputtering system was used. It could be moved in vertical direction with the help of three micrometer screws being aligned to the same height. In this manner, the sensor was the fixed point of the whole setup and there could be no movement of the sensor in lateral or vertical direction.

To allow the thermal coupling of the sensor to the chuck, some water was positioned around the steel tip, wetting the wafer as well as the supporting construction below. Several tests were carried out in order to rule out possible side effects. The temperature coupling was tested by altering the chuck temperature and reading out the sensor response. Furthermore, the influence of the Picoprobe contact pressure and position was tested. All these influences could be made negligible compared to the measurement effect.

In an additional experiment the curvature of the wafer was measured. First, a baseline measurement was taken of the unbent wafer and then the wafer was bent with a deflection of 8 mm at the wafer edges. The deflection was measured with the help of the RF tip. The RF tip was supported to an

XYZ-table and thus it was possible to measure the distance from the center with the X- and Y-screw and the deflection with the Z-screw.
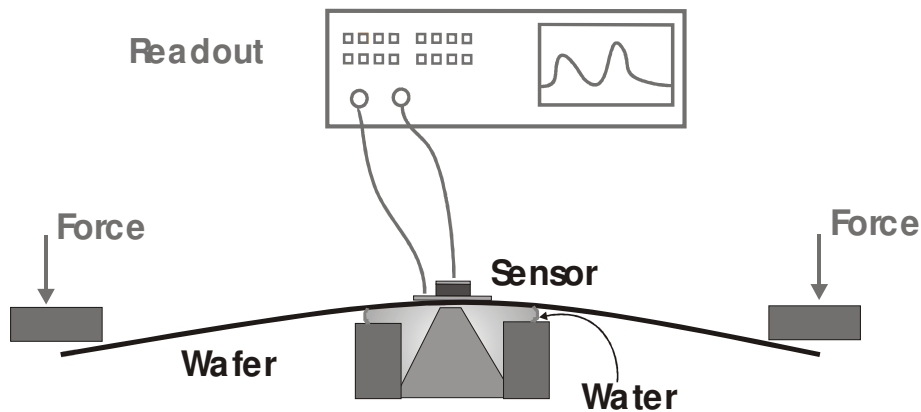

Figure 5.3: Experimental procedure: wafer with sensor positioned on a steel point. Applying a force on a ring around the edge of the wafer. Readout is done with the help of a network analyzer.

The two sensing configurations, that have been discussed in the beginning, are reproduced quite realistically. The wafer bending results in a force in both x- and y-direction whereas a secondary effect perpendicular to the sensor surface will occur as well. The experiments were all carried out with a completely patterned resonator. Furthermore, resonators with were tested with different diameters ranging from 50 up to 200 μm. No difference of the measured frequency shift was found for these different sizes. If there were some kind of relaxation of the strain within the resonator it would be expected to be different for different resonator sizes. This does therefore not seem to be the case.

5.2 Sensor Physics

In the mass sensor mode, the sensing principle of the FBAR bases on a change of the resonating mass of the sensor. The influence of stress on the FBAR resonance frequency can be categorized into three different effects. The measurement effect directly introduces a stress in the x- and y-

direction (figure 5.4). This primary stress leads to a secondary effect in form of a deformation in the z-direction, which is usually described by the corresponding poisson ratio σ. In the case of compressive stress (as in figure 5.4), the secondary effect leads to an increase of the resonator thickness, thus increasing the length of the acoustic path leading to a decline of frequency. So the frequency can be written as:

$$f_t(S) = f_0 \frac{1}{1 + \sigma S}$$ eq. 5.1,

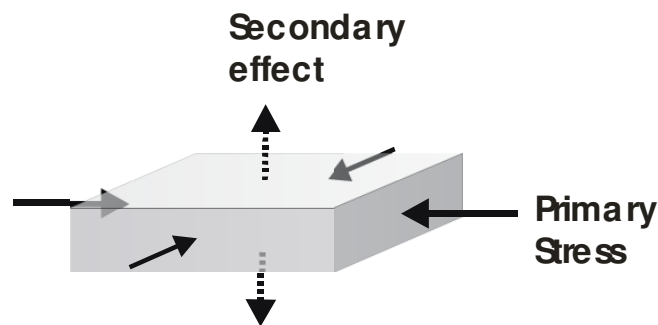where S is the strain in x-direction and σ the poisson ratio.

Figure 5.4: Influence of an externally induced stress on the sensor. The primary stress acting in both lateral directions (in this case compressive stress) is having a secondary effect with an increase of the sensor thickness.

On the other hand, the stress will alter the mass density, which has an impact on the acoustic velocity. For small strains the influence of mass density on resonance frequency results as

$$f_\rho(S) = f_0 \left(1 - \frac{(2-\sigma)S}{2} \right)$$

eq. 5.2.

Finally, there is a possible change of the elastic constants which has to do with deformation of the electron orbitals and the respective crystal lattice potentials. This dependence may be derived theoretically with the help of perturbation theory [TIE77] and has been determined experimentally for ZnO by Decremps et al. [DEC01], who carried out run-time measurements in the bulk material submitted to an external stress. This influence is described by the linear relation:

$$f_c(P) = \frac{1}{2d} \sqrt{\frac{c + \frac{dc}{dP} P}{\rho}}$$

eq. 5.3

with c the elastic constant of the respective acoustic mode, P the pressure, and d the resonator thickness.

In the experiments, the frequency dependence of two acoustic modes was investigated. The first was the longitudinal mode with the wave propagation direction and partial deflection being parallel. The second was the shear mode with the same propagation direction as for the longitudinal mode, but the particle deflection perpendicular to it. Figure 5 shows the magnitude of these influences as being calculated from equations 5.1 to 5.3.

The material constants for the longitudinal mode and for the shear mode were those obtained in bulk ZnO by Decremps. In the case of the longitudinal mode, the contributions for the different effects have opposite sign and therefore partially cancel out each other. Because the length of the acostic path and the mass density are independent of the acoustic mode, their contributions to the frequency shift are the same for both modes. In the case of the shear mode all contributions have the same sign. Therefore, the shear mode is expected to be more sensitive to an external pressure although its elastic constants are less sensitive. The theoretically obtained sensitivity is -0.0037 Hz / Pa for the longitudinal mode and 0.0162 Hz / Pa for the shear mode.
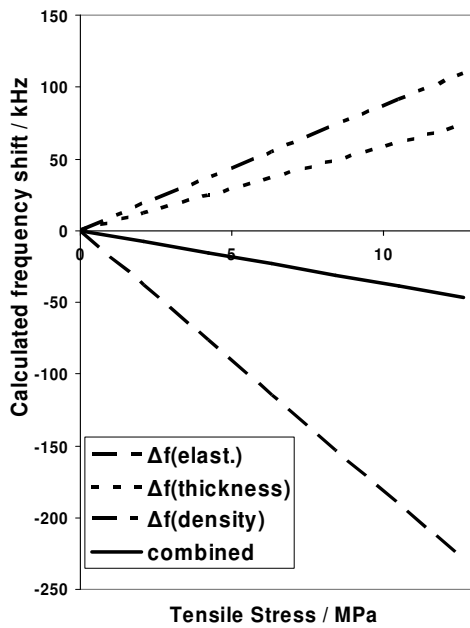
a) **b)**
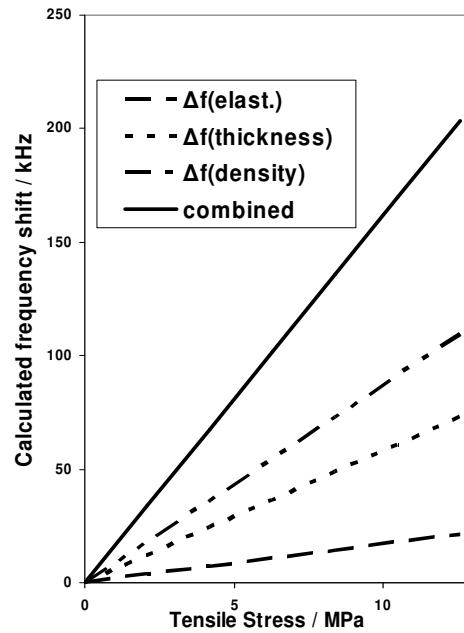
Figure 5.5: Calculated frequency shift for a) longitudinal mode and b) shear mode. The shifts for the two modes are opposite because of the different proportions for the elastic shifts.

5.3 Sensitivity

The measured deflection is shown in figure 5.7. Close to the center, there seems to be almost no deflection. To confirm the baseline adjustment also some points on the opposite side of the center were measured. The lateral strains S_1 and S_2 at the top of the substrate can be determined from the deflection of the substrate according to:

$$S_{1,2} = \frac{du}{dx}$$

eq. 5.4.

The situation is shown in figure 5.6, where the black dots show the original position of the particles. The dotted line represents the neutral (stress free) phase of the wafer, which for a homogenous wafer stretches along its center.
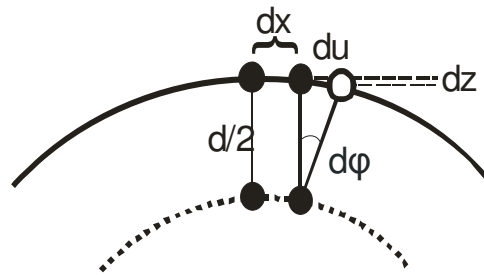
Figure 5.6: Determination of the strain from the curvature of the wafer with thickness d. Black dots: particles in their original position, open dots: particle deflected by du; dx the particle distance and dφ the variation of the angle.

For small angles it is $\sin \varphi = \varphi$, so the deflection *du* can be determined to:

$$du = d\varphi \cdot \frac{d}{2}$$ eq. 5.5.

By differentiating this with respect to x, the strain is obtained:

$$S = \frac{d\varphi}{dx} \cdot \frac{d}{2}$$ eq. 5.6 .

with dφ representing the change of the of the angle according to figure 5.6. $\dfrac{d\varphi}{dx}$ can be obtained from the curvature according to:

$$\frac{d\varphi}{dx} = \frac{d^2z}{dx^2} \cdot \frac{1}{1 + \left(\dfrac{dz}{dx}\right)^2}$$

eq. 5.7,

where dz is the deflection of the wafer.
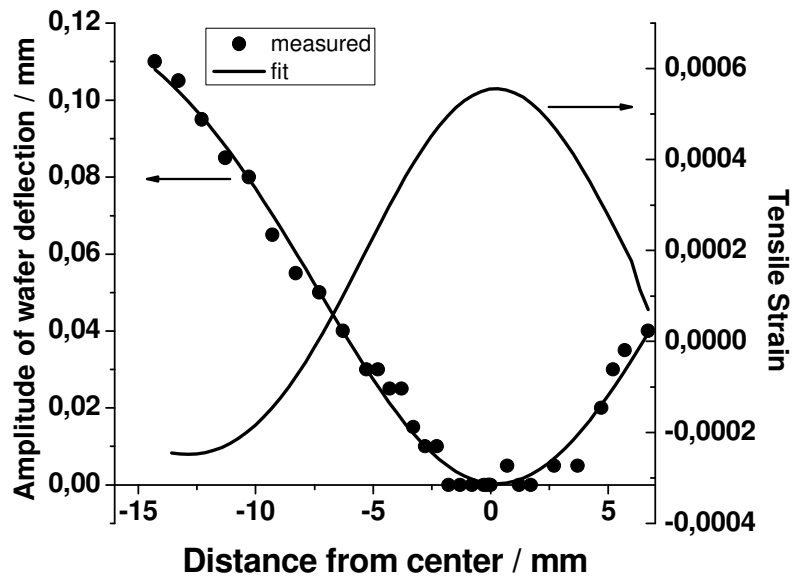
Figure 5.7: Curvature around the center of the wafer (dots and left scale). The wafer edge was deflected by 8 mm. The line represents a Gaussian fit. The corresponding tensile strain is marked at the right scale.

Because the slope in the vertex is zero, the fraction on the right side vanishes. Thus, by inserting equation 5.7 into equation 5.6, the strain can be determined to:

$$S_{1,2} = \frac{du}{dx} = \frac{d^2z}{dx^2} \cdot \frac{d}{2}$$

eq. 5.8

with d the substrate thickness, z the vertical and x the lateral direction. In order to determine the second derivative, the measured data were first fitted to a Gaussian function.
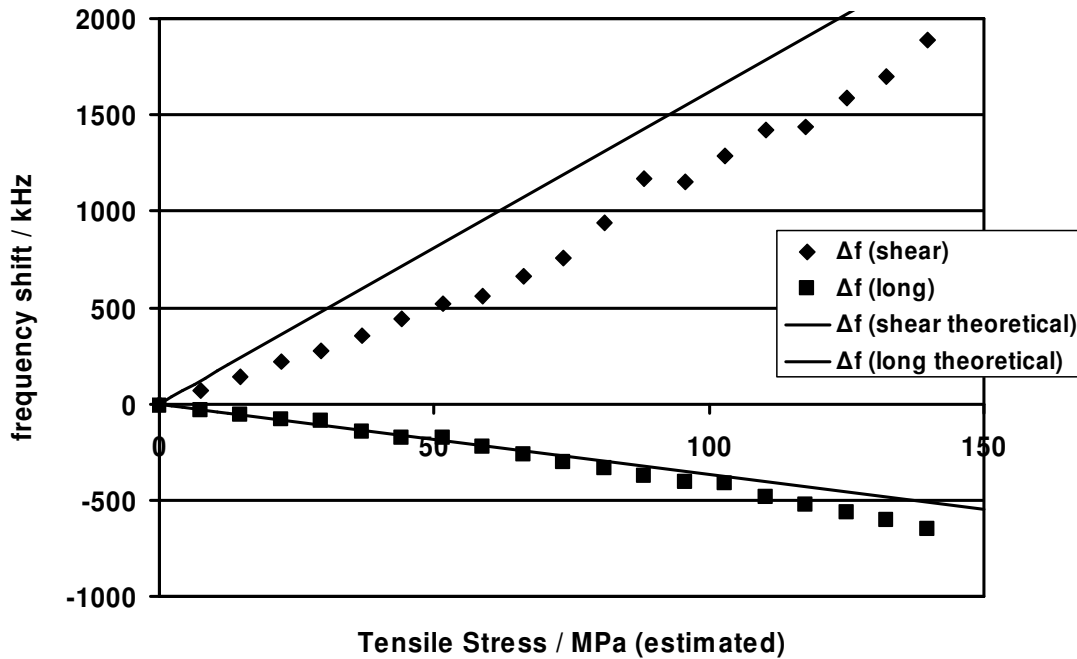
Figure 5.8: Measured and theoretical frequency shift for the longitudinal and the shear mode. The theoretical values were obtained from the calculations performed in the previous section with the values for the tensile stress being calculated from the measured wafer bending.

With this method for a deflection of 8 mm aroung the wafer edge, the strain at the vertex was determined to $5.5 \cdot 10^{-4}$. The deflections applied in the measurements ranged from 0 to 10 mm at the wafer edge. As this is still small, the curvature was assumed to be qualitatively the same for all deflections.

In the measurements, the frequency dependence of the longitudinal as well as the shear mode was determined. In figure 5.8, the magnitude of these influences calculated from equations 5.1 to 5.3 is plotted.

In figure 5.8, the sensitivities obtained from measurements are shown. The outcome of the theoretical considerations is qualitatively confirmed (shown as lines). The shear mode has a "negative"

sensitivity and the longitudinal mode a positive sensitivity which is clearly smaller. Also the linear relation seems to be holding. Nevertheless, the measurement gives a higher sensitivity than expected theoretically. Some uncertainties arising from the measurement configuration have to be taken into account. So the values for the stress sensitivity of thin film ZnO corresponds to the values obtained in bulk ZnO.

Table 5.1: Calculated and theoretical sensitivity.

Sensitivity (Hz / Pa)	Shear mode	Longitudinal mode
Theoretical	0,0162	-0,0037
Experimental	0,0158	-0,0039

Reversibility and hysteresis

In order to further classify the FBAR functionality as a stress sensor, it was tested if it showed any memory effects. It was first submitted to a tensile stress as before and the stress was then released, still continuing to measure. Figure 5.9 shows the resulting frequency shift over time. The duration of the measurement was about half an hour and memory effect was about 50 kHz.
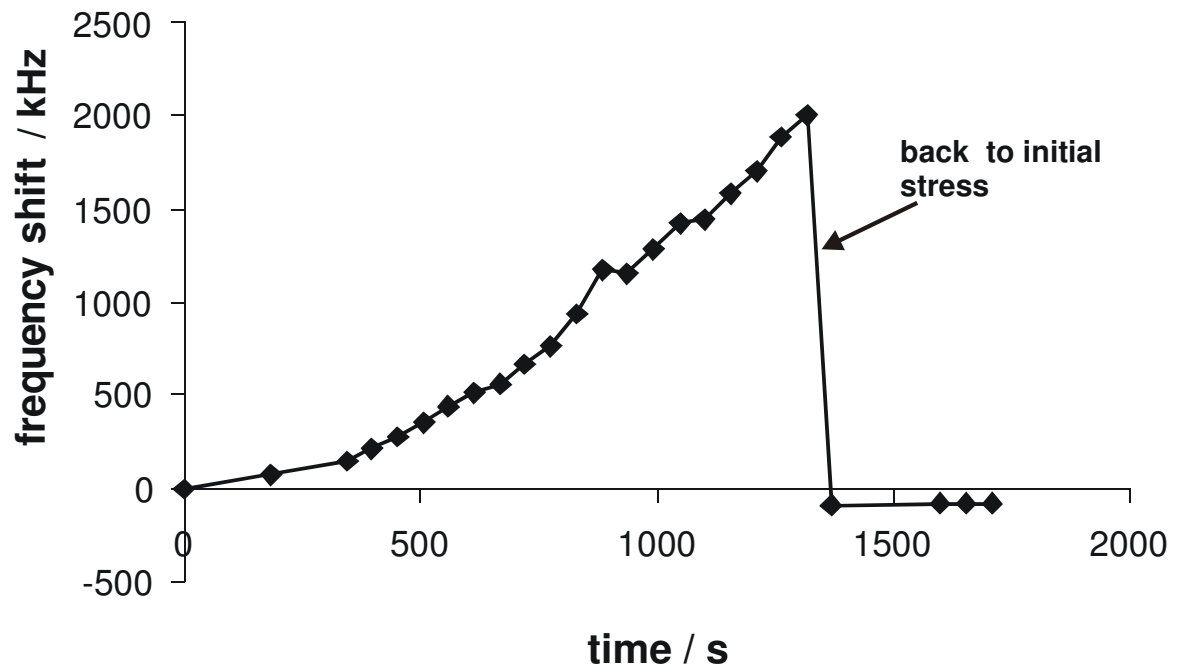
Figure 5.9: Test for possible memory effects for the stress measurement.

6.   Liquid Operation

In this chapter the operation of the sensor in liquid will be investigated in detail. One of the main designations of the sensor is the application as a biosensor. Virtually all biological reactions take place in a liquid environment. So it is necessary to know the sensor performance in liquid and the mechanisms determining the performance. Moreover, a possible application as a viscosity sensor shall be investigated. Viscosity is a parameter which plays a role in many potential applications. It is important for instance when the quality of industrial oils is monitored. The concept of viscosity sensing with bulk acoustic waves has been proven theoretically by Kanazawa et al. [KAN85]. It has been implemented using quartz crystal microbalances and was proven suitable for industrial oils [ASH03]. At present quartz crystal microbalances are a device being installed in cars in order to monitor the quality of the engine oil [HAM97]. By interpretation of damping and frequency shift of a thickness shear mode sensor it has even been possible to distinguish between different fluids such as olive and silicon oil [KUN03].

The first three sections of this chapter contain a theoretical consideration of the resonator in liquid. The first section will thereby deal with the acoustic losses and a physical model will be developed to describe the Q-factor in liquids. When the sensor is immersed in liquid, the quality factor reduces strongly. Therefore, it is useful to understand the physical loss mechanism. This will help to get an idea of the influence of frequency and the resonator acoustic properties on the viscous loss and hence the sensor performance in liquid. In the section that follows an expression for the viscosity sensitivity, the frequency change being induced by a certain change in the viscosity of liquid, will be derived. This is especially relevant for the application as a viscosity sensor. With the expression for the quality factor from section 6.1 a figure of merit will be derived for the viscosity sensor. In section 6.3 a model for the high frequency behaviour of Newtonian liquids will be introduced.

In the following experimental part measurements with liquids of different viscosities will be presented. In section 6.5, it will be investigated how the resonator parameters can be retrieved from the actual measurements. This is critical as different methods of data evaluation may yield different results. Then, the measurements with different viscosities will be presented (section 6.6). It will turn out that they show a significant deviation from the Newtonian behaviour for high viscosities. After that (section 6.7), the influence of temperature on the measurement of the viscosity is examined. Finally (section 6.8), experiments will be presented showing the ability of the FBAR as an actuator, mixing small amounts of fluid.

Theoretical considerations

6.1 Acoustic Loss in Liquids

In order to investigate the performance of a resonator immersed into a liquid, the system resonator-liquid shall be simplified to two layers. The resonator layer is assumed to be purely elastic with a finite thickness d, the liquid layer on the other hand is assumed to be purely viscous having a semi-infinite extent. The governing equations can therefore be written as:

$$\frac{d^2 u_R}{dx_3{}^2} = \frac{\rho_R}{c_R} \frac{d^2 u_R}{dt^2} \qquad\qquad \text{eq. 6.1}$$

$$\frac{d^3 u_L}{dx_3{}^2 dt} = \frac{\rho_L}{\eta_L} \frac{d^2 u_L}{dt^2} \qquad\qquad \text{eq. 6.2,}$$

where u_R is the shear displacement component within the resonator and u_L the corresponding displacement in the fluid. c_R and η_R are stiffness and mass density of the resonator and ρ_L and η_L denote the mass density and viscosity of the liquid respectively. The wave travelling in the resonator is assumed to be fully reflected on the bottom and partially reflected at the interface between resonator and fluid. So the resonator contains a wave travelling in forward as well as in backward direction. The fluid, on the other hand, is assumed to be semi infinite (the wave in the fluid is damped quite quickly, so already a very thin fluid layer can be regarded as infinite). Hence, the wave is assumed to be travelling in forward direction only. The boundary conditions are continuous stress and strain at the resonator-fluid interface and zero stress at the bottom of the resonator. According to Kanazawa the acoustic waves take the form [KAN85]:

$$u_R = 2A \cos\left(\omega_0 \sqrt{\frac{\rho_R}{c_R}} x_3 \right) e^{-i\omega t} \qquad\qquad \text{eq. 6.3}$$

$$u_L = 2Ae^{-i\left[\sqrt{\frac{\omega\rho_L}{2\eta_L}}x_3 - \omega t\right]}e^{-\sqrt{\frac{\omega\rho_L}{2\eta_L}}x_3} \qquad \text{eq. 6.4.}$$

The boundary conditions of zero stress at the resonator bottom and continuous displacement at the interface resonator fluid are already applied. The wave in the unloaded resonator takes the form of a simple half wave and the resonance condition is derived as:

$$k = \omega_0\sqrt{\frac{\rho}{c}} \qquad \text{eq. 6.5.}$$

By applying the boundary condition of continuous stress at the solid-fluid interface, the resonance condition for the resonator in liquid is obtained. Comparing this with the resonance of the unloaded resonator, Kanazawa obtains the frequency shift:

$$\Delta\omega = -\frac{\omega^{3/2}}{\pi}\sqrt{\frac{\rho_L\eta_L}{2\rho_R c_R}} \qquad \text{eq. 6.6.}$$

In the following, the change in attenuation and the corresponding quality factor caused by the liquid will be derived. The dissipated energy density of an acoustic wave is given by [ROS88]:

$$\frac{dE_{diss}}{dx_3} = \frac{1}{2}\frac{d}{dt}\omega^2\eta\left(\frac{du}{dx_3}\right)^2 \qquad \text{eq. 6.7.}$$

The components x_1 and x_2 have been left out because a one dimensional system is assumed. Inserting equation 6.3 into 6.7 yields the dissipated energy of the resonator:

$$\frac{dE_{res}}{dx_3} = 4j\omega^3\eta_R A^2 \sin^2\left(\omega_0\sqrt{\frac{\rho_R}{c_R}}x_3\right)e^{2i\omega t} \qquad \text{eq. 6.8,}$$

where viscous damping η_R in the resonator has been introduced. As one is only interested in the time integrated energy density, the time dependent part may be left out and the dissipated energy within the resonator can be determined by integrating over resonator thickness:

$$E_{res} = \int_0^d 4\omega^3\eta A^2 \sin^2\left(\omega\sqrt{\frac{\rho_R}{c_R}}x_3\right)dx_3 \qquad \text{eq. 6.9.}$$

Because the operation frequency is close to the resonance frequency of the unloaded resonator, ω may be replaced by $\omega_0 = \sqrt{\frac{\mu_R}{\rho_R}}\frac{\pi}{d}$. Solving the integral thus leads to

$$E_{res} = 2\omega^3\eta_R A^2 d \qquad \text{eq. 6.10.}$$

Now the same procedure will be carried out for the fluid. Applying equation 6.7 with the displacement in the fluid (equation 6.4) yields:

$$\frac{dE_{liq}}{dx_3} = 4A^2\omega^4\rho_L e^{-j2\left[\sqrt{\frac{\omega\rho_L}{2\eta_L}}x_3-\omega t\right]}e^{-2\sqrt{\frac{\omega\rho_L}{2\eta_L}}x_3} \qquad \text{eq. 6.11}$$

As before the time dependent part will be left out and integration over the fluid is performed:

$$E_{liq} = \int_0^\infty 4A^2\omega^4\rho_L \cos\left(2\sqrt{\frac{\omega\rho}{2\eta_L}}\right) e^{-2\sqrt{\frac{\omega\rho}{2\eta_L}}x_3} dx_3 \qquad \text{eq. 6.12.}$$

Evaluation of the integral leads to

$$E_{liq} = A^2\omega^{7/2}\sqrt{8\eta_L\rho_L} \qquad \text{eq. 6.13.}$$

The Q-factor of the resonator immersed in liquid can be written in terms of the energy dissipated in the resonator and the liquid:

$$Q = Q_0\left(1 + \frac{E_{liq}}{E_{res}}\right)^{-1} \qquad \text{eq. 6.14}$$

with Q_0 the Q-factor of the unloaded resonator. So for the change of the quality factor only the relation of the energy dissipations is needed which justifies the approach of only integrating over the x_3 direction. Inserting equations 6.13 and 6.10 into 6.14 thus yields the Q-factor of the resonator in fluid:

$$Q = Q_0\left(1 + \omega^{5/2}\sqrt{\frac{2\eta_L\rho_L\rho_R}{c_R}}\frac{1}{\pi\eta_R}\right)^{-1} \qquad \text{eq. 6.15.}$$

The viscous loss in the resonator η_R can be replaced with the Q-factor of the unloaded resonator Q_0. It is [ROS88]:

$$\eta_R = \frac{c_R{}^2}{\omega \rho_R Q_0}$$
<div align="right">eq. 6.16.</div>

So Q becomes:

$$Q = Q_0 \left(1 + \omega^{5/2} \sqrt{\frac{2\eta_L \rho_L \rho_R{}^3}{c_R{}^5} \frac{Q_0}{\pi}} \right)^{-1}$$
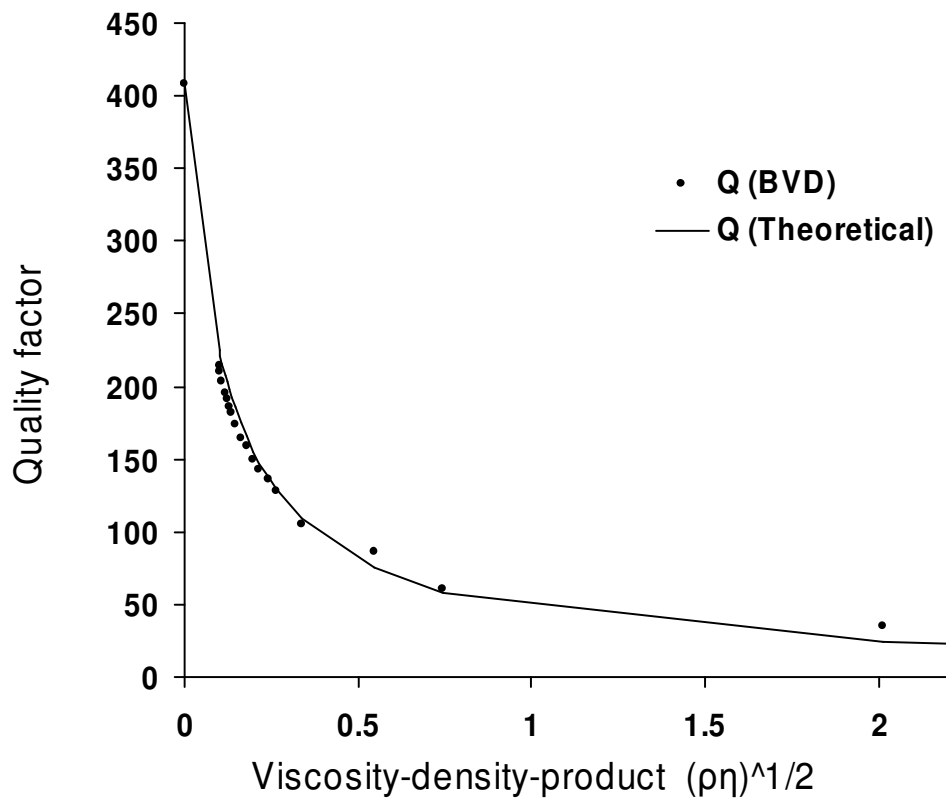<div align="right">eq. 6.17.</div>

Figure 6.1: Validation of the model for the quality factor of a resonator in liquid (equation 6.17): theoretical values for Q are compared with those measured for liquids with different viscosities.

This expression has a form resembling the expression for the frequency shift and can therefore be written:

$$Q = Q_0 \left(1 - \Delta\omega \cdot 2Q_0\omega\frac{\rho_R{}^2}{c_R{}^2} \right)^{-1} \qquad \text{eq. 6.18.}$$

Now $\Delta\omega$ will be extracted and given the name $\Delta\omega_Q$:

$$\Delta\omega_Q = \frac{Q - Q_0}{2Q_0 Q\omega\dfrac{\rho_R{}^2}{c_R{}^2}} \qquad \text{eq. 6.19.}$$

If the liquid is Newtonian (i.e. purely viscous), $\Delta\omega_Q$ as it is determined above will be the same as the frequency shift $\Delta\omega$. So $\Delta\omega_Q$ can be consulted in order to judge whether a fluid is Newtonian or not. Equation 6.17 was verified by measurements with liquids of different viscosities (see section 6.4 for a detailed description of these experiments) and shows quite good agreement with the measured values (see figure 6.1).

Equation 6.17 can now be used in order to make an assessment for the impact of the liquid on the resonator performance. In figure 6.2, the quality factors for different Q_0 are shown versus frequency. For Q_0, a value of 100, 500 and 1000 was chosen, which is about in the range being achievable with current technology. The frequency range is between 500 MHz and 3.5 GHz. According to this model, the Q-factor is strongly decreasing with increasing resonance frequency, with the quality factor at 3 GHz only about 10 for all resonators. Moreover, the decrease of the quality factor is much stronger when the unloaded Q is higher. At 500 MHz, the quality factor for the Q_0=100-resonator downgrades only little, the Q_0=500-resonator on the other hand is down by almost a half.
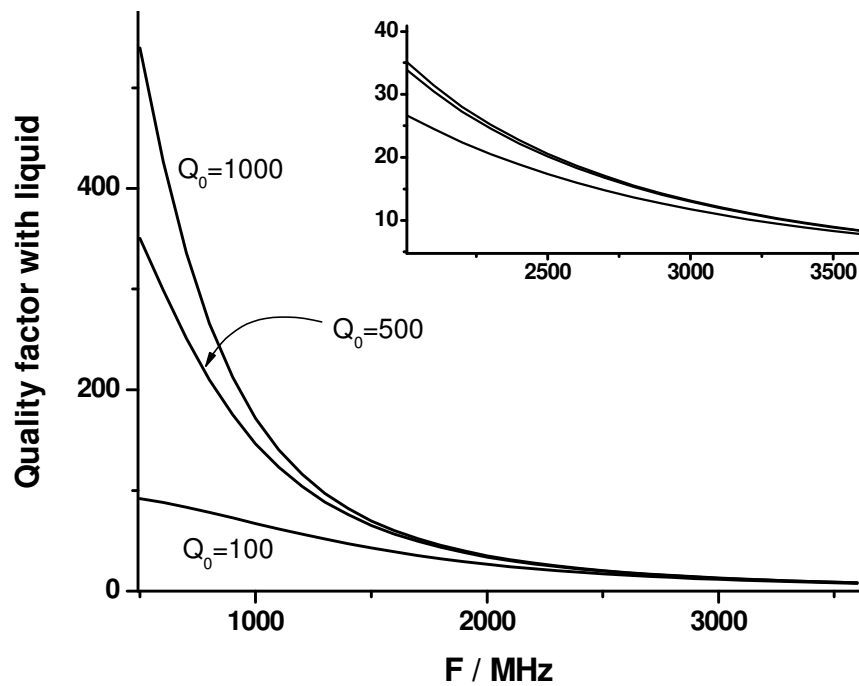
Figure 6.2: Dependence of the Q-factor on frequency for resonators immersed in water with different unloaded Q_0.

One strategy to improve the quality factor in liquid according to equation 6.17 would be to choose a resonator with a larger shear modulus. Having a larger shear modulus, less acoustic energy is expected to penetrate into the liquid and the quality factor to be accordingly higher. In figure 6.3 the quality factors are shown for different resonators all having an unloaded Q of 1000, when the acoustic properties of different materials are inserted into equation 6.17. Apart from ZnO, the material properties of tungsten and iridium were inserted. It can be seen, that a considerable improvement is achieved, especially for higher frequencies. So when higher frequencies are required (for instance in order to enhance the packaging density, see chapter 4), the use of a material with high shear modulus may be a strategy to improve the resonator performance in liquid. Although the materials shown are not piezoelectric, an overmoded setup could be used, with the materials mentioned having contact with the liquid.
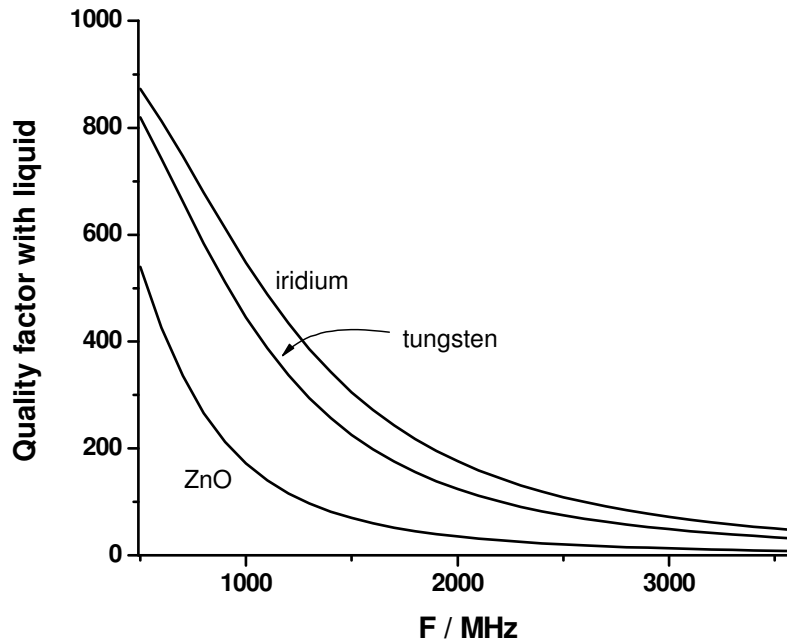
Figure 6.3: Quality factors obtained for different material properties. The quality factor of the unloaded resonator Q_0 was assumed to 1000. Choosing a material with a higher acoustic imped-ance (tungsten or iridium) an improvement of the quality factor in water can be achieved.

6.2 Application as a Viscosity Sensor, Sensitivity

In this section, the application of an FBAR as a viscosity sensor will be examined. The aim is to obtain an equation for the viscosity sensitivity relating the sensor response to a change of viscosity. One may assume an operation in the regime of a Newtonian fluid (whether it is Newtonian or not will be discussed in the next section) and start from the Kanazawa equation (equation 6.6):

$$\Delta\omega = -\frac{\omega_0^{3/2}}{\pi}\sqrt{\frac{\rho_l \eta_l}{\rho_R c_R}} \qquad\qquad \text{eq. 6.20.}$$

Now it may be further assumed that only the viscosity is changing. Differentiating with respect to the viscosity yields the viscosity sensitivity:

$$s_\eta = \frac{d}{d\eta_l}\Delta\omega = \frac{1}{2\pi}\omega_0^{3/2}\sqrt{\frac{\rho_l}{\rho_R c_R}}\cdot\frac{1}{\sqrt{\eta_l}}$$ eq. 6.21.

Unlike the mass sensitivity which is independent of the measurand in the range of small mass attachments (see chapter 2.5) the viscosity sensitivity also depends on the viscosity itself. The sensitivity is greater for smaller viscosities. It increases with $1/\sqrt{\eta}$. Note that this is just the sensitivity, for viscosity resolution, however, also the noise and Q-factor must be taken into account, which will further reduce resolution for larger viscosities.

For water at 20°C and an FBAR at 700 MHz the viscosity sensitivity can be calculated from equation 6.21, resulting in s_η = 334 kHz / mPa·s. Because of the viscosity dependence, this sensitivity only holds for small viscosity changes. As viscosity is also temperature dependent, a single sensitivity has to be evaluated for every temperature. From stability measurements in water a minimum detectable frequency shift of 2.6 kHz could be determined (see chapter 7). So the minimum detectable viscosity change will be $\Delta\eta_{min}$ = 7.7·10^{-3} mPa·s for water and a temperature of 20°C.

Analogue to the consideration in chapter 7 a figure of merit s·Q can be defined using the expression for the quality factor from equation 6.17:

$$FOM = Q(\eta_l)\cdot s_\eta = Q_0 \frac{\dfrac{1}{2\pi}\omega_0^{3/2}\sqrt{\dfrac{\rho_l}{\rho_R c_R}}\cdot\dfrac{1}{\sqrt{\eta_l}}}{1+\omega_0^{5/2}\sqrt{\dfrac{2\eta_l\rho_l\rho_R^{3}}{c_R^{5}}}\dfrac{Q_0}{\pi}}$$ eq. 6.22.

As will be shown in section 6.6, for Newtonian fluids a change in attenuation accompanies the frequency change. This change of the quality factor can also be used in order to measure the viscosity

change of a fluid. So in addition to the "frequency-method" there exists a "damping-method". Differentiating the expression for the quality factor with respect to η_l the "Q-sensitivity" is obtained:

$$\frac{\Delta Q}{\Delta \eta_l} = -\frac{Q_0 \omega^{5/2} C}{2\sqrt{\eta_l} + 4\omega^{5/2} C \eta_l + 2\omega^5 C^2 \eta_l^{3/2}} \quad \text{with } C = \sqrt{\frac{2\rho_l \rho_R}{c_R^5}} \frac{Q_0}{\pi} \qquad \text{eq. 6.23.}$$

For low viscosities the term containing the first power of η_l in the numerator can be neglected:

$$\frac{\Delta Q}{\Delta \eta_l} = -\frac{Q_0 \omega^{5/2} C}{2\sqrt{\eta_l} + 2\omega^5 C^2 \eta_l^{3/2}} \qquad \text{eq. 6.24.}$$

Hence, in comparison to the frequency-method, this sensitivity does not only depend on frequency and viscosity but also on the quality factor of the unloaded device. Nevertheless, this dependence is not linear or not even continuous as the denominator contains one term that is constant and another that is quadratic in Q_0.

From stability measurements here, too, a minimum resolution for the quality factor could be determined. The resolution for Q was determined to 0.24. With an unloaded Q of 400 and a resonance frequency of 700 MHz this leads to detection limit of $4 \cdot 10^{-3}$ mPa·s. So it is slightly lower than for the frequency-method.

6.3 Viscous and Elastic Behaviour

In order to understand the relation between the viscous and the elastic behaviour of a medium a simple consideration shall be made. A force is applied to layer A, causing a shear displacement relative to the neighbouring layer B which is assumed to be immobile. A perturbation relative to the equilibrium state is thus induced and a force will be acting between the two layers. This is schematically shown in figure 6.4. Two principle effects can be thought of as a response to this force:

the energy can be stored in the electromagnetic fields that hold together the medium. In this case, when the force, having caused the displacement, is released, the potential energy can be restored and will cause an acceleration. So all the energy will be restored and the medium is acting purely elastically.

Now think of the same procedure but this time the force on layer A is maintained for a while. After some time the energy may be transferred to the particles causing internal friction and leading to a deformation of the system in a way that they find a new energetic minimum regarding the position of A and B. In this case, the energy induced will be "lost" and the new position will be maintained. So the medium is acting viscously. The average time to reach the new equilibrium is the relaxation time τ.

When the displacement applied is periodic, the medium will act viscously whenever the time period of the displacement is larger than the relaxation time. When, on the other hand, the time period of displacement becomes shorter than relaxation time, the energy will have no time to be transformed to the particles and hence only an exchange between potential and kinetic energy will take place. For this model, Mason derived an expression for the compliance and the viscosity describing the transition from viscous to elastic behaviour [MAS65]:

$$c = \frac{c_\infty \omega^2 \tau^2}{1 + \omega^2 \tau^2} \xrightarrow{\omega \to \infty} c_\infty \qquad \text{eq. 6.25}$$

$$\eta = \frac{c_\infty \tau}{1 + \omega^2 \tau^2} \xrightarrow{\omega \to 0} c_\infty \tau = \eta_0 \qquad \text{eq. 6.26,}$$

where in the second relation $c_\infty \tau$ could be defined as low frequency viscosity. Like friction forces in general also the viscosity is proportional to velocity. Thus, the general stress-strain relation for a viscoelastic medium becomes

$$\frac{dF}{dA} = \eta \frac{d^2 u}{dt dx_3} + c \frac{du}{dx_3} \qquad \text{eq. 6.27,}$$

where the shear force was assumed to be perpendicular to the x_3-direction. Differentiating this equation, the left side can be replaced by mass density times acceleration:

$$\rho \frac{d^2u}{dt^2} = \eta \frac{d^3u}{dtdx_3^2} + c \frac{d^2u}{dx_3^2}$$

eq. 6.28.
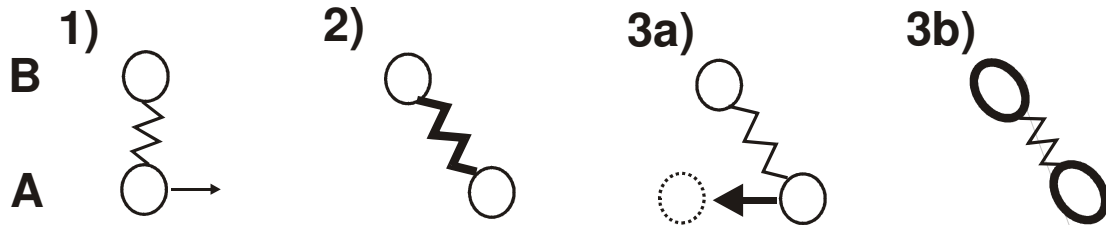
Figure 6.4: Schematic behaviour of the medium submitted to a shear force: is the duration of deformation only short, then all the energy will be stored in the field between the two layers (2) and will be converted into kinetic energy when the force is released (3a). This is equivalent to an elastic behaviour of the medium. Is the duration of the deformation longer than the relaxation time τ, a transformation of energy will take place so that the system finds a new energetic minimum (3b). The energy is being dissipated and the medium is acting viscously.

With the above relation this can be written as

$$\rho \frac{d^2u}{dt^2} = \frac{c_\infty \tau}{1 + \omega^2\tau^2} \left[\frac{d^3u}{dtdx_3^2} + \omega^2\tau \cdot \frac{du^2}{dx_3^2} \right]$$

eq. 6.29.

Experimental

6.4 Measurements with Newtonian Fluids

In order to be able to carry out measurements with the sensor in liquid, a simple fluidic system was designed and built[5]. As the sensor is still in the development stage and produced on a wafer level, the sensor layout was designed in order to enable electrical contact as well as the application of the fluidic system on top of the wafer. The flow cell was open on top, thus enabling an easy application of the fluid with a syringe. Measurements were carried out to determine the sensor response depending on the viscosity of the fluid. As a model fluid system, glycerol-water solutions were used, because they are known to be Newtonian and the viscosity can be tuned quite precisely and over a great range by choosing the mixing ratio of the two fluids.

The system was put into measuring state, which consisted in electrically contacting the sensor and applying the flow cell. Sets of measurements with different glycerol-water solutions were carried out maintaining the system in measuring state. This had the advantage that the sensor system remained unchanged during one measurement. Mixing of the fluids was done inside the flow cell. Two different methods were applied, one in the diluting direction, starting with the highly viscous glycerol and reducing the viscosity by subsequently mixing with water. For the reverse direction, it was started with water and glycerol was added consecutively. Comparison of the outcome for both methods served to evaluate the success of the mixing. The volume of the fluid in the cell was always between 50 and 180 µl. To maintain this volume, in some steps a certain amount of fluid was removed before adding new fluid. For the right dosage, an Eppendorf$^{®}$ µl-pipette was used with an adjustable volume between 10 and 100 µl. Homogeneity of the fluid was achieved by mixing the contents of the flow cell thoroughly, taking out at least one third of the fluid cell content and pumping it in again, a step that was repeated for at least ten times. Mixing properly was critical, as due to the wafer layout the sensor is located at the edge of the flow cell.

---

[5] Construction of the flow cell was carried out by Matthias Schreiter.

Figure 6.5: Setup for the liquid measurements. The flow cell was positioned onto the wafer and mixing of the fluids was done directly on the wafer.

The results obtained for both mixing methods, the dilution and the reverse direction, proved to be qualitatively the same. A systematic error could be principally expected from improper mixing. This could for instance lead to a local deviation of the mixing ratio of the fluid. Especially, it may be possible that the mixing ratio in vicinity of the sensor, which is situated in the corner of the flow cell, lags behind the overall mixing ratio. Nevertheless, no such systematic error could be observed and the results obtained for both mixing methods showed the same qualitative behaviour.

For each fluid mixture at least three measurements were carried out, reading out the impedance characteristic of the sensor. Further experiments were carried out changing the temperature of the fluid. The temperature was controlled with an ERS Aircool SP72 thermo chuck.
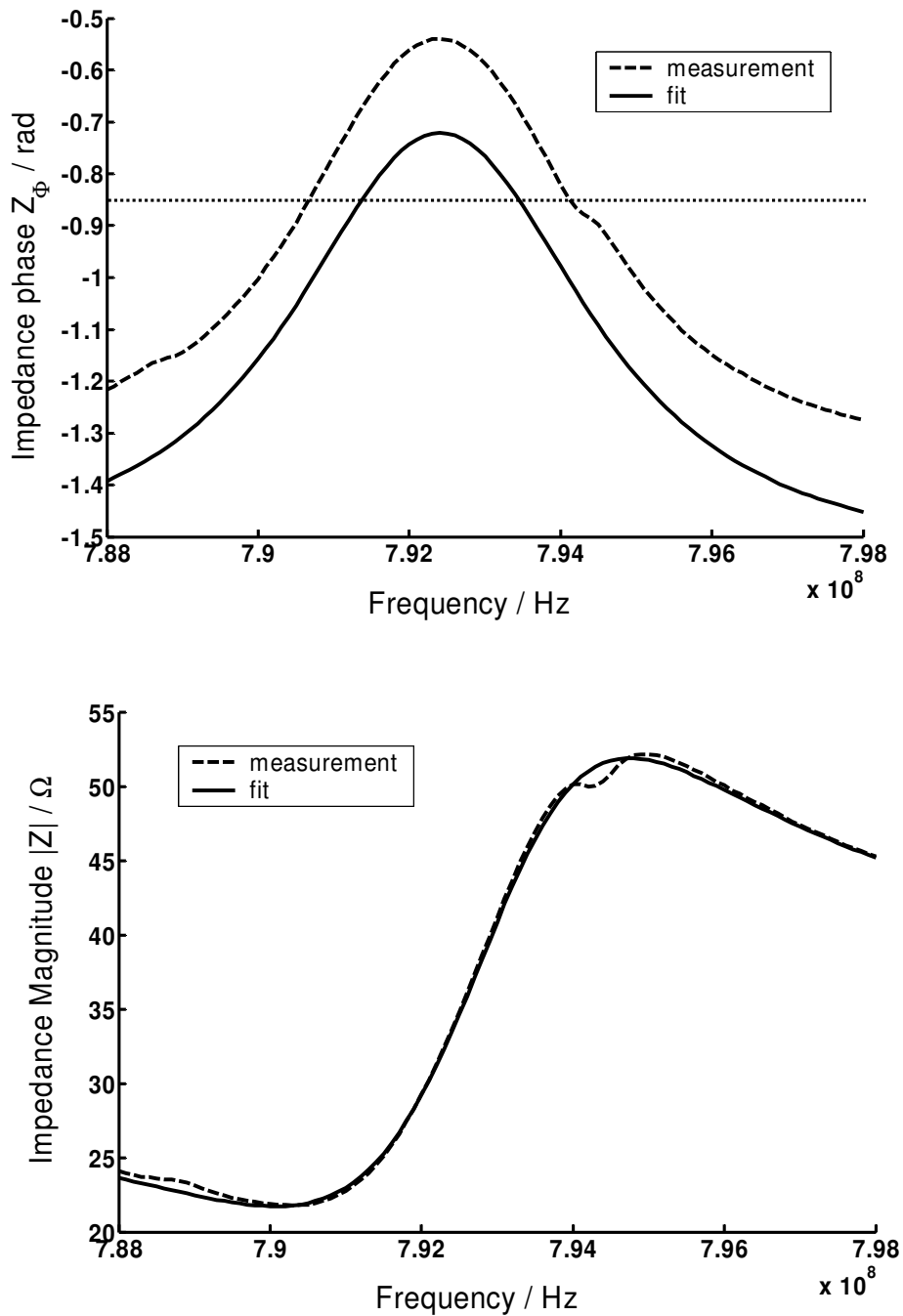
Figure 6.6: Measurement and fit of impedance magnitude and phase for the resonator used in the experiments. The magnitude can be very well fitted, whereas the measured phase is found often to be shifted by a fixed amount with respect to the calculation. The dashed horizontal line marks the phase at which the resonance is determined (details see text).

6.5 Determination of the Resonator Parameters

As the FBAR is operating as a sensor, it is important to exactly evaluate the resonance frequency and the attenuation. The intrinsic acoustic parameters are especially important, as viscosity or viscoelasticity have an impact mainly on the acoustic properties of the system sensor-fluid. Behling et al. [BEH98] investigated the frequency shifts for a quartz crystal microbalance determined with different evaluation methods. They found that especially for large attenuation, the series and parallel resonances drift apart. Two principal methods exist for frequency determination, one is to extract certain characteristic points in the impedance characteristic. The other bases on a fitting of the impedance characteristic to an equivalent circuit model. In the frame of this work, a fitting method using a BVD equivalent circuit (see chapter 2.3) was applied, supposing that this method is the best method available to obtain the intrinsic resonator values.

An example of measurement and fit of the impedance phase and magnitude is shown in figure 6.6. The measured values (dashed line) show two substructures on the rising and on the trailing edge, respectively. They have a spacing of about 7 MHz. These structures can be identified as resonances originating from the silicon substrate. Such substrate resonances appear when the acoustic mirror is not working optimally. The reason for this is the thin film process which is not yet fully optimized and might exhibit some thickness fluctuations. The acoustic mirror for this specific resonator had a maximum reflection at 800 MHz. As the wafer is much thicker (about 500 μm) than the resonator, however, the substrate resonances have a considerably lower sensitivity than the main FBAR resonance. Hence, they will practically remain at the same position throughout the measurement. When the FBAR resonance shifts and therefore a substrate resonance approaches a characteristic point, this can lead to a jump in the measured resonance frequency. A result obtained with a fitting method can equally be affected by substrate resonances as the fit may jump from one local minimum of the functional (the functional being the absolute difference of measured and fitted impedance) to another. So it is important for resonator optimization to avoid any substrate resonance.

Nevertheless, comparison of measurement and fit in figure 6.6 shows the fit to match the measured frequency quite exactly. In the impedance phase, however, there is a constant offset between the measurement and the fit. The leads connecting the resonator have a length of 750 μm and contribute only less than 1% to the phase shift, which converts into a phase shift of only 0.02 degrees. To explain the observed constant offset between calculation and measurement, we have to assume an acoustic effect of unknown origin.
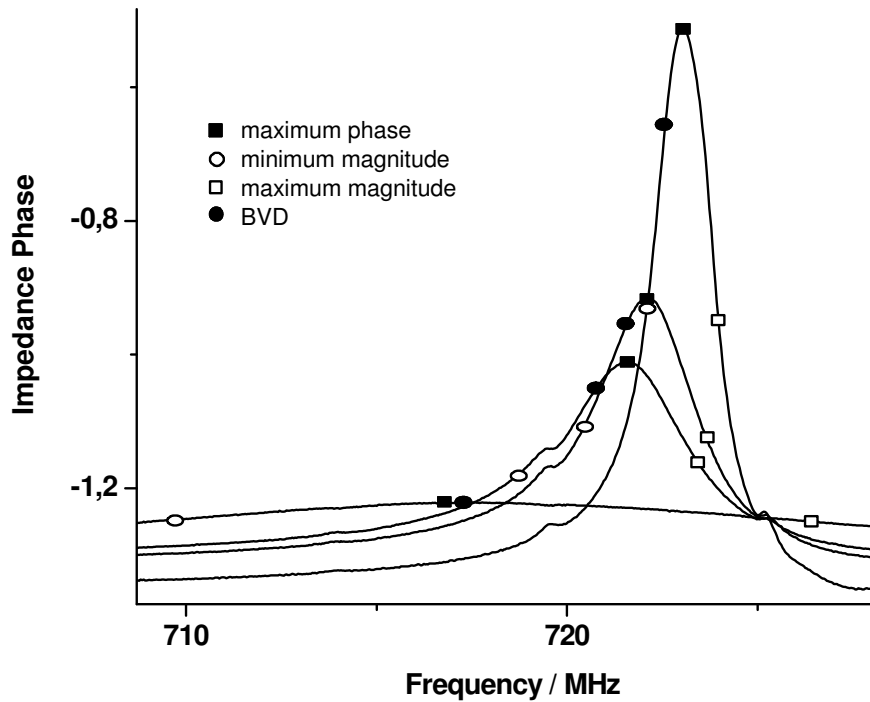
Figure 6.7: Resonance frequencies determined for resonances in air, water, glycerol-water solution (1:2) and pure glycerol. The squares and circles mark the resonance frequency points determined with different methods: maximum phase, minimum and maximum magnitude and BVD-fit.

In comparison to selecting certain characteristic points a fitting method has the advantage of taking into account all the measured points within the measured frequency band therefore providing a greater exactness of the result. Depending on the evaluation method applied, it is yet not always possible to use a fitting method. This is the case when for instance a simple oscillator or frequency counter is used for readout.

Therefore, various methods of the frequency determination from characteristic points in the electric impedance were also examined. These different methods are also discussed in the literature on quartz crystal microbalances [BEH98]. The disadvantage that only one point is used for frequency determination was compensated by carrying out a preliminary smoothing of the resonance curve. This was achieved by a ten point averaging of the resonance.
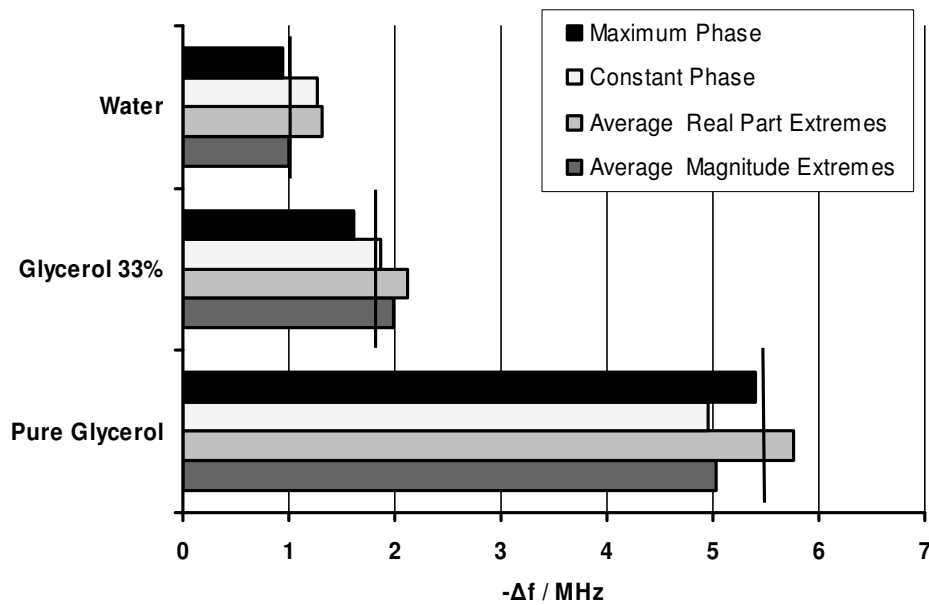
Figure 6.8: Frequency shift for different determination methods. The lines mark the frequency shift determined from the BVD model, which should be the intrinsic acoustic frequency of the device. For higher viscosities and consequently higher attenuation deviation becomes stronger. Especially the frequencies determined from the minimum and maximum of the impedance curve strongly drift apart. For high damping, evaluation of the maximum phase is the most exact method for frequency determination, due to the rather symmetric form of the phase curve. For smaller damping, averaging the values of series and parallel frequency seems to be the most exact method.

The results for the frequency shifts are plotted in figure 6.8. The values from the BVD-fit are shown as a line. When the product of coupling and Q-factor becomes very small, the frequency shifts obtained from the minimum and maximum of the real part or the magnitude of the impedance are moving apart. Therefore, the average values between the respective maximum and minimum values were evaluated.

6.6 Transition from Viscous to Elastic Behaviour

As described in the first section of this chapter, a magnitude $\Delta\omega_Q$ (or Δf_Q) can be determined in order to evaluate the character of the fluid as Newtonian or not. In figure 6.9, the measured frequency shifts and the frequency shifts according to equation 6.6 (the expected frequency shift determined from the damping) are shown. All the plotted values were determined from a BVD fit. For low vis-

cosities up to a mixing ratio with 80/20 (glycerol/water) a nearly perfect proportionality between Δf and Δf_Q is found. Hence, it can be stated that here, the fluid behaves Newtonian. Above 80% glycerol the values start to deviate, that is the real frequency shift are smaller than the f_Q-values, or the damping is higher. For pure glycerol the "real" frequency shift is 6.7 MHz, whereas the damping-shift is 9.1 MHz.
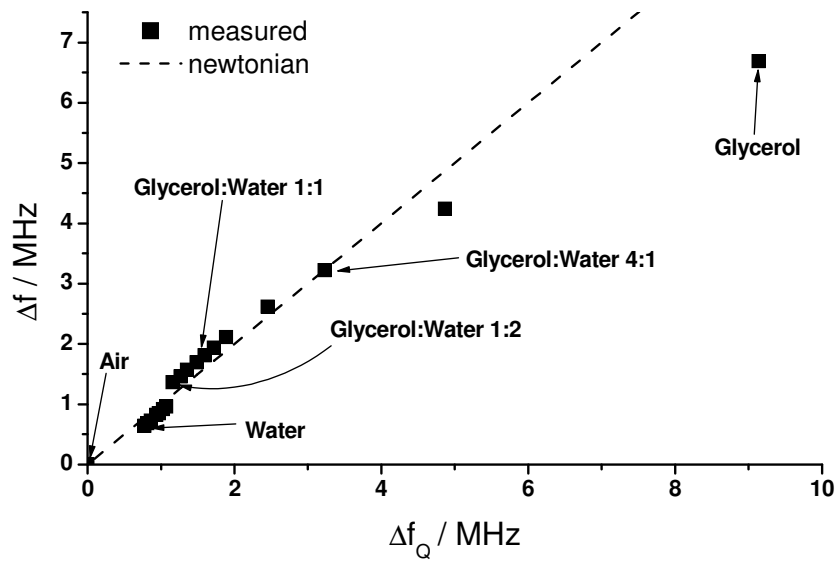
Figure 6.9: Newtonian behaviour of the liquid for different glycerol water solutions: for a mixing ratio up to 4:1 of Glycerol:Water the fluid behaves like a Newtonian fluid. For mixing ratios above that value, either the frequency shifts are lower than for a Newtonian fluid or the damping is higher.

The observed frequency shifts will now be compared to the shifts expected from the model for an elastic single layered resonator with a viscous overlayer (section 1). Recall the frequency shift derived by Kanazawa (equation 6.6):

$$\Delta\omega = -\frac{\omega^{3/2}}{\pi}\sqrt{\frac{\rho_L \eta_L}{2\rho_R \mu_R}} \qquad\qquad \text{eq. 6.30.}$$

The frequency shift is expected to be a linear function of $\sqrt{\rho_L \eta_L}$. In figure 6.10, it is plotted accordingly. Here is seen quite nicely, that for low viscosities the frequency shift as well the damping match the prediction very well. For viscosities above $\sqrt{\rho_L \eta_L} = 2\, g/\left(cm^2 \sqrt{s}\right)$, the frequency shifts deviate strongly from the prediction and there seems to be a saturation. So the properties of the fluid as being measured with the FBAR device seem to be constant for fluid mixtures containing more than 89% glycerol. The measurements were repeated several times and conducted with different methods, starting with pure glycerol first as well as with pure water, increasing and decreasing the viscosity respectively (see section 6.3). Further measurements were also carried through with a preliminary mixing in a bottle. Therefore effects like an inhomogeneous mixing which could lead to the sensor to "see" a different concentration, can be ruled out.

This behaviour of the fluid, namely exhibiting constant properties for a certain concentration of glycerol, has already been reported by other authors ([HOU91], [JAK98]). It was interpreted as an elastic behaviour. From the damping in this supposedly elastic regime the high frequency shear modulus can be determined. As all the energy penetrating into the liquid is lost, the Q-factor of the system resonator-fluid can be written as:

$$\frac{1}{Q} = \frac{1}{Q_R} + \frac{1-|R|}{\pi} \qquad \text{eq. 6.31}$$

with R the reflection of the acoustic wave at the resonator-fluid interface. Using the definition $R = \left(Z_R - Z_L\right)/\left(Z_R + Z_L\right)$, the acoustic impedance of the liquid is obtained:

$$Z_L = Z_R \frac{\pi(Q_R - Q)}{2Q_R Q - \pi Q_R + \pi Q} \qquad \text{eq. 6.32.}$$
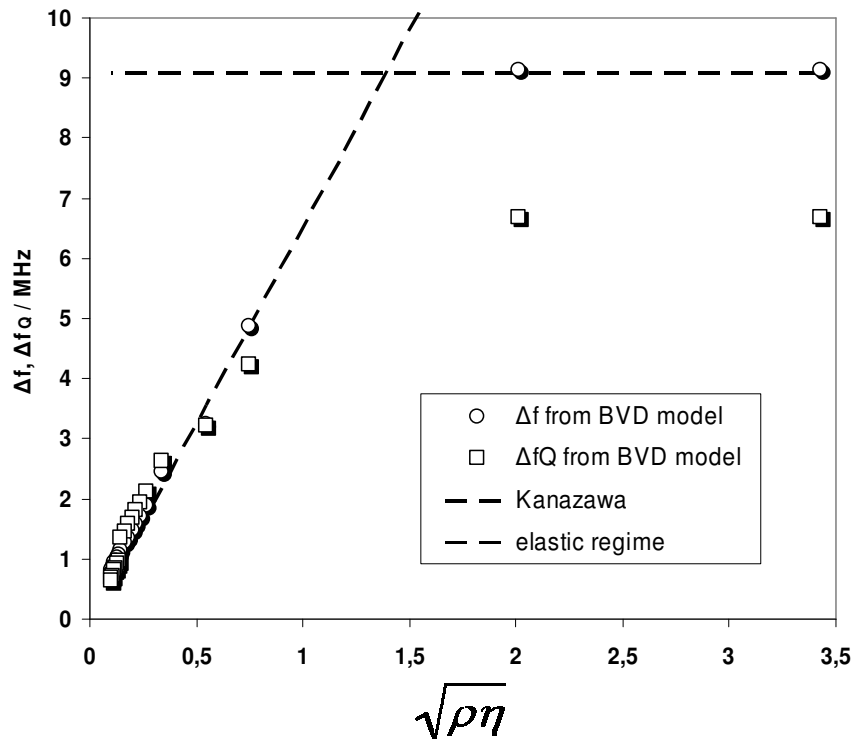
Figure 6.10: Transition from viscous to elastic behaviour, as observed for different mixtures of water and glycerol: for low viscosities the damping matches the theoretical prediction of the Kanazawa model, for high viscosities it saturates and reaches a constant, corresponding to a high frequency shear modulus of $2 \cdot 10^9$. This is significantly larger than the values found in literature which were $7 \cdot 10^7$ N/m² [JAK98] or $5 \cdot 10^8$ N/m² [HOU91].

With $c = \dfrac{Z_L{}^2}{\rho}$, we thus find for the shear modulus c = $2 \cdot 10^9$ N/m². This is a somewhat larger value than the ones obtained by Jakoby and Hoummady which were $7 \cdot 10^7$ N/m² and $5 \cdot 10^8$ N/m² respectively. Those values, however, have been obtained with a Love wave sensor in the first case and a SAW sensor, respectively.

6.7 Temperature Dependence

In a further experiment, the influence of temperature on a fluid measured with an FBAR was investigated. In figure 6.11 this influence is shown. The resonance frequency decreases with increasing temperature. The FBAR, however, has a frequency sensitivity on its own. This internal FBAR tem-

perature response was measured seperately, and then substracted from the frequency shift in fluid. With the values for the temperature dependent viscosity taken from literature [LID95], the frequency shift that is expected from this change was calculated according to equation 6.6. It shows a good agreement with the normalize measured values. So the influence of temperature on the water and the resonator can be separated quite clearly.
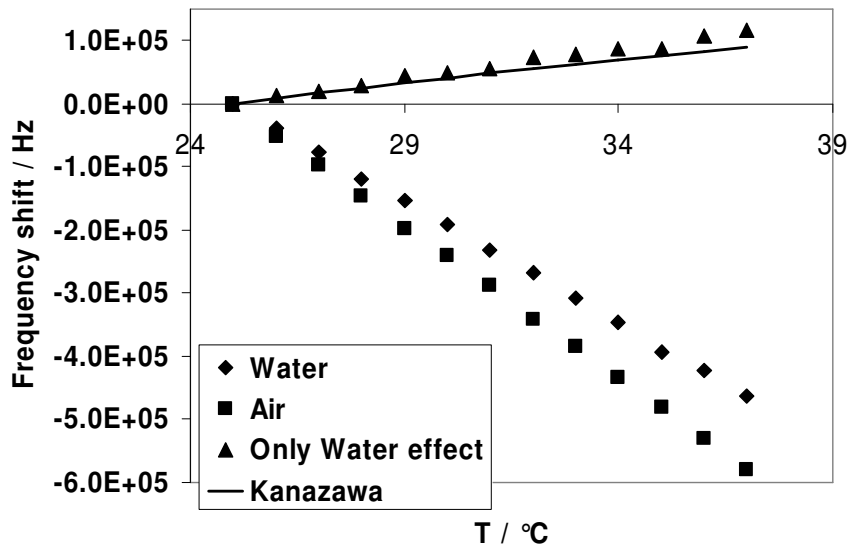
Figure 6.11: Temperature response of an FBAR covered with water: Normalizing the observed frequency shift to the one of the FBAR in air yields the frequency shift that is expected from the temperature induced change of the viscosity of water.

6.8 FBAR as a Fluidic Mixer

When the FBAR is driven at sufficiently large amplitude, it can be used as an actuator. A displacement of the particles with an acoustic wave, when strong enough, will lead to a particle diffusion and the corresponding induction of a fluid flow. Such an agitation with bulk waves has been described by Zhu et al. with PZT-based bulk acoustic resonators [ZHU98]. A fluidic mixer has even been brought to market using surface acoustic wave technology [TOE03] and is employed for Protein and DNA microarrays in order to reduce reaction time and enhance the reproducability and homogeneity of the biochemical reactions.

Employing c-axis inclined piezoelectric ZnO layers with inclination angles between 0 and 45° both the longitudinal mode and the shear mode can be excited. So it would be possible to realize a shear mode sensor and a longitudinal mode actuator with the same piezoelectric layer. As these two modes additionally show different acoustic velocities, it would be even possible to realize sensor and actuator with the very same FBAR device.
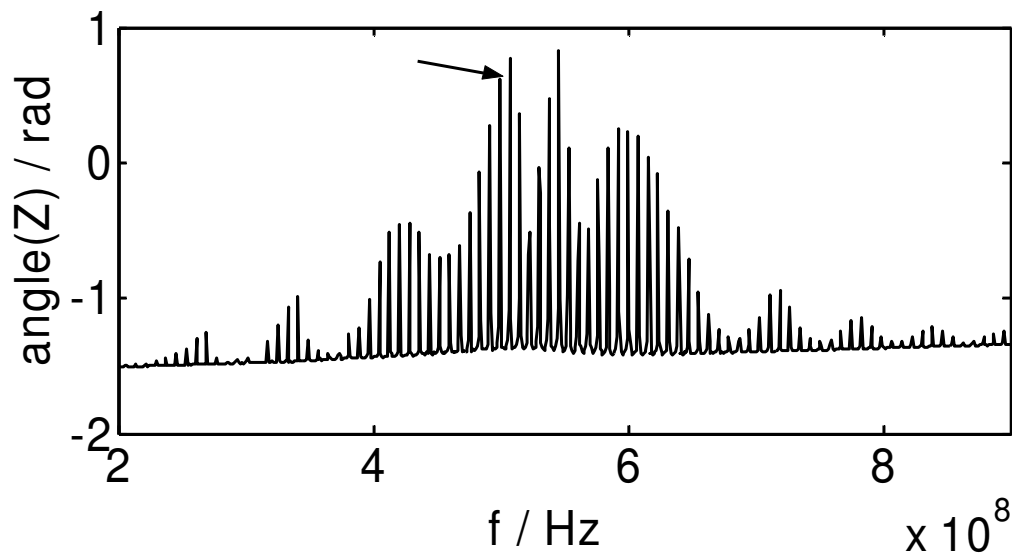
Figure 6.12: Impedance spectrum of the mirrorless resonator used for the agitation experiments: overmode resonances with a spacing of 7.5 MHz, corresponding to the thickness of the silicon substrate, are observed and a maximum is seen at 546 MHz. The arrow marks the resonances used for agitation.

To test this with the FBAR technology used in the frame of this work, an overmoded resonator was built. It has the advantage, that the mixing frequency can be chosen more freely as resonances occur in intervals given by the wafer thickness. It consisted of a Pt bottom electrode of about d = 500 nm and a top electrode of d = 100 nm thickness and a piezoelectric layer of ZnO with a thickness of approximately d = 4 μm. This thickness was chosen in order to be able to operate the device at lower frequencies. The impedance spectrum of the resonator is shown in figure 6.12. The overmode resonances have a spacing of about 7.5 MHz and can be identified as wafer resonances. They have a maximum at about 546 MHz. In order to maximize the energy that is fed into the device, the RF cables connecting the network analyzer to the FBAR were adjusted to match 50 Ω employing a stub

tuner. The frequency range of the network analyzer was now adjusted to a narrow band around the minimum of the reflection (S11 parameter).

a)
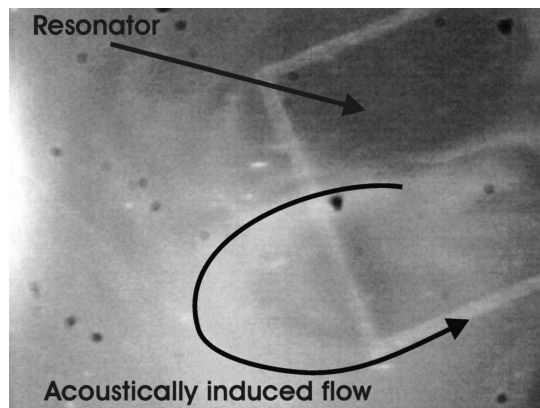
b)
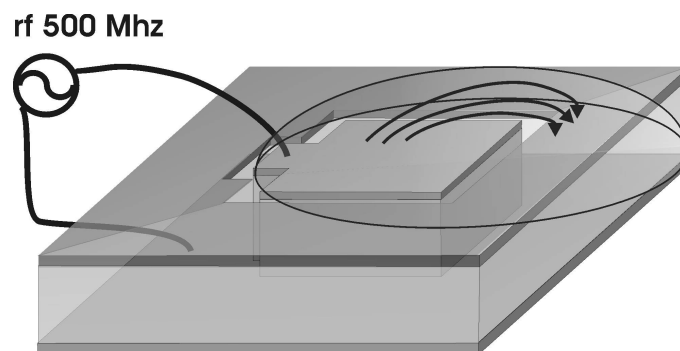
Figure 6.13: Schematic and photograph of the agitation (explanation see text).

In order to be able to observe a possible agitation, the ink of a green marker pen was extracted and a small drop placed on the resonator. A bigger drop of water was placed onto it and the resonator was switched on. A USB-camera was connected to the microscope and a movie was taken of the fluid motion. The resonator had a diameter of 500 μm.

The electric power of the network analyzer was varied between P = -25 and P = 10 dBm which is equivalent to P = 3.1 μW to P = 1 mW. A visible agitation could be observed starting at about P = -7 dBm or P = 0.2 mW. When a wider frequency range was chosen, the agitation appeared to be pulsed

with the sweeping period, giving evidence that agitation only takes place at acoustic resonance and that electric reasons for the fluid actuation can be ruled out.

One single frame of such a movie is shown in figure 6.13 a. The fluid motion always exhibits the same pattern. The fluid is moving away from the resonator in a very narrow stream that shows a laminar flow. The real cross section of this „flow channel" may not be as narrow as observed. The ink is composed of small particles that may be pulled into the region with the greatest velocity. Approaching the edge of the drop, the flow becomes slower. It flows back left and right of the central flow channel in a characteristic kidney pattern.

Different reasons may be responsible for the rather narrow flow channel. On the one hand the half space form of the drop and the resonator being located near the edge of the drop as shown in the schematic in figure 6.13 b may lead to destructive interference of the acoustic energy due to the reflection from the drop edges. Vivek et al [VIV00] made use of such interference effects to focus the fluid stream with the help of specially patterned resonators.

Another reason may be an additional focusing by the fluid that is flowing back. Knight et al. [KNI98] showed for instance that it is possible to focus the fluid flow with the help of two fluid streams coming from the sides.

7.   Biosensing Applications

In this chapter, the application of the FBAR as a biosensor will be tested. After an introduction of the sensing principle, an expression for the "biological sensitivity" will be derived. This is necessary because in biosensing applications, quantities other than the mass attachment will become relevant, most notably the concentration of an analyte in solution. Therefore, we will derive a connection between the "physical sensitivity" describing the frequency shift per unit mass attachment and the "biological sensitivity" which is referring to the concentration of analyte.

In the following sections, different biosensing applications will be discussed. First (section 7.3) an antibody-antigen-system will be tested. This is a well known system and is therefore suited to test the biosensor performance, as its binding behaviour and the mass attachments can be controlled quite easily. The measurements will especially be compared to measurements with a QCM-device operating at a frequency that is two orders of magnitude below the one of the FBAR-device.

In section 7.4, the binding behaviour of lipid vesicles will be investigated. The elasticity of these vesicles can be manipulated and result in very different measuring dynamics. In section 7.5, the formation of S-layers on the sensor surface will be monitored and series of measurements are carried out to investigate the influence of the concentration of the analyte on the measurement dynamics. Finally, layers of carbon nanotubes are deposited on the sensor and will provide a model for a two layer system where the frequency shift is heavily influenced by the elastic properties of the overlayer.

7.1 Sensing Principle

In a biosensor, two steps are required in order to obtain an analyzable result. They are illustrated in figure 7.1. In first place, there will be a biochemical reaction. The biofunctionalization involved in that reaction enables a measurand to be generated. In the case of the FBAR, this measurand is a mass load. In the second step, a transducer will convert the measurand into a measurable signal, which is an electrical signal in most of the cases, but sometimes it may have other forms like for instance an optical signal (which again may be converted into an electrical signal).

Two principles act in conjunction to enable this form of measurement and in particular the ability of the sensor to act as a biosensor: the first is selectivity and the second sensitivity. Selectivity implies that the sensor is responding to certain molecules or a certain class of molecules only. In particular,

these should be the molecules of interest for the desired sensing application. The instrument for achieving selectivity is the biofunctionalization. According to key-lock principles, selectivity is enabled. For the case of the FBAR, this is schematically shown in figure 7.2. For a single biofunctionalization to be perfectly selective, a minimum complexity of the molecules involved in the reaction will be required. Vice versa it will be difficult, for instance, if not impossible, to find a functionalization that is perfectly selective for a gas molecule such as carbon monoxide.
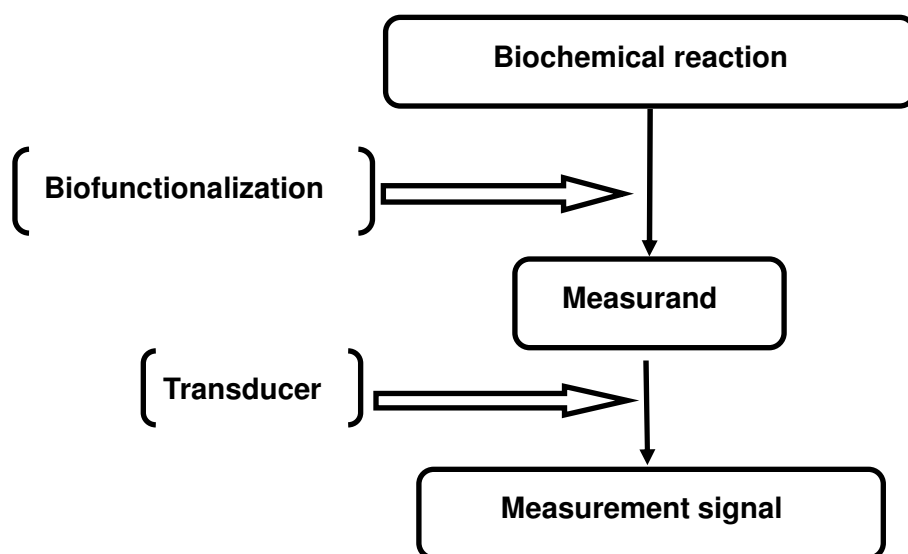
Figure 7.1: General underlying principle of a biosensor measurement: a biochemical reaction leads to the change of a measurand by virtue of a biofunctionalization. With a transducer this measurand can be read out which means converting the measurand into an electrical signal.

Nevertheless, there exists another method to increase the selectivity of the device. By combining many sensors with different functionalizations, the selectivity can be (at least theoretically) dramatically increased. An exemplary calculation demonstrates this. Let P be the probability of the sensor to respond to a "wrong" substance. One may now assume that there exist a number of different functionalizations N, each of them responding on the desired substance but responding on other substances as well. Let further be the probability to fail the same for all biofunctionalizations. If every biofunctionalization is responding to different false substances, and these substances are random (not necessarily disjunctive, if they were, two sensors would already suffice to obtain perfect selectivity), then the probability for the combination of N sensors to fail can be written as:

$$P(N) = P^N \qquad\qquad \text{eq. 7.1.}$$

Assuming for instance a probability of failure of 70% and an array of 16 sensors, the combined failure probability would reduce to 0.3%.
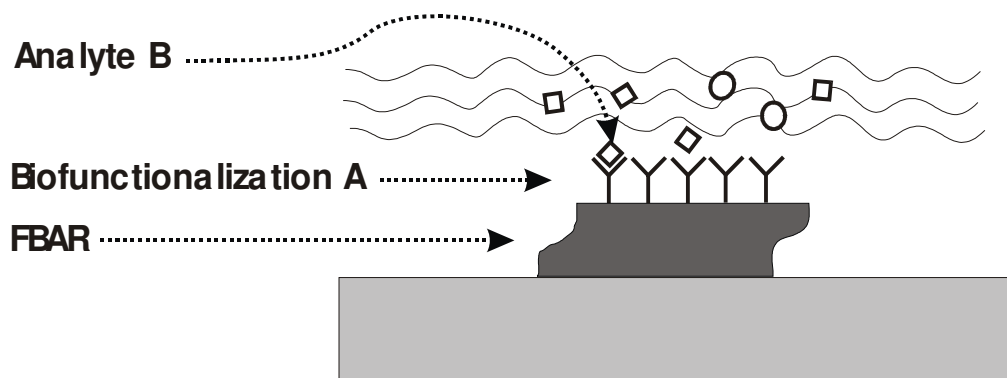
Figure 7.2: FBAR with biofunctionalization and analyte (see derivation in text).

Sensitivity is implemented by both functional elements, the biofunctionalization as well as the transducer. The biofunctionalization is acting on sensitivity by virtue of the reaction energy and the corresponding reaction speed. This may be also referred to as the chemical sensitivity of the sensor. The transducers' sensitivity, on the other hand, is given by the frequency response to a certain mass loading. This has been discussed in detail in chapter 4 and also chapter 3. In the next section the interrelation between both sensitivities will be discussed.

7.2 Influence of the Biofunctionalization on Sensitivity

The sensitivities given in chapter 4 provide a measure of the sensor response on a certain mass attachment. Someone dealing with a biological system, however, is mostly interested in the sensitivity depending on the concentration of an analyte in the fluid. To assess this, a system as shown in figure 7.2 will be considered. The biofunctionalization A is assumed to be rigidly bound to the sensor surface and is given by a constant number of molecules N[A]. The fluid is containing the analyte B which has a concentration of C[B] given in numbers of molecules per unit volume. The fluid is now

assumed to be flowing over the sensor with a constant flow. Therefore, as the fluid volume facing the sensor surface is changing constantly, the concentration of the analyte of the fluid volume in contact with the sensor is assumed to be constant. This includes that the reduction of the concentration of the analyte per time is negligible within the time frame in which the fluid volume is facing the sensor.

The probability of a reaction taking place between a certain given functionalization molecule A and the molecules of the analyte B is proportional to their concentration C[B]:

$$P_{A+B} = k_{A+B} \cdot C[B] \qquad \text{eq. 7.2}$$

with k_{A+B} the reaction constant of the reaction A + B → AB and the probability P_{A+B} giving the reaction probability per time. The reverse direction of the reaction AB → A + B is independent on concentration and has a probability $P_{AB}=k_{AB}$.

The reaction leads to a reduction of free molecules on the sensor surface and to an increase of the number of AB-complexes, which can be written as:

$$N[AB] = N_{\infty}[AB] \cdot \left(1 - e^{-(P_{A+B}-P_{AB}) \cdot t}\right) \qquad \text{eq. 7.3.}$$

The mass density can be written accordantly:

$$\frac{\Delta m}{A} = \frac{\Delta m_{max}}{A} \left(1 - e^{-(k_{A+B}C[A]-k_{AB})t}\right) \qquad \text{eq. 7.4}$$

with $\Delta m_{max}/A$ the mass density of of analyte, when all the target molecules on the sensor surface are occupied. Now recall the definition of mass sensitivity $s_m = \frac{\Delta f}{\Delta m / A}$ (chapter 4). The expected frequency shift can then be expressed in terms of the concentration of analyte and time:

$$\Delta f\left(t, C[A]\right) = s_m \frac{\Delta m_{\max}}{A}\left(1 - e^{-(k_{A+B}C[A]-k_{AB})t}\right)$$ eq. 7.5.

An exact detection limit can not be formulated in the same way as the mass detection limit (equation 4.3). But one can regard different cases: if in the first case the reaction is assumed to proceeded until the saturation is reached, the attached mass will be detected, when it is bigger than the minimum by the sensor detectable mass. Furthermore, the forward direction of the reaction has to be quicker than the reverse direction, namely:

$$C[A] > \frac{k_{AB}}{k_{A+B}}$$ eq. 7.6.

So this gives the minimum concentration of analyte in solution required that a binding to the sensor surface takes place.

In the other case, the reaction is assumed to run only for a certain time. As a detection limit, the required minimum time $t_{\min}$ for the reaction until the minimum mass attachment is reached, can be formulated:

$$t_{\min} = \frac{\ln\left[1 - \frac{\Delta f_{\min}/s_m}{\Delta m_{\max}/A}\right]}{-k_{A+B}C[A] + k_{AB}}$$ eq. 7.7,

where $\Delta f_{\min}$ is the frequency resolution of the sensor and is given by equation 4.2. In the case that the reaction is running only for a very short time as compared to the saturation time (meaning that the sensor response in the saturation case is much larger than the sensor resolution) the approximation $\ln x = x$ can be made, so equation 7.7 becomes:

$$t_{min} = \frac{\dfrac{\Delta f_{min}/s_m}{\Delta m_{max}/A}}{k_{A+B}C[A] - k_{AB}} \qquad\qquad \text{eq. 7.8.}$$

In many cases the backward reaction can be neglected so k_{AB} may be omitted in equation 7.7 and 7.8 respectively.

7.3 Measurement with an Avidin-Antiavidin Model System

Experiment

To test the sensor and assess its performance under practical conditions, measurements with an avidin-antiavidin system were carried out. The use of QCM as an immuno specific sensor is well known and has already been described by Shons et al. in 1972 [SHO72]. Time dependent measurements of such systems were for instance carried out by Thompson et al. [THO87]. Both systems, the FBAR operating in shear mode as well as the one operating in longitudinal mode, were used. Additionally, comparison measurements with a QCM system operating at 10 MHz were carried out at VTT Information Technology[6]. Furthermore, the mass of the of the layers was determined by reference measurements using surface plasmon resonance (Biacore 3000).

The measurements were all carried out on wafer. A flow cell was positioned on the wafer as shown in figure 7.3. It is composed of a chamber made from acrylic glass with an inflow and outflow that can be connected to a fluidic system. Sealing was ensured by a viton strip. The sensor, which is manufactured by surface micromachining only, has connections with 750 μm length. The flow cell has a wall thickness of 500 μm, so it can be applied while ensuring that the sensor is fully immersed in the liquid and the contact pads are located outside the flow cell, where they can be electrically contacted.

---

[6] Measurements carried out by Willem M. Albers, Jussipekka Tuppurainen

TO FLUIDIC SYSTEM   Flow cell

Inlet   Outlet

FBAR   Leads   RF Probes   TO NETWORK ANALYZER
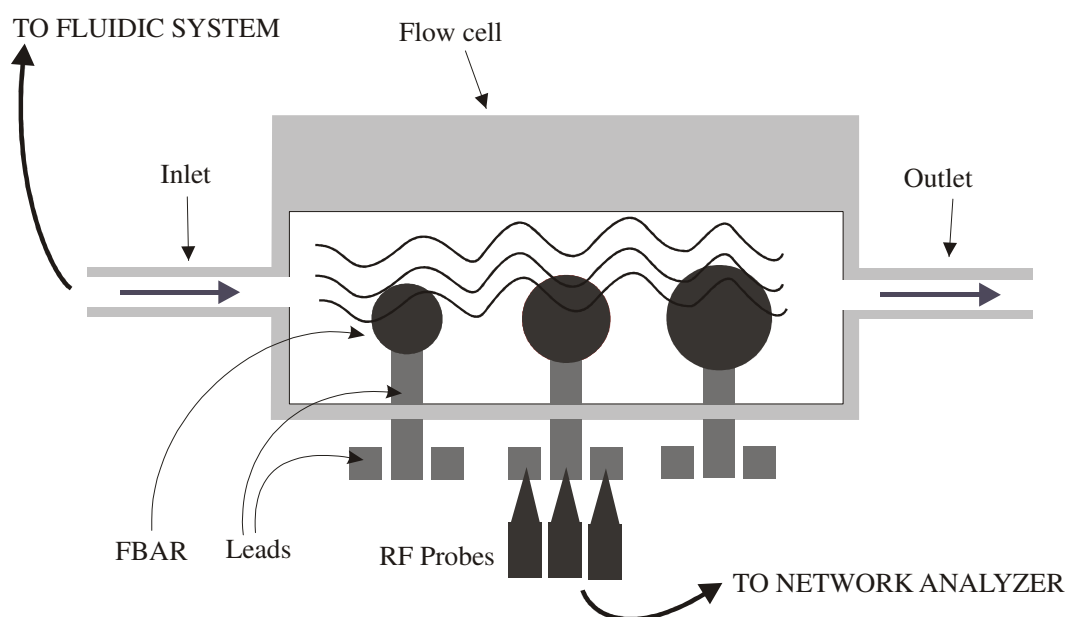
Figure 7.3: On-Wafer measuring setup: flow cell with connections to the fluid system is placed on the wafer. The active resonator area is completely immersed in water, electrical readout is done outside the flow cell with an RF-tip.

Dynamical measurements were carried out recording the resonance characteristic every 14 seconds. The frequency sweeps covered a range of 30 MHz around the resonance with a 200 point resolution. The data obtained were read out by the computer and converted to impedance values. The resonance frequency was then calculated from the impedance phase. A sensor with circular shape and a diameter of 200 µm was selected.

The measurement procedure is shown schematically in figure 7.4. A buffer fluid[7] was used to stabilize the sensor and especially the reagents. On the other hand, it served as a reference fluid, ensuring that the complex sensor-coating always "sees" the same fluid with the same viscosity. Hencem, the sensor response between two buffer solutions is mainly due to the additional layer and not further influenced by the liquid medium.

---

[7] „HBS buffer" 150 mM NaCl and 10 mM HEPES at a pH of 7.46

Figure 7.4: Schematic proceeding in the measurements of the avidin-antiavidin system: during injections of ca. 7 minutes the solution with the respective analyte was flushed over the sensor, a) the first layer of avidin, b) rinsing with buffer 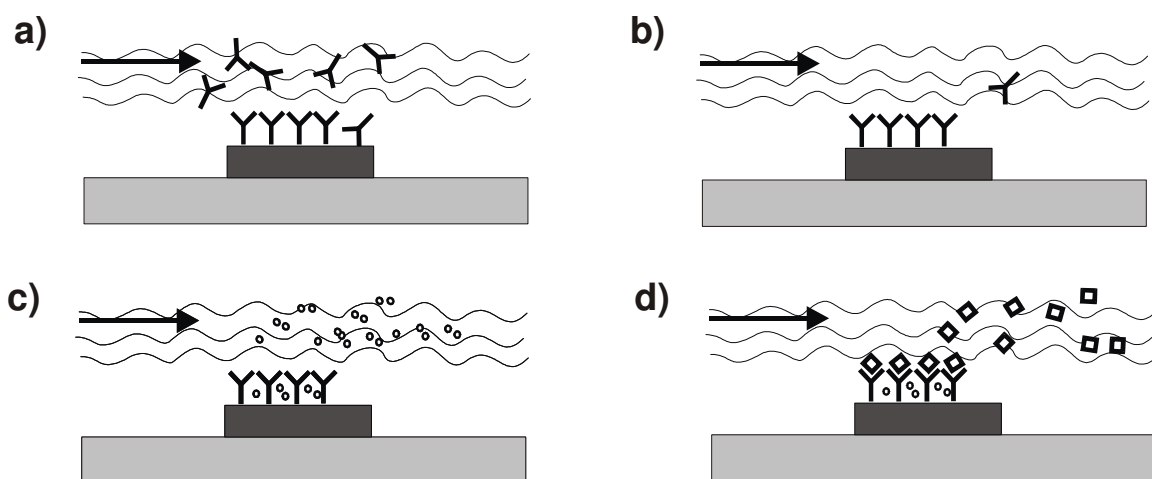solution in order to remove unspecific bindings (this step was repeated after every binding step), c) bovine serum albumin with the task to fill up the spaces between the avidin molecules and thus block any unspecific bindings in the next steps and d) antiavidin.

With this method (also shown schematically in figure 7.4), a system comprising the biofunctionalization and the analyte is built up on the sensor gold surface during one experiment. The injections with the analyte had a duration of about 7 minutes and a volume of 200 µl, respectively. The flow rate was stabilized at 36 µl/min throughout the entire measurement. After the first avidin injection, bovine serum albumin (BSA) was added. This is a comparably small molecule and serves for filling up the spaces between the avidin molecules thus preventing any unspecific binding to the gold surface in the following step. The speed at which the fluid is moving over the sensor surface was estimated to about 0.5 mm / s meaning that the time a certain molecule is staying over the sensor is about 0.4 s.

Dynamical Investigations

Before starting the dynamic measurements, all sensors, that were submitted to the biological processing, were characterized in dry state. After the measurements have been completed, the wafer was rinsed with water, dried, and comparison measurements were carried out. They yielded a medium frequency shift of 730 MHz which is quite close to the result obtained in liquid. The standard devia-

tion for these frequency shifts was only about 24 MHz, meaning that the measurement setup allows a quite homogenous coverage of all the sensors. The quality factor was reduced by about 17%.
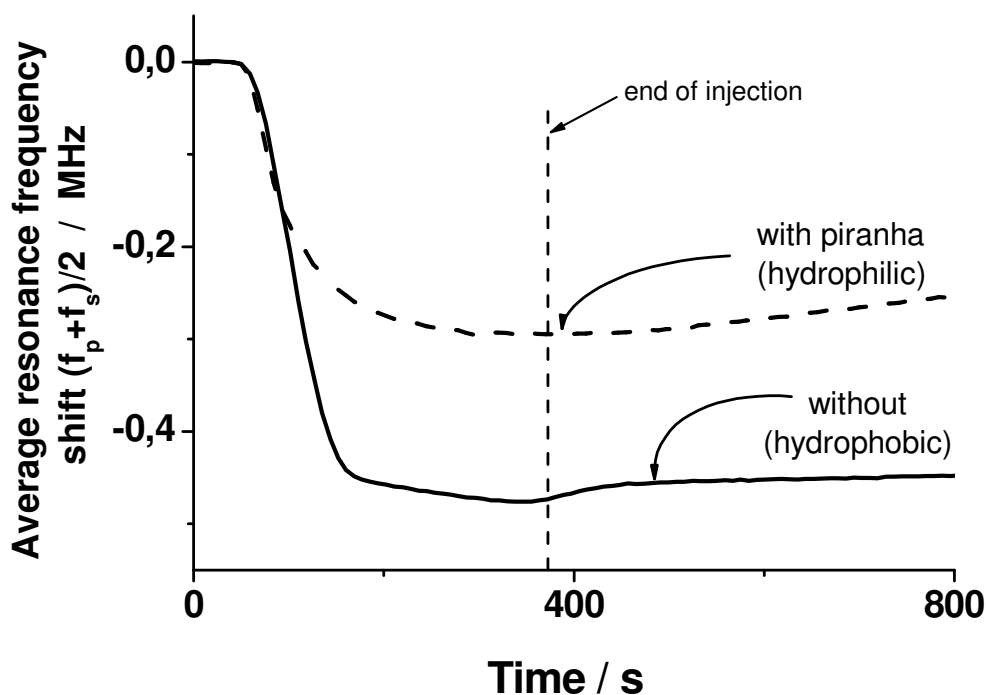
Figure 7.5: Observation of the binding of avidin with a more hydrophilic (treated with piranha solution) and a more hydrophobic surface.

A dynamic measurement of the binding of the first layer is shown in figure 7.5. The surface of the sensor was submitted to different surface pre-treatments: in one case it was treated with a piranha solution (30% H_2O_2 and 70% H_2SO_4) whereas in the other case it was not. Through the pre-treatment with piranha the surface is supposed to obtain a more hydrophilic character. The measurements show quite different characteristics: in the hydrophobic case the binding is much faster and the overall frequency shift is greater.

Interpretation for this is to be found in the different binding abilities. In the hydrophobic case, the gold surface has a greater affinity to the avidin. This also becomes clear when the sensor is flushed with buffer solution after the injection: in the hydrophilic case the frequency rises again meaning

that the avidin molecules are ripped off the surface. In the hydrophobic case, the frequency looks more stable.
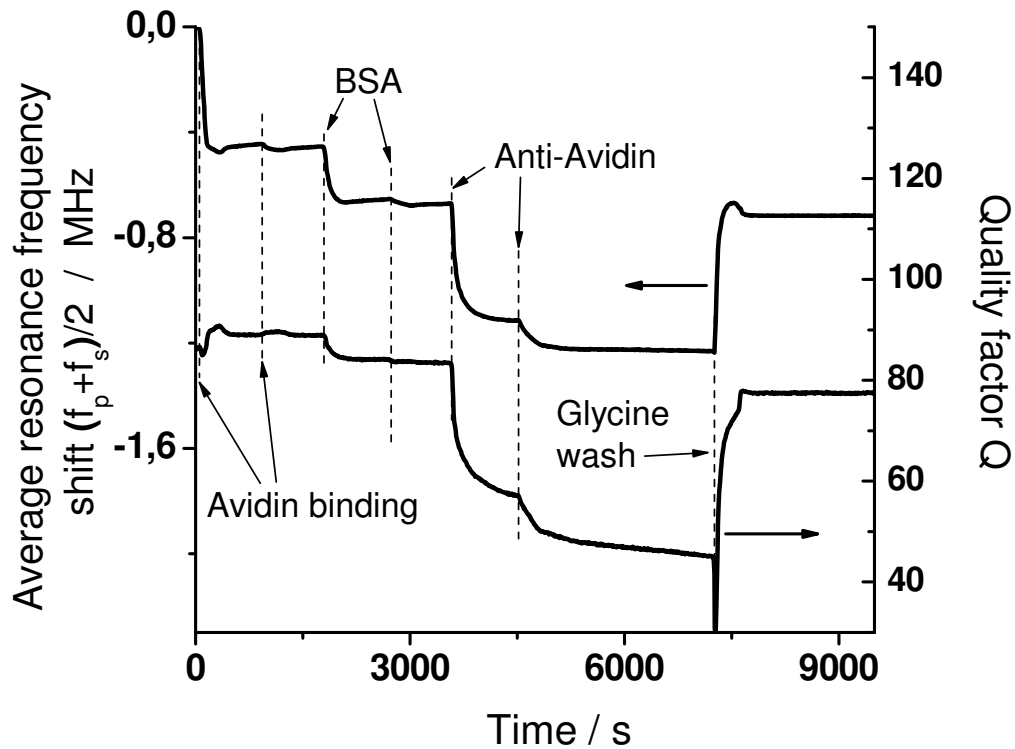
Figure 7.6: Complete time evolution of the binding processes involving avidin, bovine serum albumin and anti-avidin. In the upper curve, the frequency shift is shown, giving information about the mass attached, in the lower graph the quality factor is shown.

Moreover, in the hydrophobic case a two-stage process is observed. Obviously, after complete coverage of the surface a second layer of avidin molecules is forming. These molecules are bound unspecifically to the first layer and are removed during the washing step.

Biosensor Performance

One aim for the experiments with a biological system is to obtain values for the performance of the sensor operating under practical conditions. In chapter 4, expressions for the sensor performance were derived the figures of merit such as the quality factor and sensitivity were determined. Apart

from these figures, the minimum detectable mass furthermore depends on the minimum frequency that can be resolved by the respective evaluation circuit. This could be seen from equation 4.3.

Nevertheless, a figure of merit can be defined, which under the condition of a constant frequency resolution is principally proportional to the minimum detectable mass:

$$FOM = Q \cdot s \qquad \text{eq. 7.9.}$$

This figure was calculated for the different sensors used in the experiments. The sensitivities for the FBAR were determined from the one dimensional modelling described in chapter 3. For the quartz crystal microbalance, the sensitivity was determined from the simple Sauerbrey relation. The sensitivity of the FBAR therefore turns out to be approximately 800 Hz/(ng/cm²) which is more than three orders of magnitude higher than the sensitivity of the 10 MHz quartz crystal Microbalances (0.22 Hz/ (ng/cm²)). These results are shown in table 7.1.

All in all, the values show that the shear mode FBAR performance is expected to be superior to that of the QCM. The (mass resolution equivalent) figure of merit is about 6500 to 9900 and more than two times better than that of the QCM (22730). The much lower Q-factor of the FBAR is more than compensated by the higher sensitivity coming from the higher operation frequency. The expected performance of the longitudinal mode FBAR on the other hand is about 10 times worse, which is mainly due to the much lower Q.

Furthermore, it should be noticed that the influence of the immersion in liquid is different for the QCM and the FBAR sensor, respectively. Consider the Q-factor, which for the FBAR is about 150 in water compared to about 300 in air. So the quality factor is reduced to half its original value due to immersion into water, which means that the acoustic energy loss due to dissipation into water is doubling relative to the acoustic loss within the resonator alone. For a quartz crystal microbalance the reduction of the Q-factor is from 20000 to 2000 or by 90%, which means that the acoustic dissipation is increasing by a factor of 10. So the negative impact on sensor performance from immersion into liquid is much stronger for the QCM than for the FBAR, because the sensor performance is ruled by the product Q·s. Vice versa this means, that a QCM being superior to an FBAR in a gaseous environment may be worse in liquid.

*Table 7.1: Resonator performance in liquid: Taking the theoretical value for its sensitivity, the resonator figure of merit can be calculated for an approximate comparison of the different resonators mass resolution *Quartz sensitivity according to Sauerbrey*

	Longitudinal-mode-FBAR	**Shear-mode-FBAR**	Quartz-crystal-microbalance
Operation Frequency / MHz	2000	790	10
Simulated Sensitivity s (Hz·cm²/ng)	2500	800	0,22*
Q in liquid	10	100 - 150	2000
FOM Q·s (cm²/ng)	80000	6580 – 9880	22730

To summarize, it can be stated that when the frequency of the device is increased, a shift from low sensitivity and high Q to high sensitivity and low Q occurs, which increasingly favours the operation as a liquid sensor.

To assess the FBAR sensor performance in the biosensing application, the avidin binding was taken as a reference. Surface plasmon resonance measurements employing Biacore 3000 yielded a mass attachment of about 420 ng/cm² for this binding. With this value and the frequency shifts obtained for the binding in the experiment a value for the sensitivity of the different devices can be determined. They are summarized in table 7.2 (second line).

Furthermore, the noise was determined from stability measurements. It is influenced by a complicated set of factors. Influences deriving from the fluidic and the biological system are adding to the factors discussed in chapter 4. It could be observed that noise was decreasing throughout the experiment and was lowest at the end of the last of a set of measurements. This was despite the fact that three biolayers were attached to the sensor at that time. Hence, the noise coming from contamination inside the fluidic system seems to be playing an important role.

Table 7.2. (Bio-)Sensor performance of the different bulk acoustic wave devices, an FBAR operating in longitudinal mode, one operating in transverse shear mode and a quartz crystal microbalance. Note that the performance ruled by the detection limit is already better for the shear mode FBAR device than for the QCM.

	Longitudinal-mode-FBAR	**Shear-mode-FBAR**	Quartz-crystal-microbalance
Frequency / MHz	2000	**790**	10
Experimental sensitivity / Hz·cm²/ng*	937,5	**585**	0,54
Measured noise level / Hz	15400	**864**	1
Minimum detectable mass / ng/cm² **	21	**2,3**	5,2

* the frequency shift evoked by the avidin-binding was taken as a reference ** the mass was determined with the threefold frequency noise as frequency resolution

To determine the noise, 50 measurements of the resonance characteristic were taken over a time range of about 700 s while the rest of the system was held stable. The standard deviation of these values yielded a noise of about 864 Hz for the shear mode FBAR as compared to 15400 Hz for the longitudinal mode FBAR, and only 1 Hz for the QCM. The threefold of the standard deviation was regarded as the minimum detectable frequency shift. For the shear mode FBAR, a drastic improvement due to the much lower energy dissipation in water compared to the longitudinal mode FBAR is obtained.

In consequence, a sensitivity of 585 Hz·cm²/ng and a mass detection limit of about 2.3 ng/cm² was derived. In the same way, data were obtained for the longitudinal mode FBAR and QCM and are summarized in table 7.2. This table thus provides a direct comparison of the performance of the different sensor systems under practical conditions.

According to this assessment, the shear-mode FBAR biosensor performs twice as good as the conventional QCM-system. Although the noise level of the device is much higher than for QCM (864 Hz compared to 1 Hz), a better mass resolution is achieved because of the superior mass sensitivity.

The performance obtained with a longitudinal mode FBAR is quite poor, as expected. The results for the relative performance of FBAR and QCM agree reasonably with the semi-theoretical considerations that are summarized in table 7.1. That is, the mass resolution as obtained from the biosensing experiments corresponds to the figure of merit as obtained from the sensor performance in liquid. Nevertheless, there is a difference between the theoretical and the experimental sensitivity. The experimental sensitivity for QCM is higher whereas for the FBAR it is lower than the respective theoretical values. Here, side effects deriving from top-layer elastic properties and with frequency dependent impact on sensor sensitivity may play a role.
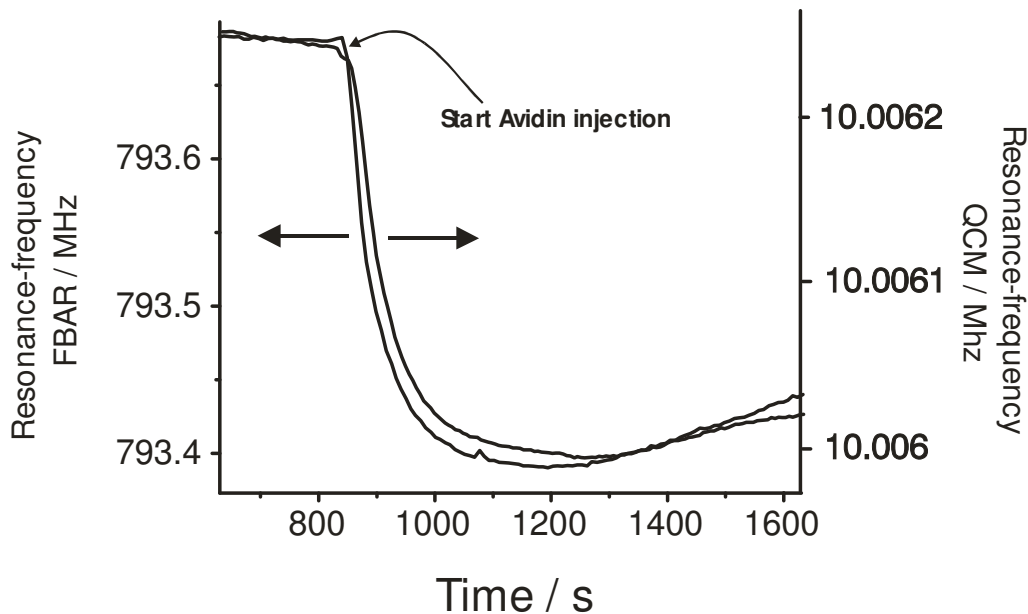
Figure 7.7: Comparison between avidin binding measured with QCM-System and FBAR: the same qualitative characteristics are observed, events with a high curvature seem to be better resolved by the FBAR (see arrow).

Figure 7.7 shows a plot of the resonance frequency taken dynamically for the avidin-binding. The surface of the FBAR-sensor was subjected to a pre-treatment with a piranha solution. One curve shows the binding process as it was seen with the shear mode FBAR whereas the other curve shows the result obtained with a conventional QCM. It clearly shows that the result obtained from both devices is qualitatively the same. A sharp decrease in resonance frequency is observed when avidin is flushed over the resonator, the rate of the adsorption yet declining throughout the process. The adsorption is lasting for 350 and 420 seconds for the FBAR and QCM, respectively, before a slight

increase of the resonance frequency begins. This time coincides with the duration of the avidin-injection, so the increase can be attributed to a detachment of loosely bound avidin molecules. The maximum reaction rate could be determined to 2.9 Hz/s or 5.4 ng/cm²s for QCM and 4.4 kHz/s or 7.6 ng/cm²s for the FBAR. The agreement of all qualitative features observed shows that although the devices are operating at very different frequencies (the FBAR operation frequency is 80 times higher than that of QCM), the same binding processes are observed in the same way. Both curves continue to rise slowly and with nearly constant speed until the next injection.

7.4 Measurements with Cell Membranes

In this section, the binding of lipid vesicles onto the FBAR surface will be described. Vesicles are the smallest compartment existing in cell biology. They consist of a single bilayer of lipids. Lipids are made up of a long chain of fatty acids forming the hydrophobic "tail" and a hydrophilic "head", which in most cases consists of a phosphoric acid. In water, these lipids form vesicles, which consist of bilayers that are bent to form a sphere. The hydrophilic parts are pointing outwards and inwards, thus shielding the hydrophobic parts from the water. This is shown schematically in figure 7.9 a.

Lipid bilayers exist in different forms and they can be classified by their head group and by the length and the degree of saturation of the tail. The tails are composed of two identical chains. The vesicles used in the experiments have the same head group, but the tails have a chain length of 18 and 16, respectively. The longer one additionally contains one unsaturated bond. The lipids are classified by four letter accronyms, the first two describing the chain and the last two describing the head group. The head group's accronym is PC (sn-Glycero-3-Phosphoholine) and the tails are designated with DO (= Dioleoyl) for the longer one and DM (= Dimyristoyl) for the shorter one [STE05].

Depending on the conditions of the environment, such as temperature, pressure or the pH, the lipids can adopt different phases featured by different physical properties. The most important phases are thereby the liquid condensed (LC) and the liquid expanded (LE) phase, the former appearing at low temperatures and the latter at higher temperatures. They differ in both geometry and density. The phase transition between the LC and the LE-phase happens at T = -20 °C for DOPC and at T = 41°C for DPPC. At the phase transition the lipids display an increased thermal capacity and compressibility. So at room temperature DOPC is in liquid expanded phase and DPPC in liquid condensed phase.
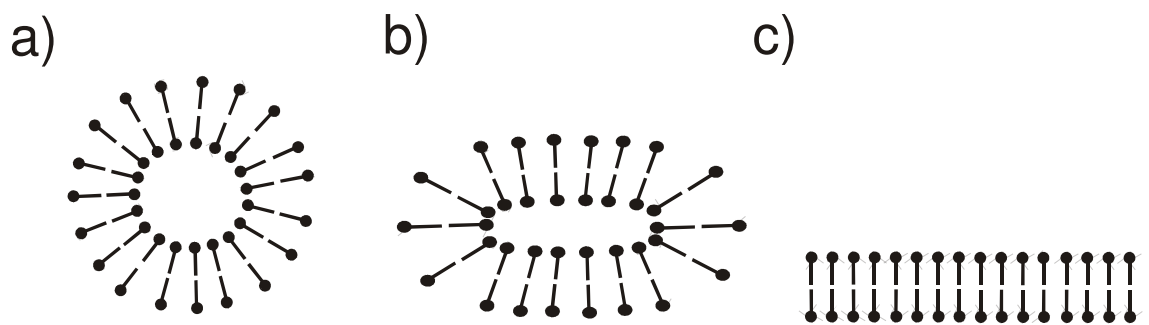
Figure 7.9: Vesicles and their binding mechanism to the surface. (a) They are made up of a lipid bilayer with the hydrophilic parts pointing inwards and outwards. The size of the vesicle depends on the bending energy. b) Adsorption is followed by a deformation of the vesicle due to the adhesion energy and after that a bursting with the formation of a bilayer (c).

To allow for vesicle adsorption onto the resonator surface, a thin SiO_2-layer of about 20 nm was processed onto the gold electrode by chemical vapour deposition. For the measurements, the open flow cell was used and the vesicle solution was directly pipetted into the flow cell. This setup was identical to the one described in chapter 6.4. Before the measurement started, a preliminary cleaning of the wafer was carried out. It consisted of a rinsing with isopropanol for half a minute and then a bath in a detergent solution (5% mucasol in water). After that, the measurement system was attached and the measurement was started. The vesicle solution was filled into the flow cell and the frequency was observed over time. Also the temperature was monitored by employing a resistor in the vicinity of the resonator.

Binding above phase transition

In a first experiment, DOPC was used. The measurement temperature was about T=25°C, so the vesicles are supposed to be in LE-phase. The measurement (dots in figure 7.10) shows a rapid decay of resonance frequency with a high speed at the beginning and switching over to a process with a lower velocity. A binding process is taking place that is fast in the beginning and slowing down with the reduction of the free positions on the sensor.

An exponential fit, whether first or second order, does not match the time dependent behaviour very well. Especially, there is a relatively fast decline at the beginning (the exponential fit for this part yields a decay time of only 30 s). After that a slow part follows. This was also fitted with an exponential function and yielded a decay time of 226 s. The fact, that both parts can be fitted separately but not the whole measurement in one single function is an indication, that the two respective proc-

esses can not proceed in parallel. A fast reaction or a reaction with a great reaction constant k however is an indication for a strong binding. So for the fast part, the binding of the vesicles and a formation of a bilayer will be responsible. For the slow part a loose association of the vesicles to the surface can be assumed. When an association is taking place in the beginning, it will be followed by a bursting of the vesicles and a consecutive bilayer formation. This is the reason, why these two processes can not take place at the same time. Also the quality factor is showing a slow drift for the second process. This supports the assumption of a loose association, which induces a further damping due to a viscosity effect.
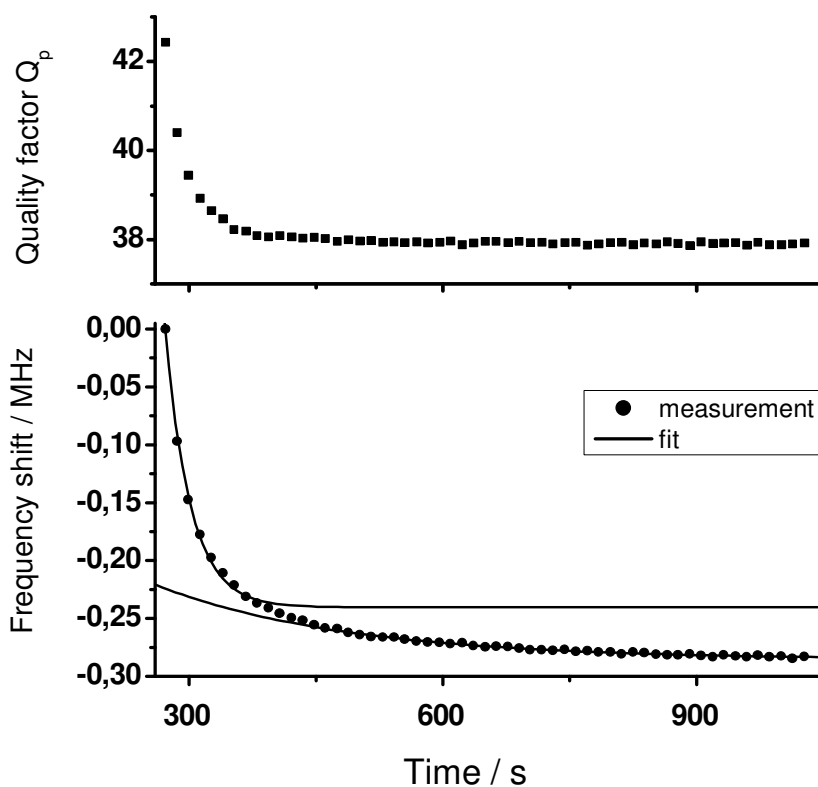
Figure 7.10: Measurement of the binding of DOPC. Two exponential processes can be spotted, a fast one with a reaction time of 30 s followed by a slow one with 226 s reaction time. The first can be interpreted as a particle association to the surface followed by a bilayer formation whereas the second is an association only. The processes can not be overlaid (no second order) leading to the conclusion that both processes are interfering.

The frequency shift is about $\Delta f = 272$ kHz and with a mass sensitivity $s = 800$ kHz·cm²/ng a mass attachment of about $\Delta m/\Delta A = 340$ ng/cm² can be obtained. With a molecular weight of 768 kDa this corresponds to a population density of $2.67 \cdot 10^{14}$ molecules per cm^2 or an area of $A = 37$ Å^2 per molecule. The quality factor of the resonator with DOPC is declining from 42.4 to 38.

Manipulating the phase transition point by doping

In the following measurements, the binding of DOPC which was doped with 1% cholesterol and the binding of DPPC was tested. The results are shown in figure 7.11. For the doped DOPC nearly no binding is observed at all (the frequency shift is only about 5 kHz) and also the quality factor (not shown in figure 7.11) stays almost constant. The temperature was then increased stepwise up to 52°C and decreased again to 25°C. Both the frequency shift and the quality factor end up at the same value after the temperature loop.
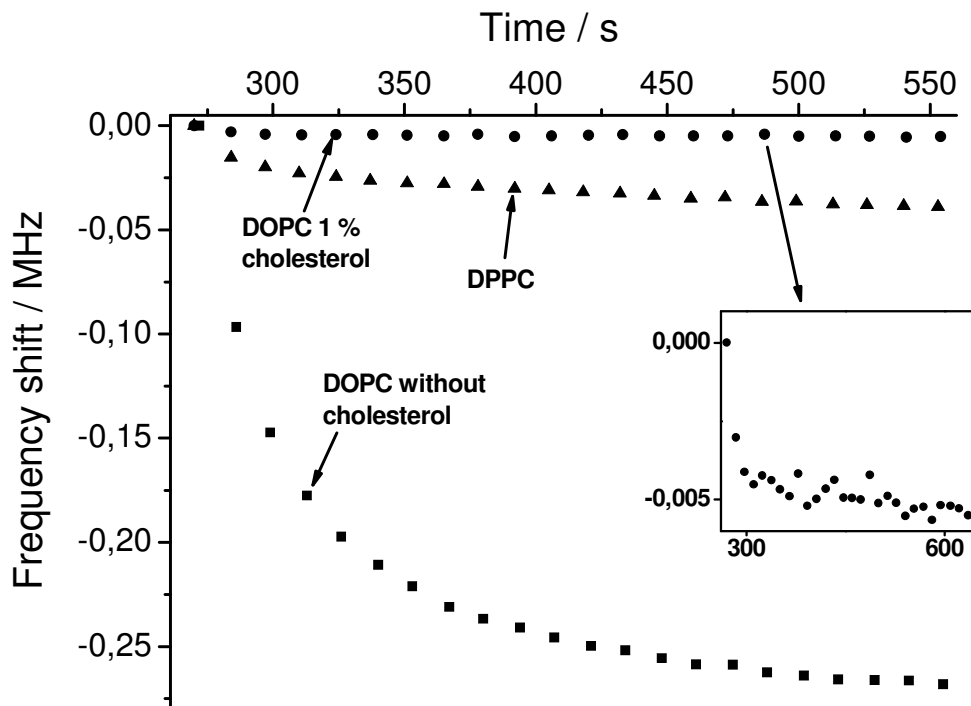
Figure 7.11: Frequency shifts obtained with DOPC, DPPC and DOPC doped with 1 % cholesterol. Because of the identical chemical composition of the head groups, the adhesion energy is the same for the different lipid vesicles. The difference in the magnitude of the binding is therefore due to the different elasticities and correspondent ability to flatten, in order to increase the contact with the sensor (step b in figure 7.9).
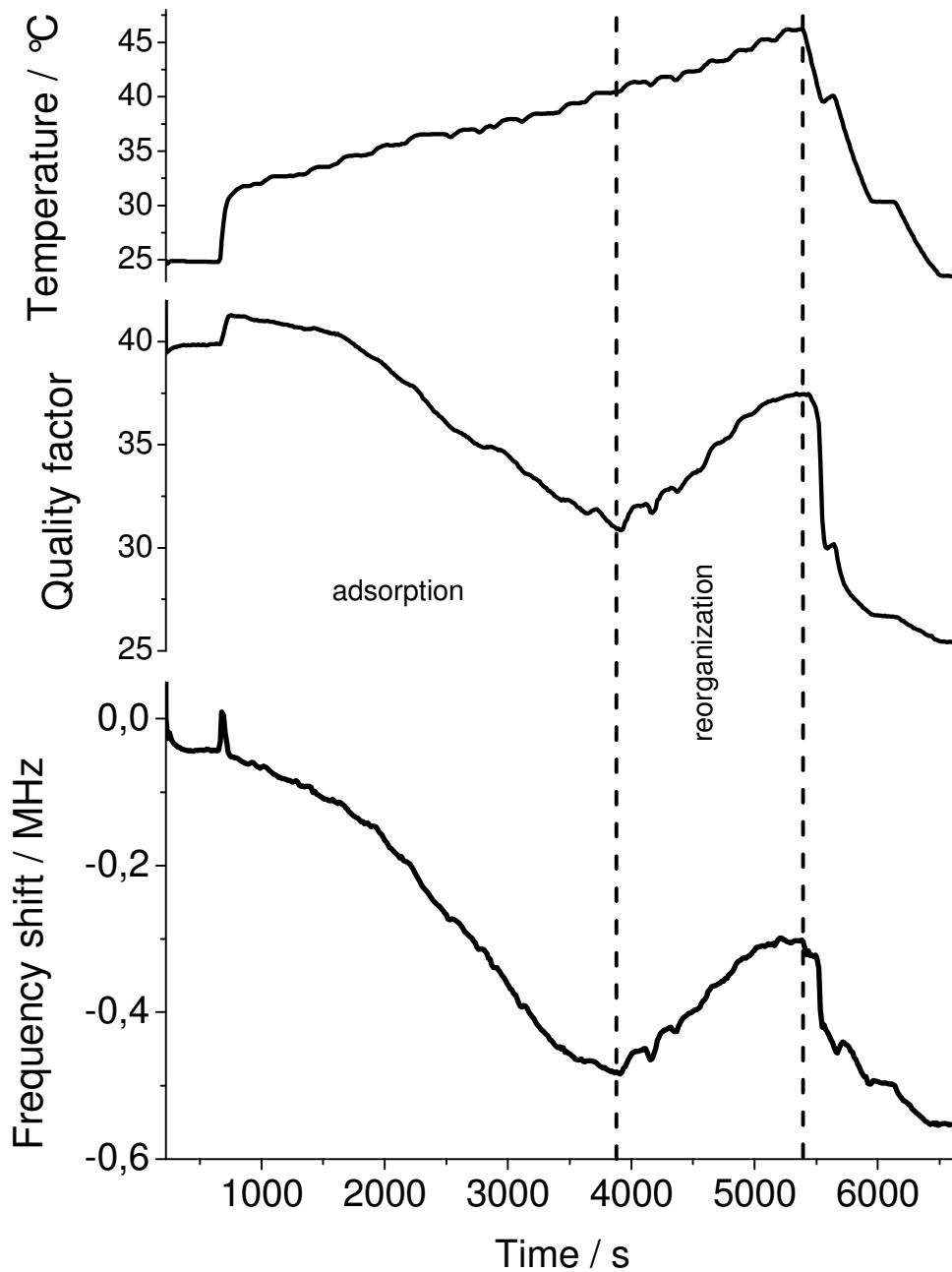
Figure 7.12: Binding of DPPC: By employing a temperature trigger an increased binding of the vesicles, which bind only very weakly at room temperature, is achieved. Both the frequency shift (below, corrected by the influence of temperature on the sensor and the viscosity of water) and the quality factor indicate a binding taking place in two stages: up to a temperature of 42°C the binding is accelerating with the increase of temperature. Above that temperature the vesicles burst and form a bilayer, which reduces the mass and the damping that were caused in part by the water trapped in the vesicles.

The binding chemistry of these vesicles is just the same as for the normal DOPC, so the reason that a binding is not observed for DOPC has to be searched in their topology. One interpretation is, that by doping the DOPC vesicles become stiffer and therefore have a fixed spherical topology. Their contact with the surface is limited to one point, which is why they can not react with the flat sensor surface.

Temperature triggering

To further investigate the mechanism of the binding of DPPC a temperature trigger was employed. As has been stated above, that DPPC has a phase transition at about 42 °C. Therefore, an experiment was carried out with the temperature being increased above that value. It was started at room temperature and the system was then heated up to a maximum of 47 °C before cooling down again to room temperature. The resonance was monitored throughout the whole measurement. In figure 7.12 the frequency shifts, the quality factor and the temperature are shown for this measurement. The temperature was measured with a resistor, being situated in the vicinity of the resonator. The measured resonance frequency was corrected by the temperature sensitivity of the FBAR (48 kHz / °C) and by the influence of the change in viscosity of water (see chapter 6). In the beginning the frequency shift is very low (36 kHz or 45 ng/cm²) and saturates after about 3 minutes. This was already shown in figure 7.11. It is about 8 times lower than for the DOPC binding.

After about 10 minutes, the temperature was increased to 32 °C. After about 200 s the temperature is stabilized at 32 °C. The frequency is observed to continue drifting at a rate of about 50 Hz/s. After that the temperature was increased in steps of 1 °C up to 47 °C, waiting for the temperature to stabilize at each step. The speed for the frequency shift is increasing further with temperature and is reaching a maximum of about 220 Hz/s.

At about 42 °C, the frequency shift stops and is moving in the reverse direction until the temperature is increased to about 45 °C. Interestingly, during this stage the attenuation is decreasing again. So possibly a rearrangement of the structure bound to the surface is taking place, reducing the mass that is bound and making the layer stiffer at the same time. The temperature is decreased in three steps back to its original value (25 °C). The frequency shift obtained from the frequency at the beginning and the end of the measurement (both at 25 °C) is about 527 kHz. This is considerably more than in the experiment with DPPC (272 kHz).

To further illustrate the phase transition, the frequency change over temperature is shown in figure 7.13. The direction of the temperature sweep is indicated by arrows. The frequency change above about 39.5 °C is almost independent of the direction of temperature change (up or down) whereas

below that temperature the curves are different. The interpretation is that at 39.5°C the properties of the layer change into a new phase. Above that temperature, they stay in this phase and the frequency shift is reversible. Decreasing the temperature below 39.5 °C, the layer stays in the same phase and so the frequency shift is different compared to the branch where the temperature was increased.
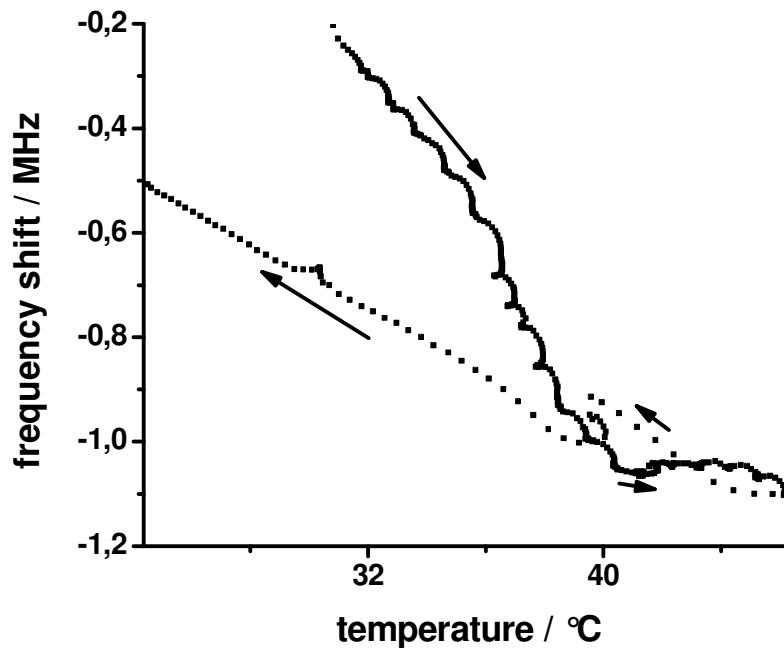
Figure 7.13: Change of resonance frequency with temperature. The direction of the temperature sweep is indicated by the arrows. A hysteresis can be seen, allowing the identification of the phase transition temperature (about 39°C). Above that temperature, the frequency shift is nearly independent of temperature, below that temperature it is different before and after temperature stimulus.

When time as a stimulating factor in the binding process can be neglected, meaning that the binding process is in equilibrium at any time (quasi static so to say) this plot serves to identify the phase transition temperature of the layer. It is furthermore seen in the f/T-plot that when the temperature is decreased, the frequency shift is linear and quite smooth, whereas in the branch where temperature was increased, the shift is not linear and also shows some irregularities. This is an indication that with increasing of the temperature a complex process of adhesion and binding takes place, with the vesicles bouncing on and off the surface, whereas in the decreasing branch the reaction with the

sensor surface is terminated and the temperature just induces changes in the properties of the over-layer and the fluid.

Another experiment was carried through with the temperature being increased from 25°C to only 42°C and back again. Interestingly, in that experiment an overall frequency shift of as much as 834 kHz was obtained corresponding to a mass attachment of 1000 ng/cm². This may be due to the fact, that a temperature increase to 42 °C is not sufficient for a complete bursting of the vesicles.

7.5 S-Layer

In this section reaction dynamics will be examined more in detail. It was said before, that the sensor can only detect a mass attachment and a damping. So one could think, that it is impossible to distinguish between different reagents binding to the surface. And it is true that a surface without any biofunctionalization is not specific to any reagent. However, when it comes to dynamic measurements, further information may be extracted regarding the reagents.

To investigate the impact of measurement dynamics, measurements with different concentrations of analyte were carried out. As a model reaction the deposition of S-layers on a gold surface was examined[8]. S-layers are composed of protein monomers that are contained in the outer cell membrane of certain bacteria. They can be arranged on a gold surface by self assembling to form a lattice structure of hexagonals or squares.

In the experiment, solutions with different concentrations of monomers were added to the sensor. After that, a solution with $MgCl_2$ was added, serving as a promoter to activate the reaction. A single monomer of the type Bacillus sphaericus NCTC has a molecular weight of about 111.5 kDa and the substructure of four monomers in a lattice has a lateral extent of about 13 nm. Hence, with the sensor fully covered, a mass attachment of 438 ng/cm^2 is expected.

Monomer solutions with concentrations of c=1.3, 3, 6.5 and 13 mg/ml were used and the binding was observed dynamically over a time of several hours. The amount of fluid injected into the flow cell was V=100 μl respectively. The maximum frequency shift measured was about Δf=214 kHz corresponding to a mass attachment of about Δm/ΔA=270 ng/cm². This is about 62 % the expected value. Assuming that the whole wafer inside the flow cell is covered (0.3 cm²), the monomers in

---

[8] S-layers were prepared and provided by Anja Blüher, TU Dresden

solution would be reduced by a mass of $\Delta m = 80$ ng. This is a considerable amount at least compared to the amount of monomers contained in the low concentrated solution, which is only 169 ng.

Table 7.3: Time constants and saturation values for the S-Layer reaction obtained from an exponential fit.

Time constant (s) → Concentration (mg/ml) ↓	t_1	t_2	t_3	k_{AB} (ml/mg·s)
1,3	806	4139	48510	$9.5 \cdot 10^{-4}$
3	671	4305		$5.0 \cdot 10^{-4}$
6.5	290	1149		$5.3 \cdot 10^{-4}$
13	213	1380		$3.6 \cdot 10^{-4}$
Saturation value (MHz) → Concentration (mg/ml) ↓	A_1	A_2	A_3	Sum
1,3	0.06065	0.05672	0.06331	0.18068
3	0.12548	0.06149		0.18697
6.5	0.10296	0.1178		0.22076
13	0.12588	0.0611		0.18698

The results for the dynamic measurements are summarized in figure 7.14, were the dots represent the measured frequency points. The measurements were then fitted to an exponential function:

$$\Delta f = y_0 + A_1 e^{-\frac{x}{t1}} + A_2 e^{-\frac{x}{t2}} + A_3 e^{-\frac{x}{t3}} \qquad \text{eq. 7.10.}$$
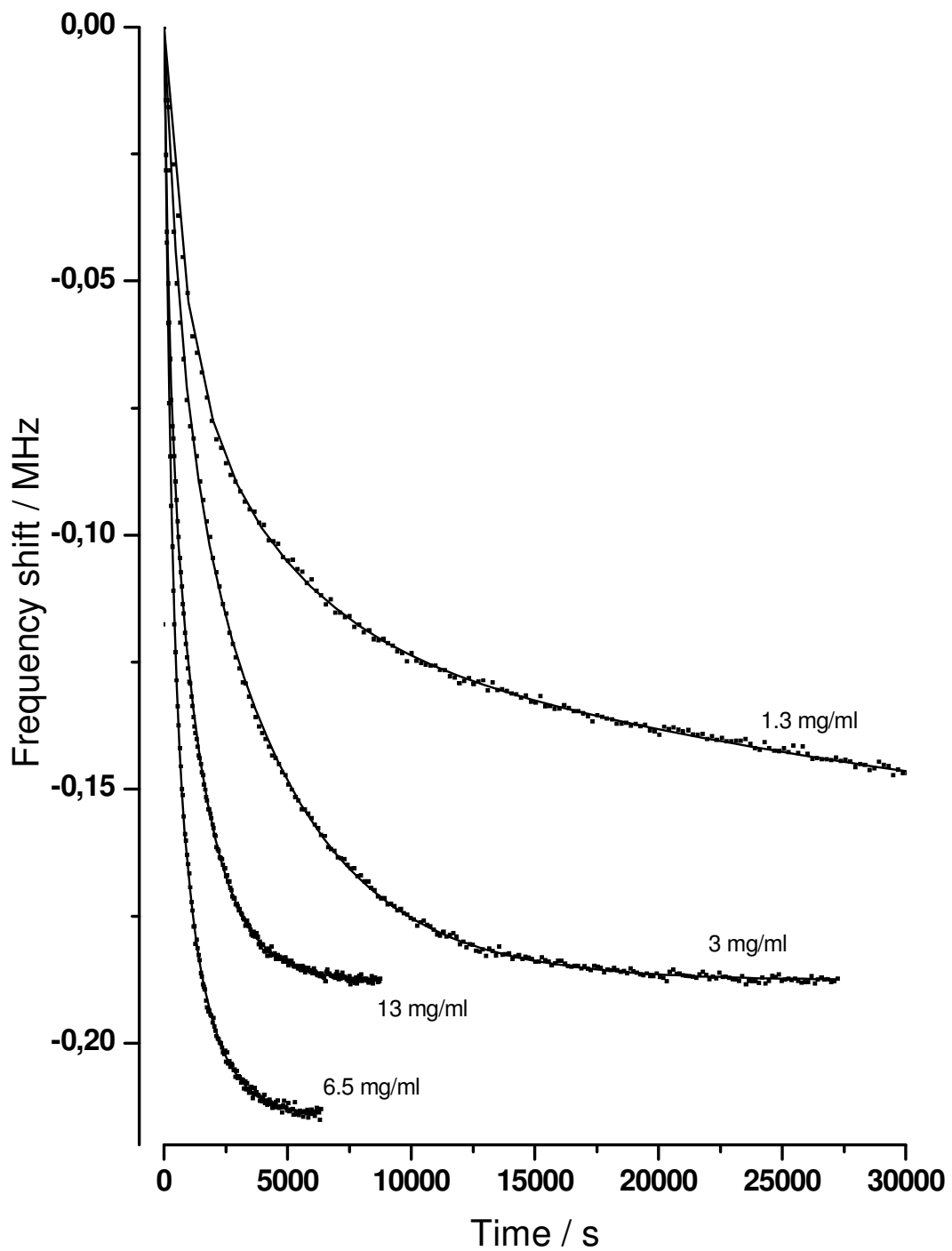
Figure 7.14: Dynamic measurements (dots) and fit (line) for the formation of an S-layer at the sensor surface with different concentrations of the monomer in solution. For c=1.3 mg/ml a third order exponential function was required to fit the measurements properly, whereas for the higher concentrations second order was sufficient. Fit parameters are shown in table 7.3.

It was found that a first order exponential fit does not match the measurements. A second order fit on the other hand matches three of four measurements very well, as shown in figure 7.14. This stands in contrast to the measurements discussed in section 7.4, where neither a first order, nor a higher order fit matched the measurement. Taking up the argument there, it can be said, that in this case two independent reactions are running in parallel. Both reactions may use the same pool of reagents, but when it comes to the formation of the layer on the sensor surface, both reactions take place simultaneously. The reaction with the shortest reaction time t_1 roughly shows a reciprocal proportionality of the reaction time versus concentration of analyte. The time constants and saturation values for the different reactions are summarized in table 7.3.
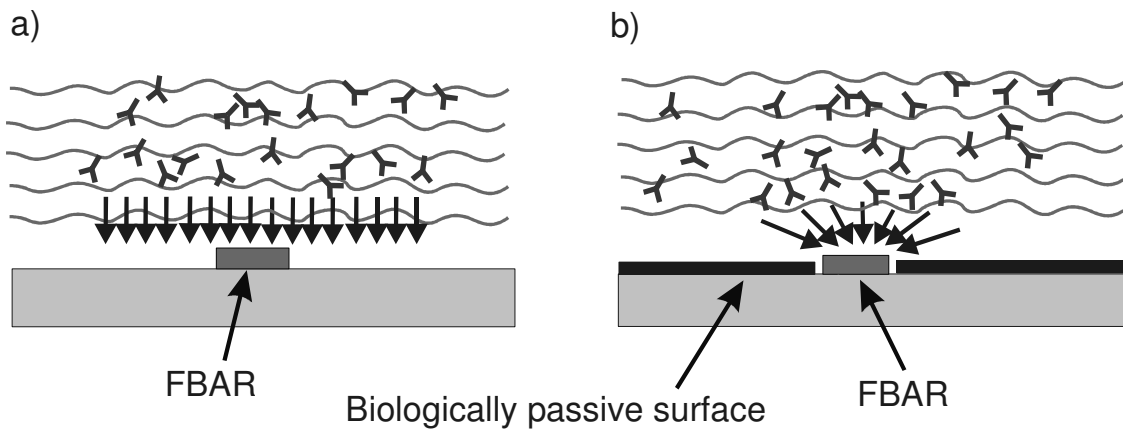
Figure 7.15: Optimization of the measurement setup regarding the diffusion profile: a) when the whole surface is biologically active, diffusion will be one-dimensional. b) When the surface surrounding the sensor is biologically passivated, diffusion will be two-dimensionally and diffusion-limitation will be reduced.

With $k_{AB} = \dfrac{1}{t_1 \cdot C[B]}$, the reaction constant can be calculated and is shown in the last column of table 7.3. According to the derivation in section 7.2, k_{AB} is expected to be a constant. Hence, the values shown in table 7.2 indicate, that the reaction for greater concentrations is slower than would be expected. Here, the influence of particle diffusion begins to play a role: the measurement system used here was an open flow cell and the solution stands still in the chamber. So the process is diffu-

sion limited. The reaction produces a depletion region in the vicinity of the surface and the mono-mers are accordingly diffusing towards the surface. With the overall concentration being smaller, the impact of diffusion limitation is relatively smaller. Three solutions exist to overcome the prob-lem of diffusion limitation: The first is to apply a flow of the particles thereby always offering the same concentration of analyte. The second is the application of an agitation mechanism to mix the fluid. A possible solution employing FBAR-technology was presented in chapter 6.8.

If neither of these solutions can be applied, a third possibility of optimization lies in the diffusion profile. This is illustrated in figure 7.15. When all of the surface is biologically active, particle dif-fusion will be in one direction only, from top towards the depletion region at the surface. The diffu-sion is one dimensional (see 7.15.a). When the surface surrounding the FBAR-sensor is biologically passivated, so that no particles react with the surface there, the diffusion profile will be two dimen-sional with particles diffusing towards the sensor also from the sides.

7.6 Carbon Nanotubes

Carbon nanotubes (CNTs) are a material drawing increasing attention in nanoscience. This is not only because of their exceptional electric properties, but increasingly because of some interesting biochemical features. With the application of carbon nanotubes as intermediate layers in biosensors, the selectivity in certain sensing applications can be significantly enhanced [SHI02]. The applica-tion of CNT on FBAR was therefore investigated.

A thin layer of CNT was deposited onto the wafer surface and the sensors were characterized before and after deposition. A technique developed by Wu et al. [WU04], using mixed cellulose ester (MCE) filter membranes, was employed[9]. With the help of a surfactant suspension, a thin film of CNTs was applied onto these membranes by vacuum filtration. They were then attached to the wa-fer with some water in between, allowing for an efficient adhesion of the nanotube film to the sub-strate. After that, the wafer was placed into the oven and was dried for 60 minutes at 115 °C. The MCE was then removed, placing the wafer into a bath of acetone for 15 minutes. The films were found to be highly homogenous as determined by SEM and AFM measurements, and the measured thickness was about d = 20 nm.

---

[9] Processing was carried out by Daniel Sickert

Interestingly, the measurements of the resonance frequency yielded a positive frequency shift, which amounted to an average of Δf = 5 MHz. Such a positive frequency shift can not be explained with a pure mass attachment according to the Sauerbrey model. To analyze these measurments, a two layer model was therefore applied. This model was derived by Lu-Lewis and was introduced in chapter 2.5 (equation 2.37). Replacing $f = \frac{v}{2t}$ on both sides of that equation and omitting the frequency shift Δf, which is still small compared to the unloaded resonance frequency, the resonance condition can be written as:

$$\rho_R v_R \tan\left(\frac{2\pi f_0 t_R}{v_R}\right) = -\rho_f v_f \tan\left(\frac{2\pi f_0 t_f}{v_f}\right) \qquad \text{eq. 7.11.}$$

Because of the small frequency shift the tangent can be approximated by $\tan\left(\frac{2\pi f_0 t_f}{v_f}\right) = \frac{2\pi f_0 t_f}{v_f} - \pi$ and equation 7.11 becomes:

$$\rho_R v_R \tan\left(\frac{2\pi f_0 t_R}{v_R}\right) = -\rho_f v_f \left(\frac{2\pi f_0 t_f}{v_f} - \pi\right) \qquad \text{eq. 7.12,}$$

The acoustic velocity v_f of the layer can then be determined:

$$v_f = \frac{\rho_R v_R}{\rho_f \pi} \tan\left(\frac{2\pi f_0 t_R}{v_R}\right) + 2 f_0 t_f \qquad \text{eq. 7.13.}$$

Assuming a mass density for the CNT's of 1.4 g/cm^3, an acoustic velocity of 80 m/s is obtained. This is much smaller than the acoustic velocity of the resonator itself (about 5600 m/s) and also

considerably smaller than the velocity of air (343 m/s). It is however comparable to the acoustic velocity of soft PVC (also 80 m/s).

Why does such a positive frequency shift occur at all, when mass is added? Figure 7.16 shows a schematic representation of the wave form of the resonance. In figure 7.16 a, a single layer resonator is shown, containing a simple sinusoidal half wave. In figure 7.16 b, the same resonator is shown with a thin overlayer. The free end of the resonator is at the overlayer surface, so the phase point with maximum amplitude (marked with an open dot) is moving outwards, leading to an increase of the wavelength. When the overlayer becomes thicker than that, a considerable part of the wave will be in the overlayer. The overlayer surface is free, so there will be an antinode. This in turn leads to a reduction of the wavelength (the phase points marked with an open dot is moving into the resonator layer). So in effect the frequency increase is only possible because of an increase in wave number (which is 1 in 7.16.c compared to ½ in a).

When an application of carbon nanotubes is desired, the extremely low acoustic velocity of such films has to be considered and the sensor has to be designed very carefully. In particular, the non linear frequency response has to be analyzed in advance, as it can seriously affect the sensivity. Non linearity of the frequency response in multilayer structures has been analyzed in chapter 3.1. With their low acoustic velocity, CNT-layers are a candidate, that could be used in a configuration for sensitivity enhancement discussed in chapter 3.1. With the quality factor reducing by about half in the experiment, the sensitivity enhancement may outmatch this reduction and lead to an improved overall performance according to equation 4.3.
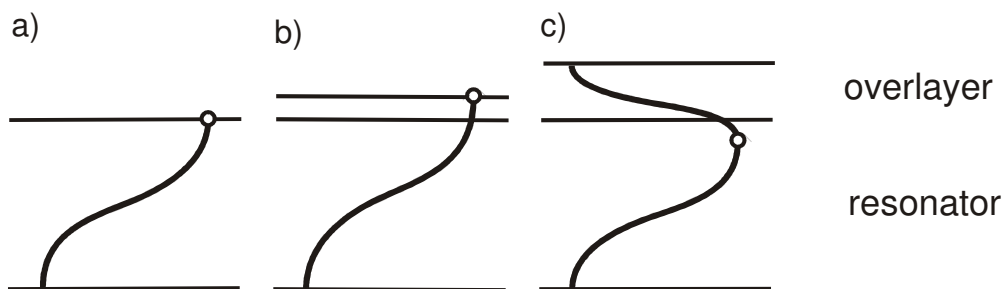

Figure 7.16: Explanation of the frequency increase due to a mass attachment. It is possible only because of an increase in wave number.

8.   Conclusions and Outlook

It could be shown in this work, that the FBAR is a highly suitable device for different applications. Given the fact, that it is in the early stages of development and already shows a similar performance as the lower frequency QCM device in practical biosensing applications (see chapter 7.3), it promises to have great prospects in future applications. Ways towards an improvement of the sensor performance were highlighted in this work, most notably the method for sensitivity enhancement presented in chapter 3.1. The FBAR will especially benefit from the manifold experience made during more than 30 years of application of the QCM sensor, which despite the lower frequency seems to behave in a quite similar way.

The adaptation of bulk acoustic wave sensor technology to CMOS compatible processes bears many advantages, which could pave the way of this technology towards a mass market device in at least some of the applications mentioned the introduction. Bulk acoustic wave sensors can now be manufactured on wafer level and with standard semiconductor technologies, thereby reducing the price of a single sensor dramatically. An integration of the sensing functions with the computing functions on a single chip is technologically possible and will make it a real MEMS device. Because the crucial dimension is the layer thicknesses (defining the resonance frequency) and the lateral dimension is secondary, the pitch size can be chosen almost freely. There is no principle limitation for the lateral size as it exists for instance for surface acoustic waves (determined by their delayline). The FBAR size can be customized to fit almost any requirement from the application.

In the analysis of the mode structure in chapter 3, some important sensor properties could be revealed. It was thereby distinguished between longitudinal and lateral modes. The longitudinal modes were analyzed employing the one dimensional Mason model. With this model it could be shown that with an appropriately dimensioned additional layer on top the sensor, the sensitivity can be enhanced above the value of a single layer device (the so-called Sauerbrey sensitivity). Depending on the impedance ratio, this increase can be of an order of magnitude and more. This may provide a powerful tool to enhance the sensor performance as it only implies the application of an additional layer with a low acoustic impedance. Futhermore, the influence of the acoustic mirror was examined. With an acoustic mirror being partially reflective, a simultaneous excitation of resonator modes (with the frequency determined by resonator thickness) and wafer modes (whose frequency is determined by the wafer thickness and overmode number) could be observed. This leads to an anticrossing like behaviour with the resonator mode evolving into a wafer mode and vice versa. Because of the different mass sensitivities of wafer and resonator modes this behaviour can be ex-

ploited in order to differentiate between a mass attachment and intrinsic changes of the resonator properties such as a temperature change.

The investigation of the lateral modes showed, that for longitudinal bulk modes the dominating lateral modes are of a thickness extensional type. Through application of a specifically patterned top layer these lateral modes can be manipulated and a mode selection seems possible. It was shown that such a mode selection can have a positive impact on the sensor performance as the energy is concentrated in a certain mode. In future laser probing techniques may be applied [TIK98] in order to determine the distribution of the lateral vibration amplitude in advance thus enabling a more precise application of the mode selecting structure. Furthermore, an improvement of the formation of lateral modes may be achieved by manufacturing resonators with steeper edges by applying a more anisotropic etching technique.

Through analysis with the BVD model it was shown that the lateral modes have quality factors above the quality factor of the pure longitudinal mode. This may be another reason for the increase of quality factor through mode selection. Another possibility to improve mode selection is to increase the mode separation by making the lateral dimensions smaller. It was shown that for a lateral extent of for instance 35 μm the spacing between the first two visible lateral modes was about 9 MHz which is a little above the frequency shifts expected for most bindings (for the antibody-antigen sequence in chapter 7 it was in the range of 1 to 2 MHz for instance). So making the device smaller seems to make sense. Not only the acoustic properties are improved but also electrically it is favourable. This was shown in chapter 4 where the best quality factors were obtained for small resonators at series resonance. For integration into a read out circuitry however the Ohmic matching must be kept in mind.

In chapter 4 the sensor performance was investigated. It is ruled by a very complicated set of influences, so it is neither possible nor desirable to make an exact theoretical description of the sensor performance. It was therefore focused on the parameters that were scalable or object to optimization during the fabrication process. In the investigation of the influence of electrical resistance it resulted that a proper scaling of the relation of the motional resistance R_m and series resistance R_s is important. Apart from the acoustic losses this relation is essentially determined by the resonator geometry, namely the signal line length and cross section and the active resonator area. Furthermore it could be shown that the complex impedance and the series resistance together can lead to a significant reduction of the series quality factor with resonator area.

The investigation of the frequency dependent performance did not reveal a clear trend. For high frequencies (8 GHz) the surface roughness becomes an important factor limiting the achievable Q-factor of the device due to thickness fluctuation. This cancels out at least partially the improvements achieved due to the higher sensitivity. Electrode thickness on the other hand sensibly influences the sensitivity and also has to be taken especially into account at higher frequencies. In order to make a complete assessment of the frequency dependent performance, the frequency dependence of noise will have to be determined in future work. This influence strongly depends on the respective application and on the read out circuit applied and noise can even be induced by the application itself by random mass attachments for example.

The investigation in chapter 5 revealed significant frequency shifts due to an externally applied stress. This behaviour was shown to be determined by three influences being a variation in thickness, density and change in the elastic constants. The latter influence proved to be the very similar as for bulk ZnO (the values were taken from literature). The measurement setup corresponded to two possible applications. In the first, the sensor would be applied on a substrate in the manner of a strain gauge measuring the bending of the substrate. The second would be a membrane configuration measuring the ambient pressure of a fluid or gas. In order to evaluate the performance of such an ambient pressure sensor, the sensor technology has to be applied in a membrane form and issues such as the long term stability, membrane roughness and optimum aspect ratios should be investigated.

The theoretical study of the FBAR performance in liquid (physical model in chapter 6.1) yielded lower losses for lower frequencies. Furthermore, a setup with a resonator material with high impedance is favoured, also reducing acoustic losses in the liquid. In future it should be tried to integrate this model into the multilayer structure of the device. In chapter 3, an improvement of the sensor sensitivity through application of a low impedance intermediate layer was shown. One of the tasks should be to bring these two conflicting influences in line and to find an optimum working point for the sensor in liquid.

The investigation of high viscosities brought some interesting physical properties and the liquid does not seem purely viscous any more for a certain viscosity-density product. It will be revealing to investigate this with resonators of different frequencies in order to see, whether this transition is scaling with the relaxation time, as supposed by the Mason model [MAS65]. When the sensor is further optimized and especially perturbations such as the wafer resonances are eliminated, more sophisticated methods of resonance analysis such as a direct impedance fitting known from QCM analysis may be adopted [FIL94]. In particular, the influence of surface roughness should be inves-

tigated to find out whether current models for the sensor response (such as [URB94]) apply at FBAR frequencies. Surface roughness may provide an interesting parameter in order to distinguish between different effects such as mass density and visocisity of a liquid.

Maybe one of the most important results of this work is, that the sensor is actually working as a biosensor. This was shown in chapter 7, carrying through an extensive study to evaluate the performance in measurements with an avidin-antiavidin system. These measurements were reproduced with a QCM system under the same conditions. They showed qualitatively the same results with the FBAR performance in terms of the minimum detectable mass being slightly better. So the FBAR is in the right condition to be tested with different biosensing applications.

Another issue, that will have to be addressed in future, is the temperature stability of the device. The temperature sensitivity of the shear mode FBAR used in this work is about -40 kHz / K, so temperature changes in the environment may falsify the measurement result. A temperature stabilization as in the setup used in this work may not (especially for a highly miniaturized device) always be applicable. Reading out the temperature seperately and correcting the frequency shift accordingly may be one solution. In chapter 3, it was demonstrated that longitudinal acoustic modes can have a strongly varying mass sensitivity depending on the specific mode form. This provides an elegant solution to differentiate between temperature change and mass attachment by interpreting the frequency shift for different modes. Such a readout can even be done with the same sensor having the advantage, that local temperature changes due to the reaction energy can be detected and utilized as a further information.

Another method for dealing with the influence of temperature consists in using materials with opposite temperature coefficient. This method is already used for temperature stabilization of filters [LAK00]. Nevertheless, if the temperature can be read out exactly and an accordant correction can be carried out (as it was done for instance in chapter 6.7) then such a temperature compensation may be needless. Furthermore, the requirement for temperature stabilization would strongly limit the developer of the device in the choice of the materials used for the sensor and the sensor layer structure.

Bibliography

ASH03 D. C. Ash, M. J. Joyce, C. Barnes, C. J. Booth, A. C. Jefferies, *Viscosity measurement of industrial oils using the droplet quartz crystal microbalance,* Meas. Sci. Technol., 2003, *14,* pp. 1955-1962

BEH98 C. Behling, R. Lucklum, P. Hauptmann, *Response of quartz-crystal resonators to gas and liquid analyte exposure,* Sensors and Actuators A, 1998, *68,* pp. 388-398

BEN97 E. Benes, M. Groschl, F. Seifert, A. Pohl, *Comparison between BAW and SAW Sensor Principles,* IEEE International Frequency Control Symposium, 1997, pp. 5-20

DEC01 F. Decremps, J. Zhang, B. Li, R. C. Liebermann, *Pressure-induced softening of shear modes in ZnO,* Physical Review B, 2001, *63,* 224105, pp. 1-5

DUN91 W. C. Duncan-Hewitt, M. Thompson, *Four-Layer Theory for the Acoustic Shear Wave Sensor in Liquids Incorporating Interfacial Slip and Liquid Structure,* Anal. Chem., 1992, pp. 94-105

FAW88 N. C. Fawcett, J. A. Evans, L. C. Chien, N. Flowers, *Nucleic acid hybridization detected by piezoelectric resonance,* Anal. Letters, 1988, *21,* pp. 1099

FIL94 C. Filiatre, G. Bardeche, M. Valentin, *Transmission-line model for immersed quartz-crystal sensors,* Sens. Actuators A, 1994, pp. 137-144

FRE99 J. Freudenberg, S. Schelle, K. Beck, M. v. Schickfus, S. Hunklinger, *A contactless surface acoustic wave biosensor,* Biosensors & Bioelectronics, 1999, *14 (4),* p. 423-425

GAB04 R. Gabl et al., *First results on label-free detection of DNA and protein molecules using novel integrated sensor technology based on gravimetric sensor principles,* Biosensors and Bioelectronics, 2004, *18,* pp. 615-620

GUH05 G. Guhr, R. Kunze, G. Martin, H. Schmidt, M. Weihnacht, *Monitoring blood coagulation with QCM and SH-SAW sensors,* IEEE Ultrasonics Symposium, 2005, pp. 58-61

HAM97 J.M. Hammond, R.M. Lec, X.J. Zhang, D.G. Libby, L.A. Prager, *An acoustic automotive engine oil quality sensor,* Proceedings of the IEEE International Frequency Control Symposium, 1997, pp. 72-80

HOU91 M. Hoummady, F. Bastien, *Acoustic wave viscometer,* Rev. Sci. Instrum.1998, *62 / 8,* pp. 1999-2003

JAK02 B. Jakoby, H. Eisenschmid, F. Herrmann, *The Potential of Microacoustic SAW- and BAW-Based Sensors for Automotive Applications - A Review,* IEEE Sensors Journal, 2002, *vol. 2, no. 5,* pp. 443-452

JAK98 B. Jakoby, M. J. Vellekoop, *Viscosity sensing using a Love-wave device,* Sensors and Actuators A, 1998, pp. 275-281

JAN00 A. Janshoff, H. J. Galla, C. Steinem, *Mikrogravimetrische Sensoren in der Bioanalytik - eine Alternative zu optischen Biosensoren?,* Angew. Chem. 2000, *112,* pp. 4165-4195

KAI03 J. E. J. Kaitila, M. Ylilammi, R. Aigner, *Spurious Resonance Free Bulk Acoustic Wave Resonators,* Proceedings IEEE Ultrasonics Symposium, 2003

KAN85 K. K. Kanazawa, J. G. Gordon, *The Oscillation Frequency of a Quartz Resonator in Contact with a Liquid,* Analytica Chimica Acta, 1985, *175,* pp. 99-105

KNI98 J. B. Knight, A. Vishwanath, J. P. Brody, and R. H. Austin, *Hydrodynamic Focusing on a Silicon Chip: Mixing Nanoliters in Microseconds,* Phys. Rev. Letters 1998, *80, no.17,* pp. 3863-3866

KUN03 J. Kuntner, G. Stangl, B. Jacoby, *Analyzing the Non-Newtonian Behavior of Oil-Based Liquids Using Microacoustic Sensors,* Proceedings of IEEE International Conference on Sensors, 2003, pp. 956-960

LAK00 K. M. Lakin, K. C. McCarron, J. F. McDonald, *Temperature Compensated Bulk Acoustic Thin Film Resonators*, IEEE Ultrasonics Symposuim, 2000

LAK03 K. M. Lakin, K. G. Lakin, *Numerical Analysis of Thin Film BAW Resonators*, Proceedings IEEE Ultrasonics Symposium, 2003, pp. 74-79

LAK92 K. M. Lakin, G. R. Kline, *Thin Film Bulk Acoustic Wave Filters for GPS*, IEEE Ultrasonics Symposium, 1992, pp. 471-476

LAK93 K. M. Lakin, G. R. Kline, *High-Q Microwave Acoustic Resonators and Filters*, IEEE Transactions on Microwave Theory and Techniques, 1993, *41/12,* pp. 2139-2145

LAK95 K. M. Lakin, G. R. Kline, K. T. McCarron, *Development of Miniature Filters for Wireless Applications*, IEEE Transactions on Microwave Theory and Techniques, 1995, *vol. 43, no. 12*, pp. 2933-2939

LAN03 R. Lanz, P. Muralt, *Solidly Mounted BAW Filters for 8 GHz based on AlN Thin Films*, IEEE Ultrasonics Symposium, 2003, pp. 178-181

LAR00 J. Larson, P. Bradley, S. Wartenberg, R. Ruby, *Modified Butterworth-Van Dyke Circuit for FBAR Resonators and Automated Measurement System*, IEEE Ultrasonics Symposium, 2000, pp. 863-868

LAR02 J. D. Larson, Y. Oshmyansky, *Measurement of Effective kt²,Q,Rp,Rs vs. Temperature for Mo/AlN FBAR Resonators*, Proceedings IEEE Ultrasonics Symposium, 2002, *1*, pp. 939-943

LEC01 R. M. Lec, *Piezoelectric Biosensors: Recent Advances and Applications*, IEEE International Frequency Control Symposium and PDA Exhibition, 2001, pp. 419-429

LEE04 J.-H. Lee, C.-M. Yao, K.-Y. Tzeng, C.-W. Cheng, Y.-C. Shih, *Optimization of Frame-like Film Bulk Acoustic Resonators for Suppression of Spurious Lateral Modes Using Finite Element Method*, Proceedings IEEE Ultrasonics Symposium, 2004, pp. 278-281

LID95 D.R. Lide, Handbook of Chemistry and Physics, 76th Edition, CRC Press, 1995 ISBN 0-8493-0597-7

LIN05 A. Link, E. Schmidhammer, *Suppression of Spurious Modes in Mirror-Type FBARs Using an Appropriate Shape of the Active Area*, Proceedings IEEE Ultrasonics Symposium, 2005

LINK1 M. Link, M. Schreiter, J. Weber, R. Gabl, D. Pitzer, R. Primig, W. Wersing, *c-axis inclined ZnO films for shear-wave transducers deposited by reactive sputtering using an additional blind*, J. Vac. Sci. Technol. A, 2006, *24 (2)*, pp. 218-222

LINK2 M. Link, *Study and realization of shear wave mode solidly mounted film bulk acoustic resonators (FBAR) made of c-axis inclined zinc oxide (ZnO) thin films: application as gravimetric sensors in liquid environments*, PhD Thesis, Université Henri Poincaré Nancy I, 2006

LOH05 R. Lohr, *Wireless Sensors*, McGraw-Hill Yearbook of Science and Technology, McGraw-Hill, 2005 pp. 389-391

LU72   C.-S. Lu, O. Lewis, *Investigation of film-thickness determination by oscillating quartz resonators with large mass load*, Journal of Applied Physics, 1972, *vol. 43, no. 11*, pp. 4385-4390

LUC00   R. Lucklum, P. Hauptmann, *The quartz crystal microbalance: mass sensitivity, viscoelasticity and acoustic amplification*, Sensors and Actuators B, 2000, *70*, pp. 30-36

LUC97   R. Lucklum, C. Behling, R. W. Cernosek, S. J. Martin, *Determination of complex shear modulus with thickness shear mode resonators*, Journal of Physics D: Applied Physics, 1997, *30*, pp. 346-356

LUT97   J. J. Lutsky, Massachusetts Institute of Technology, *A Sealed Cavity Thin-Film Acoustic Resonator Process for RF Bandpass Filters*, 1997

MAK01   T. Makkonen, A. Holappa, J. Ellä, M. M. Salomaa, *Finite Element Simulations of Thin-Film Composite BAW Resonators*, IEEE Transactions on Ultrasonics, Ferroelectrics and Frequency Control, 2001, *vol. 48, no. 5*, pp. 1241-1258

MAK04   T. Makkonen, T. Pensala, J. Vartiainen, J. V. Knuuttila, J. Kaitila, M. M. Salomaa, *Estimating Materials Parameters in Thin-Film BAW Resonators Using Measured Dispersion Curves*, IEEE Transaction on Ultrasonics, Ferroelectrics and Freuqency Control, 2004, *vol. 51, no. 1*, pp. 42-51

MAN89   E. H. Mansfield, *The bending and stretching of plates*, 1989, Cambridge university press

MAS65   W.P. Mason (Editor), *Physical acoustics*, Academic Press, New York, vol. II A, 1965

MIL83   R. F. Milsom, J. E. Curran, S. L. Murray, *Effect of Mesa-Shaping on Spurious Modes in ZnO/Si Bulk-Wave Composite Resonators*, Proceedings IEEE Ultrasonics Symposium, 1983, pp. 498-503

MIN01   Reports on Micro and Nano Technologies, MINATECH Information Day / Conference on Micro and Nano Technologies, 12 December 2001 in Teltow

POH97   A. Pohl, G. Ostermayer, L. Reindl, F. Seifert, *Monitoring of the tire pressure at cars using passive SAW sensors*, IEEE Ultrasonics Symposium, 1997, pp. 471-474

RAT05   A. Rathgeber, M. Wassermeier, A. Wixforth, *Acoustic 'Distributed Source' Mixing of Smallest Fluid Volumes*, Journal of ASTM International, 2005, *vol. 2, no. 6*

REE76   T. M. Reeder, D. E. Cullen, O. A. J. Saunder, *Frequency output pressure sensor based on an application of surface acoustic wave technology*, Proc. Automotive Engineering Congress and Expositions, Detroit, 1976, Paper No. 760093

ROS88   J. Rosenbaum, *Bulk Acoustic Theory and Devices*, Artech House, Inc., 1988 0-89006-265-X

RUB05   R. Ruby, J. Larson, C. Feng and S. Fazzio, *The Effect of the Perimeter Geometry on FBAR Resonator Electrical Performance*, Proceedings IEEE International Microwave Symposium, 2005

SAL02   S. Salgar, G. Kim, D.-H. Han, B. Kim, *Modeling and Simulation of the Thin Film Bulk Acoustic Resonator*, IEEE International Frequency Control Symposium and PDA Exhibition, 2002, pp. 40-44

SAU59   G. Sauerbrey, *Verwendung von Schwingquarzen zur Wägung dünner Schichten und zur Mikrowägung*, Zeitschrift f. Physik, 1959, *155*, pp. 206-222

SHI01   M. Shim, N. Wong Shi Kam, R. J. Chen, Y. Li, H. Dai, *Functionalization of Carbon Nanotubes for Biocompatibility and Biomolecular Recognition*, Nano Letters, 2002, *vol. 2, no. 4*, 285-288

SHO72   A. Shons, F. Dorman, J. Najarian, *An Immunospecific Microbalance*, J. Biomed. Mater. Res., 1972, *vol. 6*, pp. 565-570

STE05   D. Steppich, *Kopplung von mechanischen und thermodynamischen Eigenschaften von Phospholipidmembranen in der Nähe von Phasenumwandlungen - Bedeutung für Anwendungen und Biologie*, Diplomarbeit am Lehrstuhl Experimentalphysik I, Universität Augsburg, 2005

TIE77   H. F. Tiersten, *Perturbation theory for linear electroelastic equations for small fields superposed on a bias*, J. Acoust. Soc. Am., 1978, *64 (3)*, pp. 832-837

TIK98   P. T. Tikka, J. Kaitila, *Laser Probing and FEM Modeling of Ultrasonically Vibrating Surfaces*, Proceedings IEEE Ultrasonics Symposium, 1998, pp. 1143-1146

TOE03   A. Toegl, R. Kirchner, C. Gauer, A. Wixforth, *Enhancing Results of Microarray Hybridizations Through Microagitation*, Journal of Biomolecular Techniques, 2003, *vol. 14, no. 3*, pp. 197-204

UCH01 K. Uchino, S. Hirose, *Loss Mechanisms in Piezoelectrics: How to Measure Different Losses Separately*, IEEE Transaction on Ultrasonics, Ferroelectrics and Frequency Control, 2001, *vol. 48, no. 1*, pp. 307-321

URB94 M. Urbakh, L. Daikhin, *Roughness effect on the frequency of a quartz-crystal resonator in contact with a liquid*, Physical Review B, 1994, *vol. 49, no. 7*, pp. 4866-4870

VAL90 C. Vale, J. Rosenbaum et al., *FBAR Fiters at GHz Frequencies*, Proceedings of the 44th Annual Symposium on Frequency Control, 1990, pp. 332-336

VIG00 J. R. Vig, F. L. Walls, *A review of sensor sensitivity and stability*, Frequency Control Symposium and Exhibition, 2000, pp. 30-33

VIV00 V. Vivek, Y. Zeng, E. S. Kim, *Novel acoustic-wavemicromixer*, Proc. IEEE MEMS, 2000, pp. 668-673

WU04 Z. Wu, Z. Chen, X. Du, J. M. Logan, J. Sippel, M. Nikolu, *Transparent, Conductive Carbon Nanotube Filmes*, Science, 2004, *vol. 305, no. 5688*, pp. 1273-1276

ZHU98 X. Zhu and E.S. Kim, *Microfluidic Motion Generation with Acoustic Waves*, Sensors and Actuators: A. Physical, 1998, *66/1-3*, pp. 355-360

Veröffentlichungen

J. Weber, W. M. Albers, J. Tuppurainen, M. Link, R. Gabl, W. Wersing, M. Schreiter, *Shear mode FBARs as highly sensitive liquid biosensors*, Sensors and Actuators A 128, 2006, pp. 84-88

J. Weber, M. Link, R. Primig, D. Pitzer, M. Schreiter, *Sensor for ambient pressure and material strains using a thin film bulk acoustic resonator,* Proceedings of the IEEE International Ultrasonics Symposium, 2005, vol. 2, pp. 1258-1261

J. Weber, M. Link, R. Primig, D. Pitzer, M. Schreiter, *High frequency viscosity sensing with FBARs,* Proceedings of the IEEE International Frequency Control Symposium, 2006, pp. 117-121

J. Weber, M. Link, R. Primig, D. Pitzer, W. Wersing, M. Schreiter, *Investigation of the Scaling Rules determining the Performance of Film Bulk Acoustic Resonators operating as Mass-Sensors,* IEEE Transactions on Ultrasonics, Ferroelectrics and Frequency Control, 2007, (in press)

J. Weber, M. Schneider, A. Wixforth, work in progress

Appendix

Modelling parameters vertical acoustic modes (chapter 3.1)

A matlab program implementing the one dimensional Mason model was applied to analyze the structure of the vertical acoustic modes. The modelling parameters used to obtain the results in chapter 3 were the following:

Figure 3.1:

Layer thicknesses (/ μm):

    0 – 0.5 variable layer, 0.05 top electrode, 0.4 piezolayer, 0.05 bottom electrode

Mass density:

5606 kg/m^3 for all layers (mass density of ZnO)

Acoustic velocity:

Variable layer: factor in figure · 6370 m/s

Other layers: 6370 m/s

Figure 3.2:

Layer thicknesses (/ μm):

Without: 0 – 0.05 Mass attachment, 0.05 top electrode, 0.4 piezolayer, 0.05 bottom electrode

With, 1, with, 0.1: 0 – 0.05 Mass attachment, 0.0296 Intermediate layer, 0.05 top electrode, 0.4 piezolayer, 0.05 bottom electrode

Mass density:

5606 kg/m^3 for all layers (mass density of ZnO)

Acoustic Velocity:

Without: 6370 m/s for all layers

With, 1: Intermediate layer 637 m/s, 6370 m/s for all other layers

With, 0.1: Intermediate layer and mass attachment 637 m/s, 6370 m/s for all other layers

Figure 3.3:

Membrane:

Layer thicknesses (/ μm)

   0.01 top electrode, 0.43 piezolayer, 0.01 bottom electrode

Mass density:

   5606 kg/m^3 for all layers (mass density of ZnO)

Acoustic Velocity:

   6370 m/s for all layers

Mirror:

Layer thicknesses (/μm):

   0.01 top electrode, 0.58 piezolayer, 0.01 bottom electrode, 0.6 mirror layer high velocity, 4

   × (0.15 mirror layer low velocity, 0.6 mirror layer high velocity), 20 substrate

Mass density:

   5606 kg/m^3 for all layers (mass density of ZnO)

Acoustic Velocity:

   6370 m/s top electrode, piezolayer, bottom electrode and substrate 12740 m/s mirror layer

   high velocity, 3185 m/s mirror layer low velocity

Figure 3.4:

Before mass attachment: Same as for figure 3.3

With material added (only the thickness of the top electrode changes)**:**

Membrane: Thickness top electrode 0.082

Mirror: Thickness top electrode 0.106

Figure 3.5:

Wafer modes (solid lines)**:**

Layer thicknesses (/μm):

   0.43 – 0.8 top electrode, 0.58 piezolayer, 0.01 bottom electrode, 0.6 mirror layer high veloc-

   ity, 4 × (0.15 mirror layer low velocity, 0.6 mirror layer high velocity), 20 substrate

Mass density:

5606 kg/m^3 for all layers (mass density of ZnO)

Acoustic Velocity:

6370 m/s top electrode, piezolayer and bottom electrode, 12740 m/s mirror layer high velocity, 3185 m/s mirror layer low velocity

Resonator mode (dashed line)**:**

Layer thicknesses (/μm):

0.02 top electrode, 0.43 – 0.8 piezolayer, 0.02 bottom electrode

Mass density:

5606 kg/m^3 for all layers (mass density of ZnO)

Acoustic velocity:

6370 m/s for all layers

Lebenslauf

*20.1.1974	Hannover
5/93	Gymnasium Mellendorf, Abitur
10/93-11/95	Universität Hannover, Grundstudium Mathematik-Informatik, Vordiplom
10/95-10/97	Universität Hannover, Grundstudium Physik, Vordiplom
10/97-11/98	Zivildienst
11/98-6/02	Technische Universität München, Hauptstudium Physik, Diplom
	Spezialisierung Halbleiterphysik, Laserphysik
10/99-9/00	Universidad Complutense de Madrid
seit 11/03	Siemens Corporate Technology, München, Promotion